

ABSTRACT

Title of dissertation: DEMONSTRATION OF A QUANTUM GATE
WITH ULTRAFAST LASER PULSES

Jaime David Wong Campos
Doctor of Philosophy
2017

Dissertation directed by: Professor Christopher R. Monroe
Joint Quantum Institute
University of Maryland Department of Physics
and
National Institute of Standards and Technology

One of the major problems in building a quantum computer is the development of scalable and robust methods to entangle many qubits. Quantum computers based on trapped atomic ions are one of the most mature and promising platforms for quantum information processing [1, 2], exhibiting excellent coherence properties [3], near-perfect qubit detection efficiency [4], and high-fidelity entangling gates [5, 6]. Entangling operations between multiple ions in a chain typically rely on qubit state-dependent forces that modulate their Coulomb-coupled normal modes of motion [1, 7, 8]. However, scaling these operations to large qubit numbers in a single chain must account for the increasing complexity of the normal mode spectrum, and can result in a gate time slowdown [9] or added complexity of the control forces [10]. In this thesis, I present an alternative route to the scalability problem using optical interactions faster than any state evolution. The experiments shown here represent a

proof of principle for quantum manipulation of atoms in the strong coupling regime. This work relies on spin dependent forces (SDK) with short laser pulses and use it as our fundamental building block for thermometry and non-trivial motional state preparation. Together with a robust stabilization of the ion trap and high light collection efficiency, we demonstrate two-ion entanglement with ten ultrafast pulses. Due to the nature of the interaction, the demonstrated entangling operation can be made arbitrarily fast only limited by laser engineering.

DEMONSTRATION OF A QUANTUM GATE WITH
ULTRAFAST LASER PULSES

by

Jaime David Wong Campos

Dissertation submitted to the Faculty of the Graduate School of the
University of Maryland, College Park in partial fulfillment
of the requirements for the degree of
Doctor of Philosophy
2016

Advisory Committee:

Professor Christopher R. Monroe, Chair/Advisor
Professor Alexey V. Gorshkov
Professor Mohammad Hafezi
Professor Howard Milchberg
Professor Luis A. Orozco

© Copyright by
Jaime David Wong Campos
2017

Dedication

This thesis is dedicated to my family and the people that have constantly supported me throughout the ten years after I left my country.

Acknowledgments

I believe that a good reason of why I am where I am is because of Luis Orozco. Before starting grad school at University of Maryland, he took the high risk of giving a four-month job to someone as crazy as me with a failed english exam and a not so incredible curriculum. After that period, Luis kindly guided me through the process of finding a research group so I could start my graduate studies. Words are not enough to demonstrate my gratitude to you, so I hope my future actions show how much I thank you.

The summer before starting grad school, I had the good fortune of landing a research assistanship in a group full of extremelly smart and capable people. I thank Chris Monroe for letting that happen and pick someone who did not really know what was going on. Chris has a good blend between being a hands-off advisor and being there for proper advise. I really cherish those paper torture sessions where we grinded all the nonsense Kale, Steve and I put on the manuscript in question, always keeping a good vibe and learning a ton from each other. I think I am more sad of not having that experience again in the foreseeable future than I am from leaving the Ultrafast lab.

During my first three years of grad school, I worked directly with Kale Johnson who became one of my closest friends. After you left, I certainly missed fooling around with the *trident of destiny* (a roach killer). I thank you for your patience and friendship. It was awesome teaming up with you and understanding what was important and taking pride on our job, the works we published is a true testimony

of our productivity as a team. I look forward to continuing the work we started together, to new heights!

In my last year of grad school after Kale left, Steven Moses became my new labmate. Your intelligence is only rivaled by the kind of awesome human being you are. Thank you for training me and sharing your views about how science must be done and your perspicacity regarding lab techniques. I really hope to see you in the future, maybe hiking in the mountains of Colorado while you help us carry the jugs of water!

Although I feel lucky that the two people I spent most time became close friends, I thank to the other members of the Monroe group (in no special order), Jonathan Mizrahi, Brian Neyenhuis, Kai Hudek, Paul Hess, Ken Wright, Jason Amini, Jonathan Mizrahi, Volkan Inlek, Shantanu Debnath, Jake Smith, Aaron Lee, Geoffrey Ji, David Hucul, Phil Richerme, Grahame Vittorini, Crystal Senko, Taeyoung Choi, Daniel Brennan, Andrew Manning, Chenglin Cao, Marko Cetina, Norbert Linke, Jiehang Zhang, Martin Lichtman, Guido Pagano, Kristin Beck, Michael Goldman, Samantha Suplee, Caroline Figgatt, Clay Crocker, Harvey Kaplan, Ksenia Sosnova, Kevin Landsman, Antonis Kyprianidis, Daiwei Zhu, Allison Carter, Patrick Becker, Wen Lin Tan, Kate Collins, Laird Egan, Micah Hernandez, Eric Birckelbaw, Hanna Ruth, Sophia Scarano.

Because “life outside the lab” is also important, I thank the latin american gang Pablo Solano, Alejandra Maldonado, Ana Valdes, Francisco Salces, Israel Martinez, Kristel Izquierdo, Daniel Chang, Andres Yi, the team SSTT and Mossa Barandao. I also thank the good friends I left in Mexico such as Alejandro Abarca, Liza

Velarde, Felipe Yee, Pipen, Poke, Uni, Nacho, Gaby, Oliver, Chago, Llaguno and Guti. I thank you all for understanding that I was always busy with A or B project and that I am like a runaway horse by nature, always looking what to do next.

My parents Augusto and Virginia, and my siblings Sara and Augusto E. who helped me in making the decision of going to Mexico for my undergrand and be away from home. The whole Loo, Pacheco and Robles family in Mexico who took so much care of me and made my Decembers an amazing experience while being away from home. I hope the work written in this thesis will make you proud of what I have done with my time.

Finally, I thank Dalia Ornelas whose love and support in the past three years brightened even the darkest days. I thank you for helping me go through the hard days of grad school, which implied long work nights, weekend excursions to the lab and very frequent absences from social gatherings. Thanks for accepting me as I am, my weird humor and workaholic tendencies, I would be half a man without you. I am looking forward for the years to come, to see what adventures life is preparing and where we will go together.

I shall also thank the National Science Foundation for its support through the Physics Frontier Center at the Joint Quantum Institute since they supported my assistanship at the beginning of my graduate studies.

To all of you, and as Gustavo Cerati said: “*No solo no hubiera sido nada sin ustedes, sino con toda la gente que estuvo a mi alrededor desde el comienzo; algunos siguen hasta hoy. Gracias... totales!*”

Table of Contents

Dedication	iii
Acknowledgements	vi
List of Tables	ix
List of Figures	x
List of Abbreviations	xii
1 Introduction	1
1.1 Ion trap based quantum computing	4
1.1.1 Computation with phonons and qubits	5
1.1.2 The $^{171}\text{Yb}^+$ qubit	7
1.1.3 Spectral crowding and approaches to scalability	9
1.1.4 Thesis outline	12
2 The Apparatus	15
2.1 Linear Rf Traps	15
2.2 Trap frequency stabilization	19
2.2.1 Rectifier circuit	20
2.2.2 Rf amplitude locking results	22
2.3 Ion loading	25
2.3.1 Photoionization	25
2.3.1.1 Ion autoloader	26
2.4 Qubit state preparation	29
2.4.1 Doppler Cooling	29
2.4.2 Optical pumping	30
2.4.3 Detection	31
2.4.4 Qubit control with microwaves	33
2.5 Imaging system	34
2.5.1 Aberration retrieval	35
2.5.2 Fitting algorithm	36

2.5.3	Position sensing	37
2.5.4	Imaging system for two ions	40
3	Ultrafast spin control	43
3.1	Raman spin interactions	44
3.2	Single pulse rotation	47
3.3	Multiple pulses and weak regime	49
3.3.1	Beatnote lock	50
4	Ultrafast spin-motional control	52
4.1	Coherent state displacements and properties	52
4.2	Spin and motion coupling	54
4.3	Evolution operator for a single ultrafast pulse	56
4.3.1	Spin dependent kick	58
4.3.2	From weak to strong coupling	60
5	SDK characterization, and validation.	62
5.1	Experimental considerations	63
5.1.1	Drive to the Zeeman levels	63
5.1.2	Model	65
5.1.3	Polarization imperfection	66
5.1.4	Axial mode coupling	67
5.1.5	Leakthrough light	68
5.2	Experiments with SDKs	68
5.2.1	Thermometry with ultrafast pulses	69
5.2.2	Sensing of a thermal state	71
5.2.3	Fock State Tomography	77
5.2.4	Limits of Measurement	78
5.3	Generation of quantum superpositions (“Cat states”)	80
5.3.1	Three and Four-Component Cat Contrast	91
5.3.2	Six and Eight-Component Cat Contrast	92
5.3.3	Sources of Error	93
6	Demonstration of a quantum gate with ultrafast pulses	94
7	Conclusions and outlook	105
A	Normal mode spectrum numerical calculation	107
B	Ion loading code (Python)	110
C	Doppler Cooling limit	111
D	Zernike Polynomials	114
E	Allan deviation dead time analysis	115

List of Tables

3.1 Lasers used	50
---------------------------	----

List of Figures

1.1	Classical, quantum and probabilistic bits	2
1.2	Shannon entropy of a quantum system of phonons and qubits	6
1.3	$^{171}\text{Yb}^+$ atomic energy level diagram	8
1.4	Spectral crowding in a chain of 55 ion	10
1.5	Alternatives for scaling up an ion-based quantum processor	11
2.1	Blade trap	16
2.2	Helical resonator with a capacitive divider pickoff	20
2.3	Rectifier circuit	21
2.4	Can lock performance	23
2.5	Two photon ionization	26
2.6	Adaptive ion number recognition	27
2.7	Qubit state preparation	29
2.8	Optical pumping	31
2.9	Detection	32
2.10	Microwave time scan	33
2.11	Imaging system	35
2.12	Aberration retrieval	38
2.13	Ion position Allan variance	40
2.14	Two PMT detection	41
3.1	Single pulse power scan	48
3.2	Two pulse spin flip	49
4.1	Clebsch-Gordan coefficients and relevant energy levels	55
4.2	Single pulse motional wavepacket diffraction	58
4.3	Ultrafast experimental schematic	59
4.4	Weak to Strong	61
5.1	Component of electric field along the axial direction vs. distance from the center of the beam for a 2 (blue) and 5 (red) μm waist.	64
5.2	Infidelity vs. the ratio of the Rabi frequencies of the qubit and Zeeman transitions.	66

5.3	Ultrafast atom interferometry	70
5.4	Ultrafast sensing measurements of \bar{n}	72
5.5	Ultrafast thermometry in the sideband cooling regime	74
5.6	Ultrafast thermometry in the Doppler cooling regime	75
5.7	Ultrafast thermometry in the high \bar{n} regime	76
5.8	Ultrafast phase space tomography	79
5.9	Cat state creation	82
5.10	Fast Cat state creation and verification	84
5.11	Slow Cat state creation and verification	85
5.12	Three and four-component cat states	88
5.13	Six and eight-component cat states	89
6.1	Entangling gate experimental setup	95
6.2	Experimental setup for the quantum gate	96
6.3	Gate sequence and parity measurement theory	99
6.4	Gate sequence and parity measurement results	100
6.5	Parity vs. Gate phase	103

List of Abbreviations

AWG	Arbitrary Waveform Generator
BEC	Bose-Einstein Condensate
CCD	Charge-Coupled Device
CF	ConFlat
COM	Center of Mass
DC	Direct Current
EMCCD	Electron Multiplying Charge-Coupled Device
GVD	Group Velocity Dispersion
ICCD	Intensified Charge-Coupled Device
LO	Local Oscillator
MOT	Magneto-Optical Trap
NA	Numerical Aperture
PMT	Photomultiplier Tube
PSF	Point Spread Function
QIP	Quantum Information Processing
Rf	Radiofrequency
SDK	Spin-Dependent Kick
SQUID	Superconducting Quantum Interference Device
UHV	Ultra-High Vacuum
UV	Ultraviolet

Chapter 1: Introduction

Quantum mechanics is the theory of the microscopic realm and recent technical advances in the manipulation and control of basic quantum systems have triggered the use of some of its least intuitive properties, such as entanglement, for applications in practical devices. Quantum computation is one such applications with the capacity to revolutionize the world because of its potential to outperform conventional computers. It has been demonstrated that the memory capacity of such devices scale exponentially, compared to the linear scaling of current computers. Moreover, it is becoming apparent that classical computers are reaching a bottleneck in operation and manufacture since thermal runaway, quantum tunneling and variability in on-chip transistor electronic properties severely limits their scalability to faster devices.

One needs to first understand their building blocks of the two computing platforms to better comprehend their differences [11]. In a classical computer, the fundamental unit of information is the bit, which can represent either a 0 or 1 depending on its state i.e. a transistor is on and off but not both (figure 1.1a). Any string of information can be represented as a combination of several bits and we also notice that classical bits are *deterministic*, meaning that they can only

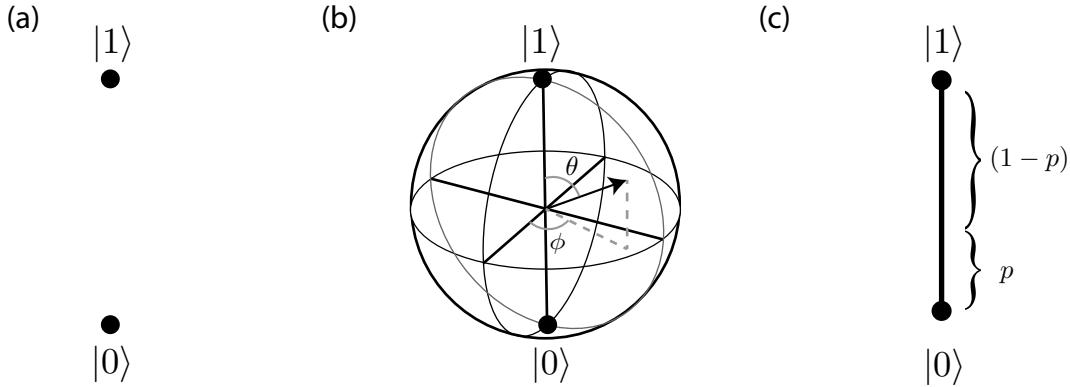


Figure 1.1: Classical, probabilistic and quantum bits. (a) Classical bits can only take two values in a deterministic way. (b) Quantum bits are represented by a point on a Bloch sphere and are better described by complex numbers. (c) A classical probabilistic bit could take either 0 or 1 with probabilities p and $(1-p)$ of obtaining either value. Bit values are represented as end points on a joining line.

change their state because of external perturbations. On the other hand, quantum computing makes use of the quantum bit or qubit as its fundamental information unit, which can also take binary values but possess different properties than its classical counterpart.

Qubits follow the rules of quantum mechanics and are intrinsically *probabilistic*. As a consequence, two pieces of independent information are needed to describe its behavior, making vectors in a Hilbert space an ideal way of representing them. Because of this inherent two dimensionality, qubits are usually represented as a point in the Bloch sphere (See figure 1.1b). Algebraically, the usual way of representing an arbitrary qubit is using the Dirac notation of bras ($|\psi\rangle$) and kets ($\langle\psi|$) for an arbitrary state ψ :

$$|\psi\rangle = \cos \theta |0\rangle + \exp(i\phi) \sin \theta |1\rangle, \quad (1.1)$$

where θ and ϕ are the two independent numbers describing the *probability amplitude*

and *phases* respectively. It is experimentally found that the act of measurement gives a value of 0 or 1 with a probability of $|\cos \theta|^2$ or $|\sin \theta|^2$ respectively, obtained by taking the absolute square of such amplitudes together with their phases. Such value remains true till the qubit is initialized again.

It is reasonable to ask ourselves if the behavior of a qubit can be mimicked by classical means, after all, we could create a probabilistic bit that can take either 0 or 1 value in a probabilistic manner (See figure 1.1c) with predefined weights p and $1 - p$. Although the answer is *yes* for a single unit, it is in general *no* when working with qubit ensembles. The reason is because qubits, as quantum mechanical objects, follow the superposition principle and can also be entangled. Qubit superpositions are a direct consequence of their quantum nature. The time evolution of a set of qubits and the interactions with each other follow the Schrödinger equation, which is a wave equation. Furthermore, entanglement is a unique quantum feature and is defined as the inability to independently describe the state of individual qubits in an ensemble from the rest in a nonlocal way [12]. One example of such a fully entangled two-qubit state is given by

$$|\psi\rangle = \frac{|0\rangle_1|1\rangle_2 - |1\rangle_1|0\rangle_2}{\sqrt{2}}, \quad (1.2)$$

where $|x\rangle_{1,2}$ represents qubit one and two respectively. It is clear from the above expression that if a measurement is performed on the first qubit, the state of the second qubit is automatically known.

It is also important to remark that these correlations remain even if the measurement happens in a different basis, that is, if we write $|0\rangle \rightarrow (|+\rangle + |-\rangle)/\sqrt{2}$ and

$|1\rangle \rightarrow (|+\rangle - |-\rangle)/\sqrt{2}$. Although spooky, entangled states are routinely created in experiments around the world and have been demonstrated to exhibit correlations that exceed classical predictions [13, 14].

1.1 Ion trap based quantum computing

Current efforts for building a quantum computer include both solid state (NV, superconductors) and atom based systems. Although extensive documentation and comparisons can be found in the literature [15], I will not discuss the features of each platform, instead I will focus on the description of ion trap systems.

Trapped ion based systems are one of the most mature platforms for quantum computing since the first demonstration of near perfect state detection [16–18] and two qubit entanglement [19] has been shown in such systems. Moreover, long coherence times [20], error correction [21] and high fidelity gates [5, 6] have also been demonstrated in the past years, opening the door for control of larger qubit numbers [10]. These systems employ rf Paul traps that harmonically confine positively ionized atoms in a linear chain. Two or three dimensional arrays can be also achieved in a controllable way [22], but linear chains are usually preferred due to simplicity.

The qubit states are commonly defined by two distinct electron states which can either be optical or different hyperfine states due to their robustness to external noise and long lifetimes. Communication between qubits is achieved by coupling to their motional degrees of freedom that serve as a quantum bus and allows full qubit

connectivity [10]. Motional states are best described in terms of quantized normal modes and are coupled to the qubits by laser light, which provides a reliable and high degree of control. When the motional wavefunction of the qubit is smaller than the reduced wavelength of the laser light ($\lambda/2\pi$), the ion is said to be confined in the Lamb-Dicke regime [23, 24]. In this regime, the coupling between the spin and the motional levels is such that high momentum transfer is suppressed up to second order. Physically, this implies that the motional quantum number n (Fock state) can change by no more than one.

1.1.1 Computation with phonons and qubits

Since we have a system with individual atoms whose motional states can be addressed and controlled, it is natural to ask ourselves why we cannot use the seemingly infinite harmonic oscillator energy levels $\hbar\omega n$ as our quantum computer processor instead of individual qubits. The answer lies theoretically in the amount of information that could be stored and potentially processed in such systems [25] because of their fermionic (qubits) and bosonic (phonons) statistics and quantum coherence in practice.

Specifically, the Shannon entropy describing the amount of information in a system is defined as

$$S = -\text{tr}(\rho \log \rho), \quad (1.3)$$

where ρ is the density matrix and in this section, it will describe a system with maximum unbiased ignorance (statistical mixture), which is diagonal in the compu-

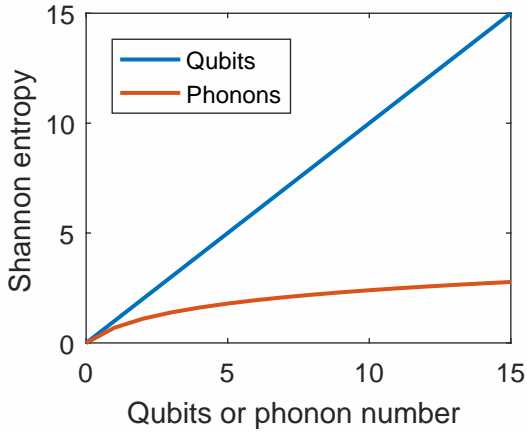


Figure 1.2: Shannon entropy of a quantum system of phonons and qubits. The amount of information stored in an array of qubits scales linearly with their number while for phonons, it scales logarithmically.

tational basis. For a system with N qubits, $\rho_{kk} = \sum_k^N |k\rangle\langle k|/2^N$ we compute

$$S_{\text{qubits}} = -\text{tr}(\rho_{kk} \log \rho_{kk}) = -\sum_k^{2^N} \frac{1}{2^N} \log_2 \left(\frac{1}{2^N} \right) = N, \quad (1.4)$$

that is, we double the processing power for every added qubit. We then compare the qubit system with one made out of $N + 1$ phonons, the $+1$ accounts for the vacuum state. The density matrix for a N occupied phonon system is $\rho_{nn} = \sum_n^N |n\rangle\langle n|/(N + 1)$ and the information entropy is given by

$$S_{\text{phonons}} = -\text{tr}(\rho_{nn} \log \rho_{nn}) = -\sum_n^{N+1} \frac{1}{N+1} \log_2 \left(\frac{1}{N+1} \right) = \log_2(N + 1). \quad (1.5)$$

We notice from the above expression that although we have an infinite amount of energy levels, the information stored in such systems scales poorly compared to the N -qubit case. Moreover, it is experimentally found that motional states are fragile and prone to couple to the environment due to unavoidable noise, leading to decoherence. Also, the apparent large number of energy levels is also limited in practice due to trap anharmonicities. On the other hand, atomic qubits are identical

to each other and due to their physical properties, they can be made insensitive to noise up to second order.

Although the use of phonons as a quantum information unit is senseless in both theory and experiment, they are commonly manipulated in multi-qubit systems as a quantum bus for communication between atoms mediated by spin-motion entangling operations, such as the Mølmer-Sørensen [26, 27] interaction, where entangling operations couple single modes of motion with the spin of the ion. Unfortunately, scaling these operations is increasingly difficult due to the bunching of individual motional modes caused by internal ion chain interactions and can result in a gate slow down or added complexity of the control forces. This problem is known as *spectral crowding* and severely limits the scalability of single chain ion quantum computing.

1.1.2 The $^{171}\text{Yb}^+$ qubit

For the experiments described in this thesis, we trap $^{171}\text{Yb}^+$ and $^{174}\text{Yb}^+$ ions. Their main properties stem from their nuclear spin, $I=1/2$ for the 171 and $I=0$ for the 174 isotopes. The $^{171}\text{Yb}^+$ ion is used throughout this thesis as the qubit due to its ground “clock” states hyperfine levels $|F = 0, m_F = 0\rangle \equiv |0\rangle$ and $|F = 1, m_F = 0\rangle \equiv |1\rangle$ 1.3 that defines the qubit states in the $^2S_{1/2}$ manifold (see fig. 1.3) separated by $12\ 642\ 812\ 118.5 + (310.8)B^2$ Hz, where F is the total angular momentum of the atom, m_F is the projection along the quantization axis, the quadratic B terms accounts for the second-order Zeeman shift and B is the magnetic field in units of

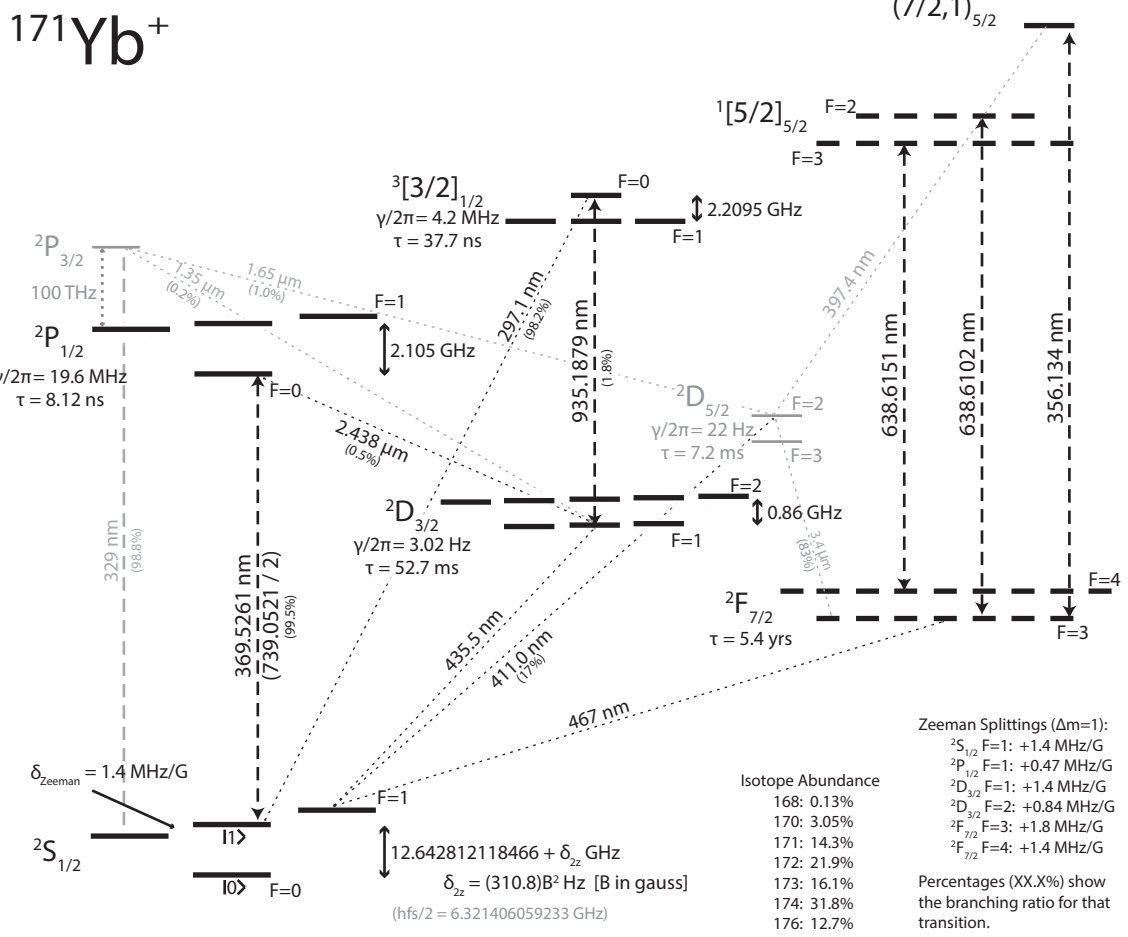


Figure 1.3: Energy level diagram of $^{171}\text{Yb}^+$. The qubit states are defined by the hyperfine levels in the $^2\text{S}_{1/2}$ manifold due to its first order robustness to fluctuating magnetic field.

gauss. We chose such states due to their natural robustness to first order magnetic field fluctuations. Moreover, its strong cooling transition (See chapter 2) at 369.5 nm is within reach of standard frequency doubling techniques. Our system is then best described as the tensor product of the internal states and motional states.

1.1.3 Spectral crowding and approaches to scalability

The normal modes of the ion chain oscillations are of two kinds, axial and transverse. While the axial are well spaced and their separation is almost constant, the transverse are not and their structure is more complicated. Transverse modes are commonly used for quantum computing applications of heavier ions since they are easier to cool down to the ground state and their frequency tuning is less restrictive compared to the axial modes. When the number of ions trapped in a chain increase, there is a bunching of such transverse modes around the common mode frequency. This problem is also known as *spectral crowding* and is an important experimental issue since the interactions that can resolve individual frequencies must be extended in time.

For example, figure 1.4 shows the motional spectrum of both transverse (blue) and axial (red) modes on the blue sideband for 55 ions harmonically confined with frequencies $(\omega_z, \omega_r)/2\pi = (0.2, 4.2)$ MHz along a chain. The MATLAB code can be found in Appendix A [28].

We notice that for the transverse modes, the spectrum bunches around the highest frequency (the common mode) at radial frequency ω_r and the closest transverse frequencies are separated by 4.8 kHz implying that a minimum interrogation time of about 200 μs is required to properly resolve them. Furthermore, because we perform several operations per experimental shot, the total duty cycle can reach several seconds, making the whole computation more vulnerable to noise picking.

Axial modes (red) could instead be employed and would solve the spectral

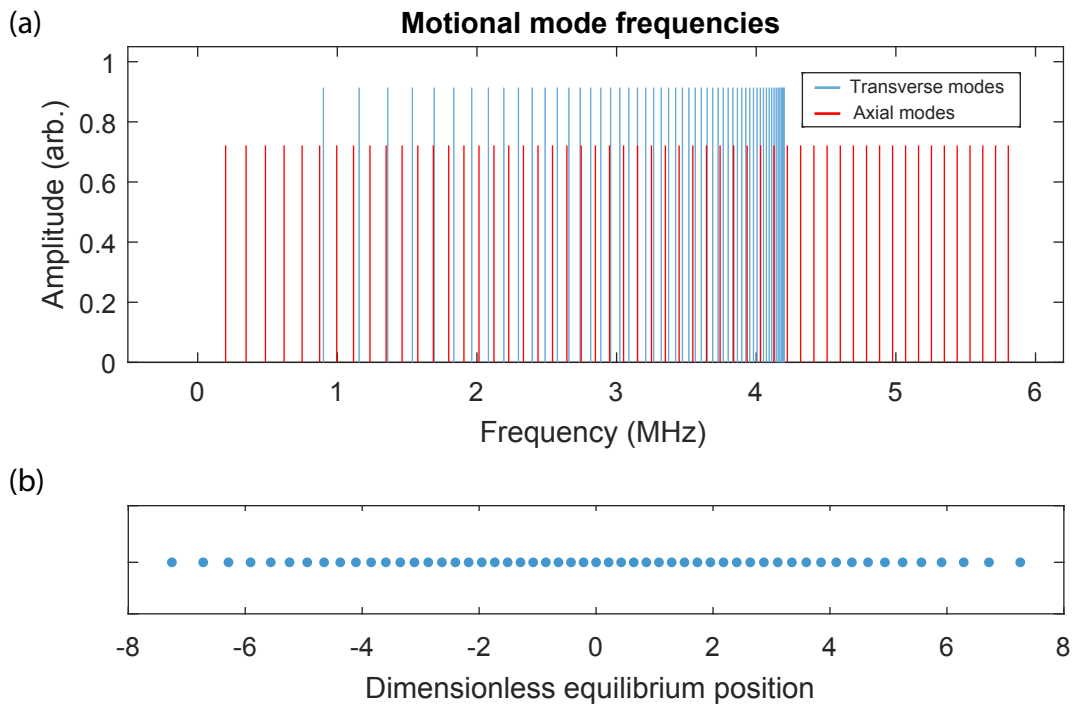


Figure 1.4: Spectral crowding in a chain of 55 ions. (a) First order motional transverse (blue) and axial (red) sidebands showing a spectral bunching at the transverse common mode frequency. Spectral crowding complicates the scalability of single linear chain quantum computers based on Mølmer-Sørensen type operations since longer interrogation times on the sidebands are required for motional coupling. The longer interaction times make operations sensitive to external noise picking. (b) Equilibrium positions of a linear chain. The uneven spacing at the end positions is due to the Coulomb force of the inner ions acting on the outer ones. This same Coulomb interaction produces the spectral crowding.

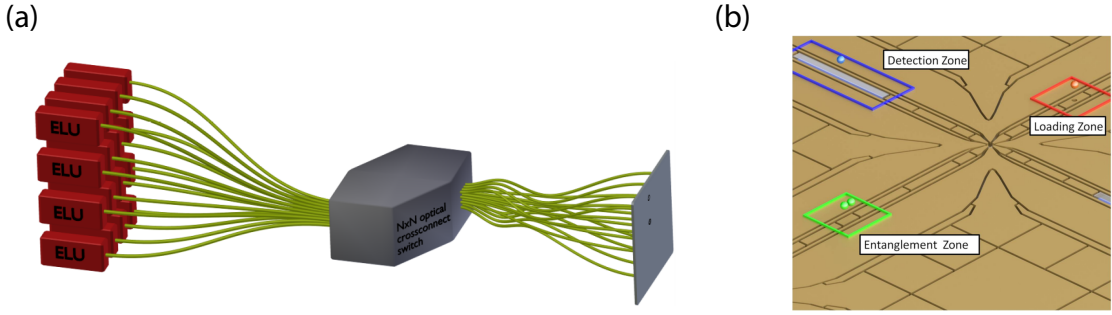


Figure 1.5: Alternatives for scaling up an ion-based quantum processor. (a) The modular approach makes use of individual traps containing ion chains as an elementary logical unit (ELU). The units are connected to an optical switch that routes and entangles the ELUs. (b) In the shuttling approach, the ion trap is divided in specialized zones for entanglement, loading and detection. Ions are shuttled from one zone to another by a predefined set of changing DC biases.

crowding issue since they are more evenly separated (about 1 kHz of separation in the example of fig. 1.4) and easily resolved in the frequency domain but they come at the cost of being lower frequency. At a experimental level, the axial common mode (lowest frequency) is prone to pick DC electrical noise and its low frequency makes cooling difficult with standard techniques.

Two solutions have been proposed to ameliorate this scalability problem. On one hand, single traps can be taken as elementary logical units (ELU) of a larger modular system (see fig 1.5a) interconnected by photonic links [29]. In the ion-photon approach, a lower ion number is stored in each ELU, thus avoiding spectral crowding. However, because photon heralding is required, the experimental duty cycle is bound to be slow due to the probabilistic nature of the operation.

As another avenue, shuttling ions in and out of designated interaction regions (see fig 1.5b) is one potential solution to this issue [30] but is subject to increased noise and heating that degrades coherent operations.

1.1.4 Thesis outline

I present in this thesis the fundamental entangling operation of a different scaling approach that uses impulsive optical forces [31–36] from picosecond pulses. These ultrafast qubit state-dependent kicks occur much faster than the normal mode frequencies of motion and thus can couple through local modes of motion without perturbing spectator trapped ion qubits. This ultrafast approach has the added benefit of being less sensitive to relatively slow noise, and is also insensitive to the thermal motion of the ions since it is effectively frozen during the interaction. Unlike other Coulomb-based gates between ions, ultrafast entanglement operations do not require confinement to within the Lamb-Dicke regime.

The construction of a fundamental gate with ultrafast pulses is the main focus of this thesis with the following outline:

- Chapter two outlines the experimental apparatus and unique features of the experiment. Although the reader is recommended encouraged to read references [37,38], we will expand the concepts, vision and insight of the tools used for our demonstration. The chapter starts with basic concepts of ion trapping and discusses a scheme where two or more drive frequencies are used, highlighting its advantages. We then discuss our trap frequency lock (sensitive to the rf amplitude that we feedback), automatic loading of many ions, and expand a few concepts on state preparation. Finally, we discuss the characterization of our high resolution imaging system for one and two ions.

- Chapter three describes the basic laser-ion spin interactions with ultrafast pulses. I send individual pulses from a mode-locked laser and describe the interaction through Raman transitions. I restrict the discussion to coherent quantum control of the internal states and show the necessary experimental conditions for such spin manipulations.
- Chapter four describes the basic concepts needed for motional control. We calculate the resulting motional wavefunction after interaction with two counterpropagating Raman pulses and develop the theory and experiment of our basic operation involving impulsive momentum kicks. Moreover, we also show a crossover between the ultrafast and quasi-CW regime.
- The fifth chapter covers methods used for benchmarking our base interaction . It also shows results from experiments for sampling the ion motional state and the creation of non-trivial motional states such as mesoscopic quantum superpositions and multicomponent “cat” states.
- Chapter six describes our demonstration of entanglement with ten pulses where we demonstrate a generation of a Bell state with $(76 \pm 1)\%$ fidelity.
- Chapter seven concludes with afterthoughts and possible future directions.

The present thesis is based on the following publications:

1. *Sensing Atomic Motion from the Zero Point to Room Temperature with Ultrafast Atom Interferometry*, Phys. Rev. Lett. **115**, 213001 (2015).

2. *Active stabilization of ion trap radiofrequency potentials*, Rev. Sci. Instrum. **87**, 053110 (2016).

3. *High-resolution adaptive imaging of a single atom*, Nat. Photonics **10**, 606-610 (2016).

4. *Ultrafast creation of large “cat” states of an atom*. Nat. commun. (2017).

5. *Demonstration of two-atom entanglement with ultrafast optical pulses*. Submitted (2017).

I was the coleading author in **1,2,4** and leading author in **3,5**. Works **1** through **4** where done with Kale Johnson as the senior grad student and my only labmate and **5** was done together with Steven Moses as also my only labmate. Some of the presented material is directly from the papers and is referenced as such.

Chapter 2: The Apparatus

I describe the experimental setup used for all the work presented in this thesis. A throughout description of the vaccuum and trap systems is given in [37–40] and will not be described here. I instead give an overview of ion trap theory and its generalization described by the Hill’s differential equation, where some of its particular cases have been used for multispecies trapping [41]. I will describe a scheme to lock the trap frequency to an stable reference, two-photon ionization, show a loading method for large chains using an adaptive technique and prepare the qubit in a predefined state. We finalize, by providing an extensive description of the imaging system with focus on aberration correction and detection of two ions.

2.1 Linear Rf Traps

Gauss’ law in free space ($\vec{\nabla} \cdot \vec{E}$) forbids the creation of a stable equilibrium point with electrostatic fields since flux conservation is imposed. A time varying inhomogeneous electric field is not subject to such constraint because its time averaged force is not zero [42]. Confinement is then achieved through oscillating rf electric fields whose gradients create a harmonic pseudopotential that pushes the ion towards regions of lower field. For our experiments, we used a linear trap with four

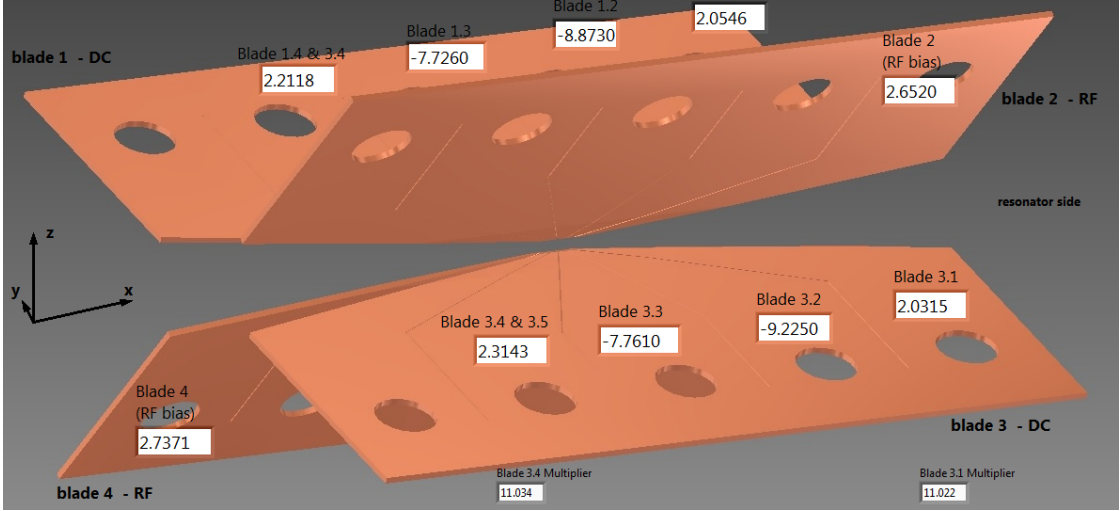


Figure 2.1: Blade trap. Four segmented gold-plated blades are mounted in an insulating mount in Ultra high vacuum (UHV). Due to blade alignment, the rf null where the ions equilibrate is not necessarily the geometric center. The separation of the trapped ions to the nearest blade is about $R \approx 200 \mu\text{m}$ and was made bigger than other trap designs to avoid damage from high power UV radiation.

segmented gold-plated blade electrodes (see fig. 2.1) in ultra high vacuum (UHV) at 10^{-11} Torr to avoid collisions from residual gas with the ions and improve isolation. Opposite blades are rf driven respect the other two held at constant field and the outer static field blades aid in the axial confinement near the trap axis. The total potential at the trap center is

$$V(x, y, z) = \frac{\mu V_0}{2} \left[1 + \frac{(x^2 - y^2)}{R^2} \right] \cos \Omega_{\text{rf}} t + \frac{\kappa U_0}{Z^2} \left[z^2 - \frac{(x^2 - y^2)}{2} \right], \quad (2.1)$$

where μ and κ are geometrical factors [43], Ω_{rf} is the drive frequency, R (Z) are the distances between ion-electrode transversally (axially) and V_0 (U_0) are the drive amplitude and axial voltage respectively.. While hyperbolic electrodes would give a true harmonic pseudopotential, a blade trap closely approximates such behavior at the center of the trap. Specifically in our system, the ion-blade distance is $R \approx 200$

μm in our trap and implies that, at the trap center, we can neglect anharmonic terms up to several microns from the position of the ions, which for practical purposes is large compared to the ion wavefunction ($\approx 5 \text{ nm}$). Moreover, it has been shown that the contributions of anharmonic terms in similar traps are less than 0.1% [44]. Together with the above arguments and the results of Section 5.3 showing harmonicity at practical positions away from the trap center, we neglect such extra expansion terms.

A charged particle trapped at the center of the trap will feel a harmonic ponderomotive force with oscillation “secular” frequency

$$\omega = \frac{e\mu V_0}{\sqrt{2}mR^2\Omega_{\text{rf}}}, \quad (2.2)$$

where m is the mass of the particle, e is the electric charge of the ion and will axially oscillate with frequency

$$\omega_z = \frac{1}{Z}\sqrt{\frac{2e\kappa U_0}{m}}. \quad (2.3)$$

The equations of motion are

$$\ddot{r}_i + [a_i + 2q_i \cos(\Omega_{\text{rf}}t)] \frac{\Omega^2}{4} r_i = 0 \quad (2.4)$$

with

$$a_x = a_y = -\frac{1}{2}a_z = -\frac{4e\kappa U_0}{mZ^2\Omega^2}, \quad (2.5)$$

$$q_x = -q_y = \frac{2eV_0}{mR^2\Omega^2}, \quad q_z = 0. \quad (2.6)$$

These equations of motion resembles a Mathieu equation [23]. At this point, it is natural to ask What is the effect of another drive at different frequency or

an arbitrary periodic time dependent function $f(t)$? In fact, such equation can be described by a Hill differential equation

$$\ddot{x} + f(t)x = \ddot{x} + \left[c_0 + \sum_{n=1}^{\infty} c_n \cos(2nt) \right] x = 0. \quad (2.7)$$

where $f(t+T) = f(t)$. This problem has been studied for the trapping of ion species with large differences in charge-to-mass ratios (of more than a million fold) [41] and notice that the Mathieu equation (eq. 2.4) is a special case of 2.7.

Usual experimental conditions employ a single frequency and are subject to external stray electric fields E_{stray} that shift the ion equilibrium position. The equations of motion for such systems take the form

$$x(t) = x_0 \underbrace{\left(1 + \frac{q_i}{2} \cos(\Omega_{\text{rf}}t + \phi_\mu) \right)}_{\text{intrinsic micromotion}} \cos(\omega t) + \underbrace{\frac{eE_{\text{stray}}q_i}{2m\omega^2} \cos(\Omega_{\text{rf}}t + \phi_\mu)}_{\text{excess micromotion}} + \underbrace{\frac{eE_{\text{stray}}}{m\omega^2}}_{\text{dc offset}}, \quad (2.8)$$

where $q_i = \frac{2e\mu V_0}{mR^2\Omega_{\text{rf}}^2}$ is usually $\ll 1$. The terms that depend on $\cos(\Omega_{\text{rf}}t)$ are known as “micromotion”.

The micromotion in Paul ion traps is an ubiquitous form of driven motion caused by the trapping rf field and can be separated into two contributions: The component modulating the harmonic motion intrinsic to the drive ac field and the second term of eq. (2.8) being the excess of micromotion caused by the external field. Differently from the secular motion, this excess of micromotion cannot be decreased by standard laser cooling methods because of its driven nature. Moreover, its presence is usually detrimental for the precise control of the motion of the ion. Cancelling of such micromotion is done by applying a $-E_{\text{stray}}$ through a definite set of offset voltages.

2.2 Trap frequency stabilization

Stability of the trap frequency (eq. 2.3), which depends on the amplitude of the rf field applied to the electrodes V_0 , is crucial because it directly affects the ability to coherently manipulate the motional degrees of freedom. The rf circuitry involved in the Paul trap is susceptible to environment and electrical fluctuations such as picked noise from the environment, amplifier noise, temperature drifts, etc. that greatly degrades the coherence. We actively stabilize the trap frequency [45] by noninvasively probing and rectifying the high rf voltage, to measure the amplitude of the applied electric field, right before it reaches the ion trap. As shown in the schematic of fig. 2.2, an rf signal at $\Omega_{\text{rf}}/2\pi = 17$ MHz and -8 dBm is produced by an rf oscillator (SRS DS345) and sent through the local oscillator (LO) port of a level 3 frequency mixer (Mini-Circuits ZX05-1L-S), with a conversion loss of 5.6 dB. The RF port of the mixer is connected to a rf amplifier (Mini-Circuits TVA-R5-13) with a self-contained cooling system, providing a gain of 38 dB. The amplifier signal is fed into an antenna that inductively couples to a 17 MHz quarter-wave helical resonator and provides impedance matching between the rf source and the circuit formed by the resonator and ion trap electrode capacitance [46]. The antenna, resonator, and equivalent ion trap capacitance C_{trap} are shown in Fig. 2.2, and exhibit an unloaded quality factor $Q_U \sim 600$. A capacitive divider samples roughly 1% of the helical resonator output, using $C_1 = 0.2$ pF and $C_2 = 20$ pF ceramic capacitors (Vishay's QUAD HIFREQ Series) with temperature coefficients of 0 ± 30 ppm/ $^{\circ}\text{C}$. With $C_1 \ll C_{\text{trap}}$ and residual inductance between the divider and

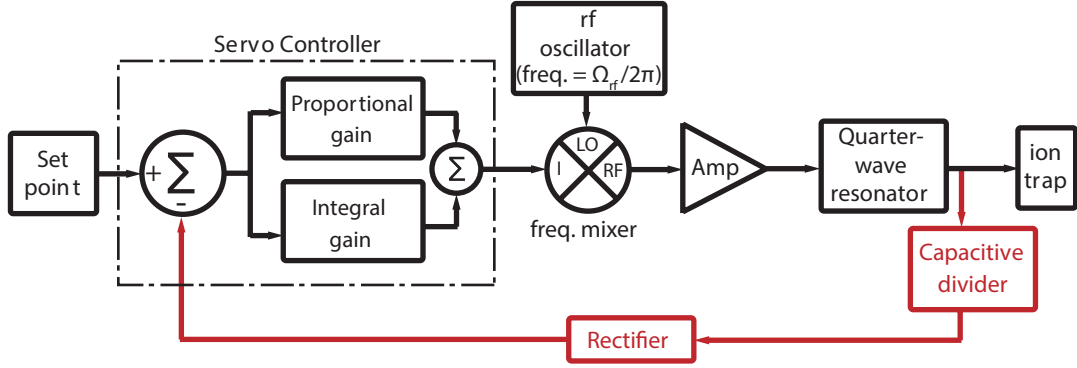


Figure 2.2: Stabilization of the rf field amplitude V_0 only, with fixed rf drive frequency (used in the experiment reported here)

the trap electrodes much smaller than the resonator inductance itself, the divider faithfully samples the rf potential within a few centimeters of the trap electrodes and does not significantly load the trap/transformer circuit. The capacitors are surface-mounted to a milled copper-clad epoxy circuit board and installed inside the shielded resonator cavity.

2.2.1 Rectifier circuit

The sampled signal passes through a rectifier circuit (fig. 2.3a) consisting of two Schottky diodes (Avago HMPS-2822 MiniPak) configured for passive temperature compensation [47] and a low-pass filter giving a ripple amplitude 10 dB below the diode input signal amplitude. High quality foil resistors and ceramic capacitors are used to reduce the effect of temperature drifts. The entire rectifying circuit is mounted inside a brass housing (Crystek Corporation SMA-KIT-1.5MF) as shown in fig. 2.3b. The sampling circuit has a bandwidth of 500 kHz, limited by the $5 k\Omega_{rf}/68 \text{ pF}$ RC filter. The ratio of dc output voltage to rf input voltage amplitude,

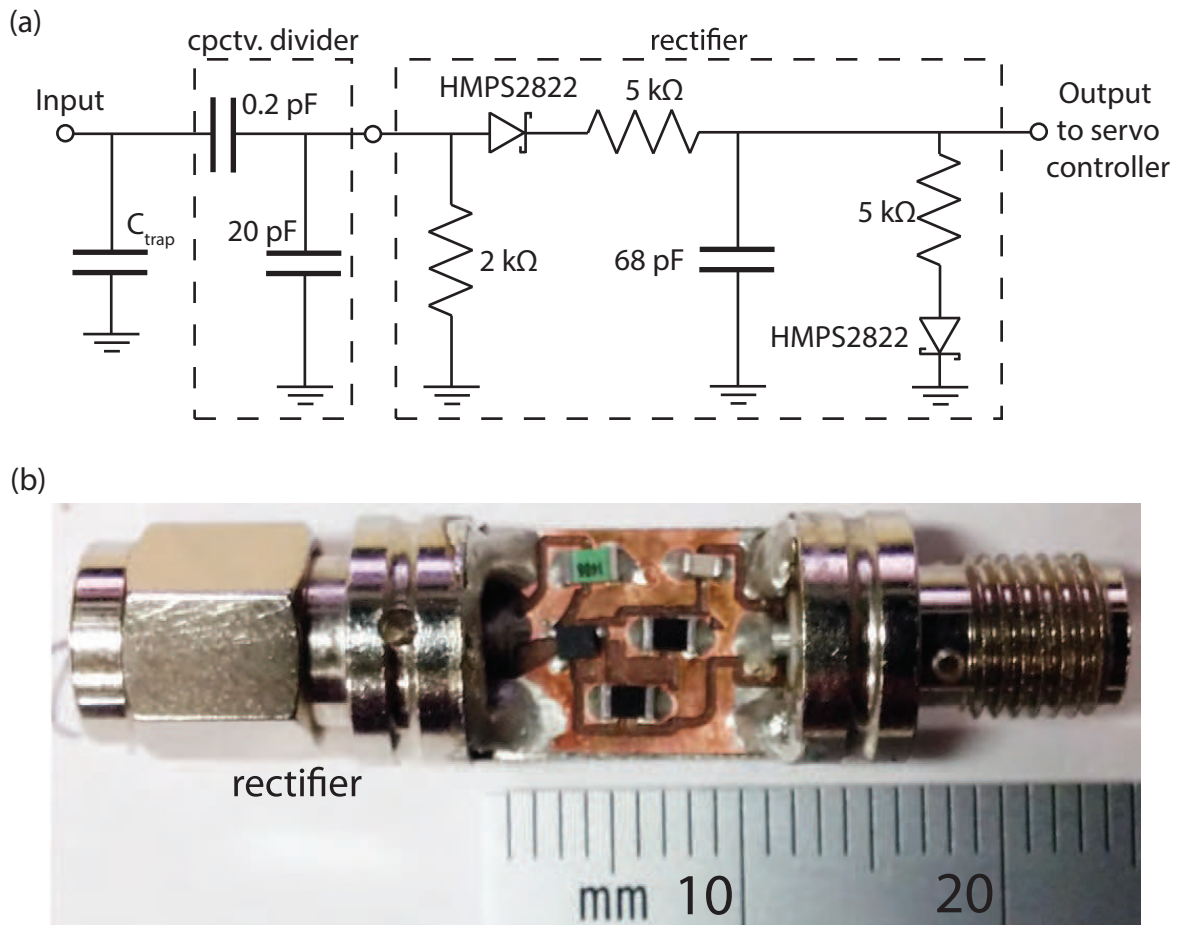


Figure 2.3: Rectifier circuit. (a) A capacitive divider delivers a small fraction of the signal going to the trap. A $2\text{k}\Omega$ shunt resistor grounds the rf signal that does not pass the diode on the negative cycle. The rectifier circuit is tuned in such a way that the ripple and average voltage is optimal. (b) Mounted rectifier circuit in a brass housing. A cylindrical seal on top of the circuit completely isolates it from the environment.

including the capacitive divider, is 1:250 at a drive frequency of 17 MHz, 1:330 at 100 MHz, and 1 : 870 at a drive frequency of 1 MHz.

The rectified dc signal is then compared to a stable set-point voltage (Linear Technology LTC6655 5V reference mounted on a DC2095A-C evaluation board) with variable control (Analog Devices EVAL-AD5791 and ADSP-BF527 interface board), giving 20-bit set-point precision and $\pm 0.25\text{ppm}$ stability. The difference between these inputs the error signal is then amplified with proportional and integral gain (New Focus LB1005 servo controller) and fed back to regulate the upstream rf oscillator amplitude via the frequency mixer described above. The overall frequency response of the feedback loop is limited to a bandwidth of 30 kHz, consistent with the linewidth $\Omega_{\text{rf}}/(2\pi Q)$ of the helical resonator transformer.

2.2.2 Rf amplitude locking results

We confirm the performance of our circuit by performing a Ramsey experiment (see next sections) on the quantized vibrational levels of the ion. The experiment is performed by applying laser light at $\omega_L = \omega_{hf} + \omega$ where ω_{hf} is the qubit energy splitting to measure the frequency of the motional sideband operations since they are mostly affected by the trap frequency. We sample ω at a rate of 2.1 Hz for 80 minutes with no feedback on the rf amplitude, and then for another 80 minutes while actively stabilizing the rf potential. A typical time record of the measurements over these 160 minutes is shown in Fig. 2.4a. Feedback control clearly improves the stability of the ion oscillation frequency

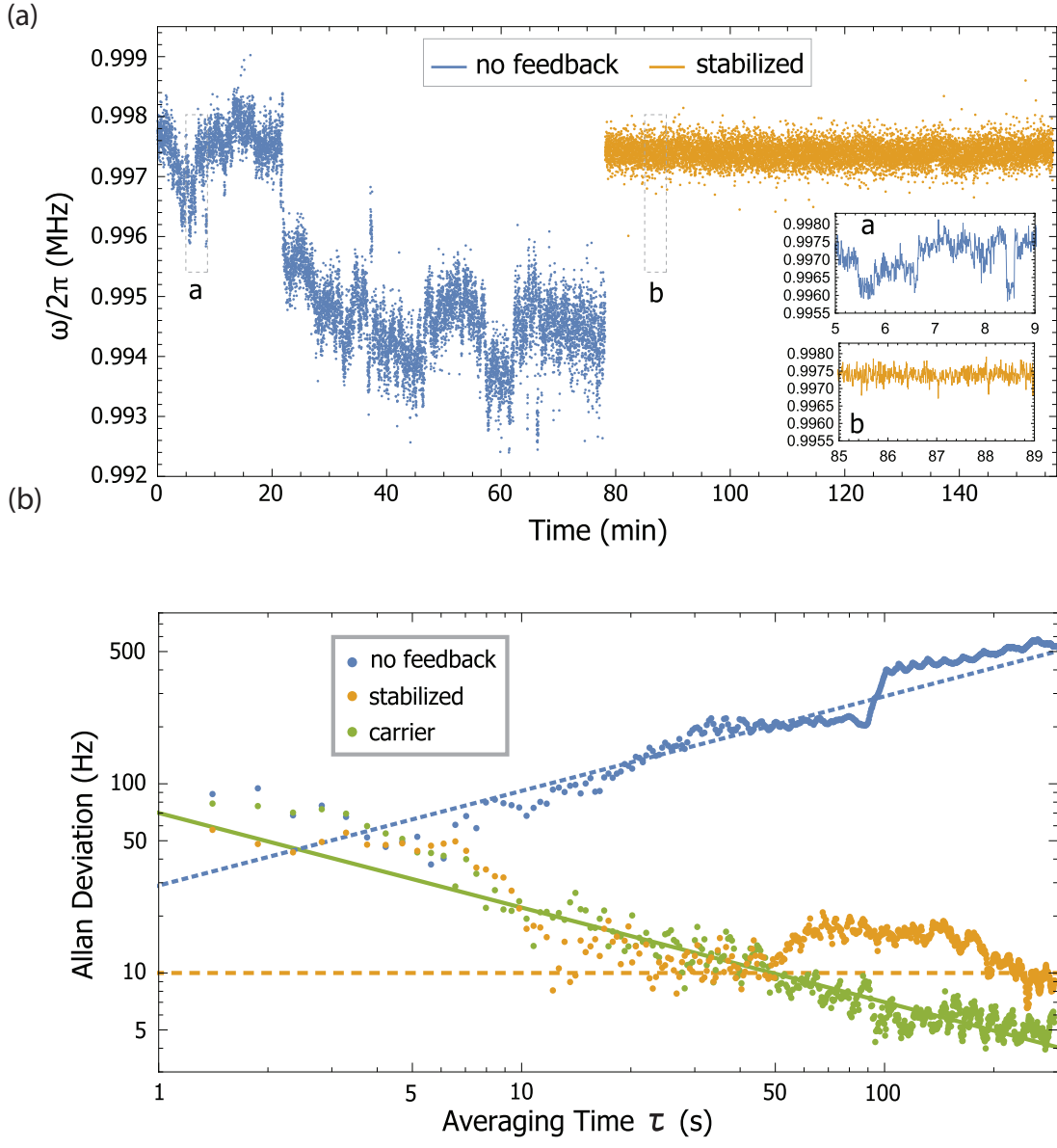


Figure 2.4: Rf amplitude lock performance. (a) Locking performance in the time domain shows clear improvement. The noise on the unlocked system at the first 80 minutes resembles telegraph noise and is not well understood but might stem from mechanical or thermal fluctuations. (b) Allan deviation of (a) for an unlocked (blue) and locked (yellow) system. We see a jump at 50 s and it likely can be caused by drifts on the capacitive divider. The green line shows an Allan deviation from the carrier that is expected to be insensitive to the above noise due its independence to the motional states. The only difference between the yellow and green lines is the presence of trap evolution and motional noise picking.

A way to characterize the stability of an oscillator is to compute its Allan deviation from time series measurements as:

$$\sigma^2(\tau) = \frac{1}{2(M-1)} \sum_{n=1}^{M-1} (y_{n+1} - y_n)^2, \quad (2.9)$$

where M is the number of samples per time bin and y_n are the frequency measurements of the oscillation frequency as a function of integration time τ . When the system is stabilized, the Allan deviation in ω is nearly shot-noise limited (decreasing as $1/\sqrt{\tau}$) up to ~ 200 s of integration time, with a minimum uncertainty of better than 10 Hz, or 10 ppm, representing a 34 dB suppression of ambient noise and drifts (see fig. 2.4b). Without feedback, the trap frequency deviation drifts upward with time. For integration times shorter than 7 s, there is not sufficient signal/noise in the measurements to see the effects of feedback stabilization.

Although the Allan deviation of the oscillation frequency in the stabilized system improves with longer averaging time as expected, it drifts upward for a period just after $\tau = 50$ s (likely caused by a temperature drift affecting the capacitive divider pick-off). We confirm that this drift only appears in the ion oscillation frequency ω and not the driving field ω_L or the ion hyperfine splitting ω_{hf} by performing the same experiment on the qubit transition near beatnote frequency $\omega_L = \omega_{hf}$ instead of the upper sideband. As shown in Fig. 2.4b, the measured Allan deviation of the carrier continues downward beyond $\tau = 50$ s, meaning that the ion oscillation frequency is affected by the rf amplitude at long times.

2.3 Ion loading

Paul traps are loaded with ions that are photoionized from a neutral atomic beam aimed at the center of the rf trap. Laser cooling localizes the atoms within a few nanometers and its internal states are usually manipulated with optical pumping and detection schemes. This section is devoted to further discuss the techniques used in this thesis.

2.3.1 Photoionization

We load Yb^+ ions by photoionizing neutral Yb coming from a thermal beam produced by an atomic oven [48]. The atomic beam is aimed towards the center of the trap together with focused UV Light at 398.9 nm that is resonant to the Doppler shifted ${}^1S_0 \Leftrightarrow {}^1P_1$ transition (see fig. 2.5) of the neutral Yb, providing isotope selectivity. A second energetic photon at 369 nm or 355 nm excites the atom from the 1P_1 state to the continuum. Since more power is available at 355 nm, this is a preferred method for fast loading. The loading rate can be tuned depending on the time this beam is on.

We lower the rf voltage to easily capture ions and continuously send 399 nm, 355 nm and Doppler cooling light. The trapped ions are hot and not crystalized in a linear chain. After trapping the desired number of ions, we raise the trapping potential to form a linear chain. Although the number of trapped ions is random by nature, adaptive techniques can be used to tune the amount of trapped ions

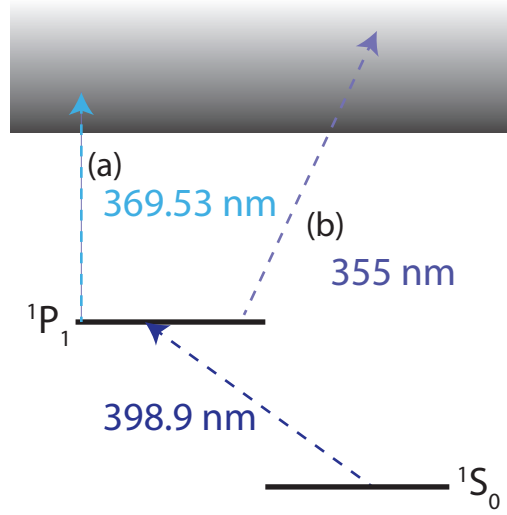


Figure 2.5: Two photon ionization. (a) 369 nm photons routinely used for state preparation and cooling can be used as the second ionizing photon. However, low average powers ($< 1\text{mW}$) are usually achieved due to poor doubling efficiency [38], greatly affecting the loading rates. (b) Tripled light from a Nd:YAG at 355nm is better suited for loading since high average powers are easily achieved. We used 50 mW of this light for loading.

2.3.1.1 Ion autoloader

Loaded ions usually appear suddenly, or can appear one-by-one with appropriate control of the photoionization laser intensity. Once they are loaded, laser cooling (see next section) immediately localizes them to the nanometer-scale in space, and they behave as effective point-source optical objects. The imaging of their fluorescence onto a camera then allows the identification of a trapped ion. Alternatively, trapped ions can be loaded from a complex multi-zone trap [49] whereby individual trapped ions are shuttled from a previously-loaded trap zone to an experimental zone where fluorescence is collected.

For applications involving large qubit arrays, it is important to know exactly

(a)



(b)

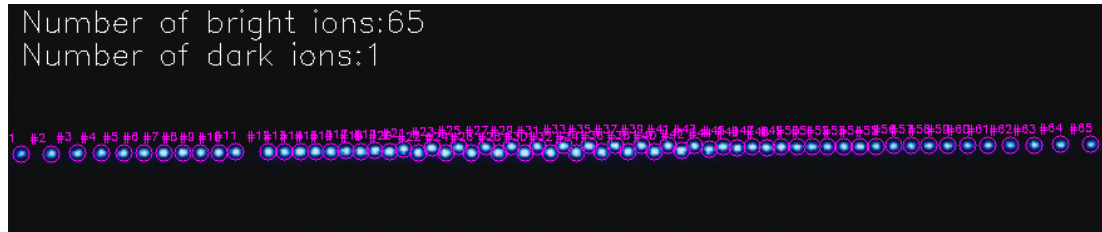


Figure 2.6: Real time adaptive ion number recognition. (a) Fast ion loading is performed by lowering the trap potential since it is easier to capture higher ion numbers. This leads to 2d-3d configurations because the axial confinement is commensurate with the transverse one. We notice that the ion loader accurately identifies the ion number based on the fluorescence and its actual configuration is irrelevant. (b) Linear chain with a dark ion that arise from either different atomic species that do not fluoresce at the cooling frequency or right isotope ions trapped in a nonfluorescing state.

how many ions are confined in the trap. We developed image recognition software to count the ion number as the loading proceeds (code in Appendix B).

The positions of the individual ions are determined by first fitting the overall intensity distribution to a sum of a variable number of Gaussian functions. We quickly determine the peak positions by calculating the Laplacian of Gaussians (LoG) whose zeroes indicate the inflection point of the intensity distribution for each peak. In practice, we use a Difference of Gaussians (DoG) algorithm to quickly approximate the Laplacian, as subtracting two Gaussians with different widths essentially produces the second derivative. This technique returns regions of local maximas, which are easy to find even if the individual atomic images overlap strongly.

During loading there are many conformations, from the simplest 1D line, to 2D zig-zag crystals and then evolving to a series of 3D helical structures [50]. The relative spacings of ions in these configurations can be computer for crystals of up to 100 or more ions. For insufficient anisotropy in the confinement, many ions will form 3D conformations and exhibit out-of-focus images, which may not allow unambiguous identification of individual atoms. However, 1D and 2D structures work well, and even some simple 3D structures can be accurately characterized (see fig. 2.6a). A subset of ions typically do not fluoresce in the image, but their positions are made obvious by the larger gaps in the crystal (see fig. 2.6b). These “dark” ions arise from different atomic species that do not respond to the laser light, or from ions trapped in a nonfluorescing state. These dark ions are often transient, blinking on and off, and their positions, bright or dark, must be recorded to keep an accurate

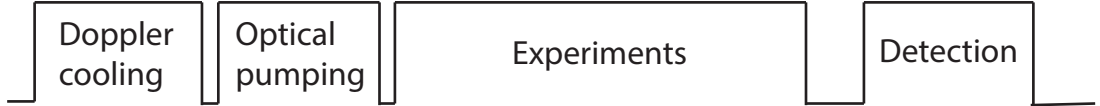


Figure 2.7: Qubit state preparation. Each experimental cycle we Doppler cool the ions to localize them, optically pump their state to the $|^2S_{1/2}, F = 0\rangle$ state and run the experiments often involving a qubit-motion coupling. Detection is performed to the qubit states and allow us to infer the motional evolution.

count of ions and accounting of their positions.

We run software that processes the intensity distribution as described above for rapid ion loading and real-time analysis of ion number while controlling the intensity of the ionizing laser. In this way, we can control the number of atoms loaded in the trap and produce a targeted number of trapped ions.

2.4 Qubit state preparation

A normal experimental sequence is composed of Doppler cooling, optical pumping, experimental operations and detection (see fig.2.7). In this section, we describe in further detail each of these steps. We point out that differently than other ion based quantum computing experiments, we do not use ground state cooling for motional state preparation.

2.4.1 Doppler Cooling

After loading, we send light that is 10 MHz red-detuned from the ${}^2S_{1/2} \leftrightarrow {}^2P_{1/2}$ transition for Doppler cooling. Additionally to the 369.5 nm light, we send 935.2 nm light to pump population out from the metastable ${}^2D_{3/2}$ level, caused by decay

from the ${}^2P_{1/2}$. Doppler cooling localizes the ion with total energy in the directions $i = x, y, z$ (see [51] and Appendix C for the derivation)

$$E_{k_i} = \frac{m \langle v_i^2 \rangle}{2} = \frac{\hbar\Gamma}{8} \left(1 + \frac{f_{si}}{f_i}\right) \left[\frac{\Gamma(1 + \frac{2}{3}s_0)}{4\Delta} \right] + \frac{\Delta}{\Gamma} \quad (2.10)$$

where Γ and Δ are the transition natural linewidth and detuning respectively, $s_0 = I/I_{\text{sat}} = 2\Omega^2/\Gamma^2$ is the fractional saturation transition intensity with Ω as the resonant Rabi frequency, f_{si} is the probability of emission along the i direction (1/3 for isotropic emission) and f_i is the direction of the cooling light

For optimized parameters $\Delta = \Gamma/2$, $s_0 \ll 1$, isotropic emission, even illumination along all directions $f_{si} = f_i = 1/3$ and normal trap frequencies $\omega = 2\pi \times 1\text{MHz}$, we can estimate the mean occupation number \bar{n}

$$E_{k_i} = \frac{\hbar\Gamma}{4} = \hbar\omega \left(\bar{n} + \frac{1}{2} \right) \quad (2.11)$$

$$\bar{n} \lesssim 10.$$

It is clear from eq. 2.11 that higher trap frequencies imply a lower \bar{n} . Although further cooling such as resolved Raman sideband cooling could be employed to obtain temperatures close to the ground state, the experiments described in this thesis do not require this extra step and throughout the remainder of this thesis, we will assume that we work at the Doppler limit unless otherwise specified.

2.4.2 Optical pumping

We continuously send 369.5 nm light for time T_{pump} seconds to initialize the qubit in the $|0\rangle$ state. Since the transition $|{}^2S_{1/2}, F = 0\rangle \Leftrightarrow |{}^2P_{1/2}, F = 0\rangle$ is

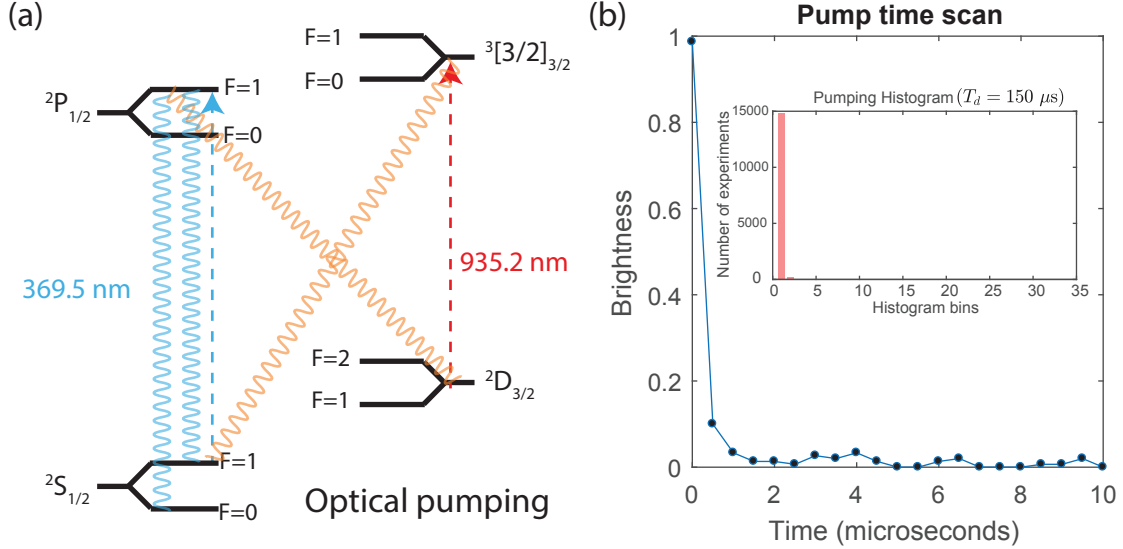


Figure 2.8: Optical pumping. (a) We optically pump to the $|^2S_{1/2}, F = 0\rangle$ state by driving the $|^2S_{1/2}, F = 1\rangle \leftrightarrow |^2P_{1/2}, F = 1\rangle$. (b) Time scan showing the brightness decay for high T_{pump} times. At the end of the pumping cycle, we have initialized the ion in the $|^2S_{1/2}, F = 0\rangle$ state.

forbidden due to selection rules, we generate sidebands at 2.1 Ghz to populate the $|^2P_{1/2}, F = 1\rangle$ states, which have 1/3 probability to decay to the $|0\rangle$ state. Because the $^2P_{1/2}$ states also decay to the $^2D_{3/2}$, we leave the 935.2 nm beam on with its respective sidebands that address all the hyperfine levels of the $^3[3/2]_{3/2}$ state.

2.4.3 Detection

As illustrated in fig. 2.9, we perform qubit detection using fluorescence methods [48] by driving the $|^2S_{1/2}, F = 1\rangle \leftrightarrow |^2P_{1/2}, F = 0\rangle$ transition with 369.5 nm light for time T_d . If the ion is prepared in the $|0\rangle$ ($|^2S_{1/2}, F = 0\rangle$), light will be far detuned from the closest allowable transition in the $|^2P_{1/2}, F = 1\rangle$ state and it will not scatter any light. On the other hand, if the ion is in the $|1\rangle$ state, light will be scattered at a rate given by eq. (C.6).

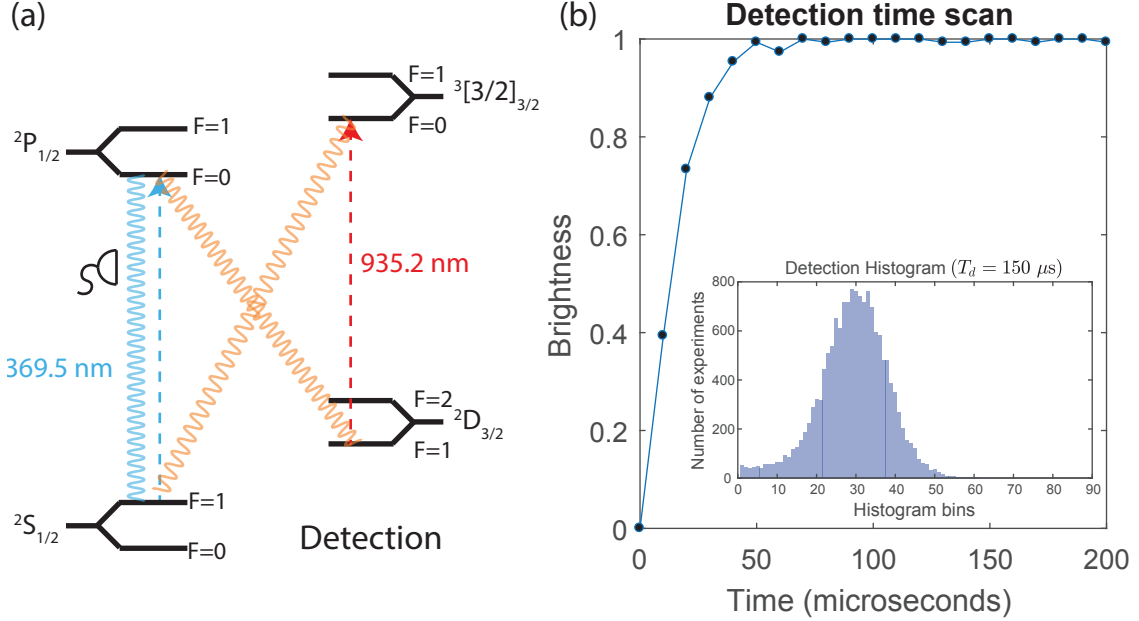


Figure 2.9: Detection scheme. (a) We send resonant laser light to the states $|^2S_{1/2}, F = 1\rangle \leftrightarrow |^2P_{1/2}, F = 0\rangle$. Any decay to the $|^2D_{3/2}, F = 1\rangle$ is pumped back to the $|^2S_{1/2}, F = 1\rangle$ states by resonant 935 nm light that drives the $F=1$ state of the $^2D_{3/2}$ to the bracket state $^3[3/2]_{3/2}$. (b) Time scan showing the brightness saturation for high T_d times. The inset shows a photon histogram of 100 experiments with $T_d = 100 \mu\text{s}$. Notice the tail at the bin 0 caused by off resonant coupling to the $|^2P_{1/2}, F = 1\rangle$ states.

The scattered photons are imaged with a lens array (see section 2.7) to a Photomultiplier tube (PMT). The collected photons then gives information of the ion state and if we collect more than one photon, we say that the ion was in the $|1\rangle$ state. Due to its random nature, the distribution of photons arriving at the detector follows a Poissonian distribution [52], and any deviation from this behavior is due to off-resonant coupling to the $|^2P_{1/2}, F = 1\rangle$ that decays down to the $|^2S_{1/2}, F = 0\rangle$ state.

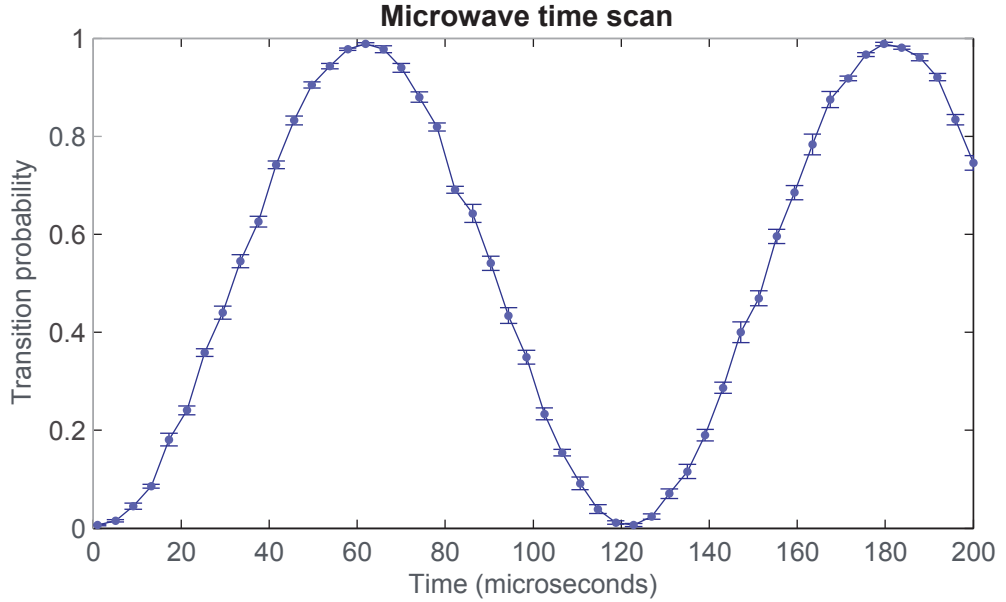


Figure 2.10: Single ion microwave time scan. We send microwaves resonant to the qubit splitting for different times. Rabi flops between the qubit levels are driven by microwaves. Each point represents 1400 experiments and error bars were calculated using the standard error of the mean.

2.4.4 Qubit control with microwaves

We achieve further state control by directly coupling to the magnetic moment of the ion through microwaves producing Rabi flops in the qubit states. Although the same spin manipulation can be done with optical fields, microwaves are preferred due to their simplicity and because they are easy to work with (no beam alignment, frequency tuning is simple and fine polarization tuning is not necessary for driving the clock states). Experimentally, a microwave horn directed towards the center of the trap provides one Watt of power at the qubit splitting frequency. Usual microwave time scans are shown in Fig 3.2. These microwave transitions are about five orders of magnitude weaker than their optical counterpart, due to the weak

coupling of electromagnetic radiation with the magnetic dipole compared to the spin orbit coupling driven by optical fields.

2.5 Imaging system

We collect the fluorescence from the ion at $\lambda = 369.5$ nm using an objective lens of numerical aperture $NA = 0.6$ with 10x magnification. The atomic ion is positioned 11.6 mm from a 4 mm thick vacuum window. The first assembly of six lenses fabricated by Photon Gear, Inc. allows collection from a large numerical aperture with near diffraction-limited performance [53]. After this lens, we place a 128 μm pinhole to spatially filter the scattered light from the ion trap followed by a short focal length lens. 471(3)x overall magnification of the system is found by comparing the lateral displacement of the lens assembly to the corresponding image displacement. As the detector, we use an iXon Ultra 897 electron-multiplying-charge-coupled-device camera (EMCCD) with pixel size of 16 μm . Because angular alignment of the lens assembly is crucial, we correct the tilt with a 5-axis alignment stage (ULTRAAlign 562-XYZ and M-562F-TILT) with angular resolution of 100 μrad . The depth of focus is measured to be on the order of 0.5 μm . The presence of astigmatism, which may stem from clamping of the imaging system or cylindrical warping of the vacuum glass, is corrected by placing a slow cylindrical lens after the short focal length collimating lens. The performance of this design is simulated in ZEMAX with an aberration-free spot size of 374.6nm.

The large collection numerical aperture makes the image quality prone to de-

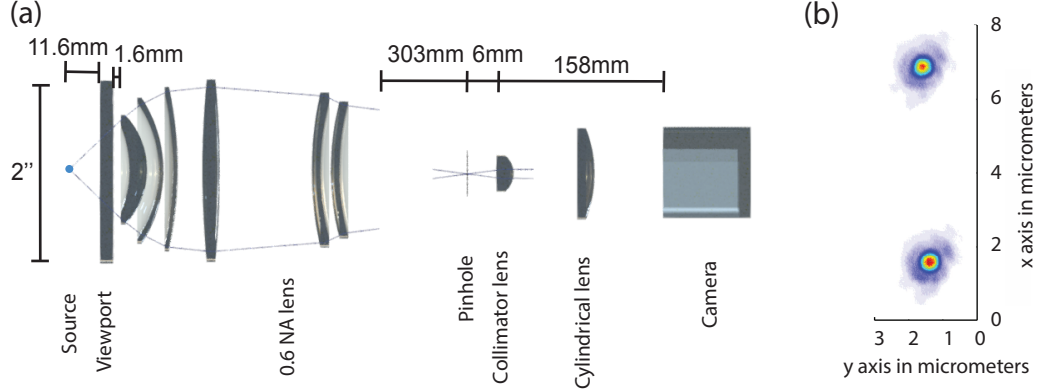


Figure 2.11: (a). Optical setup depicting the source, vacuum window, 0.6 NA objective lens, pinhole, short focal length lens to increase the magnification, cylindrical lens to correct for astigmatism and camera or PMT. (b) Image of the atoms in the real space. At the position of the camera, the two images are separated by $5 \mu\text{m} \times$ Magnification resulting in about 2.5 mm of separation. The large separation at the image plane allows for the detection of each ion with two separate and identical PMTs. (For more details see ref. [54])

formations due to aberrations. These aberrations can be detected by interferometric methods and corrected using deformable mirrors. We instead develop a phase retrieval method and ameliorate aberrations by better alignment and extra optical elements. The methods discussed in this section are described in depth in [54].

2.5.1 Aberration retrieval

The measured spatial distribution of the image is the point spread function (PSF) [55] which contains information about the ultimate resolution achievable in an imaging system and is the building block for more complex image formation through deconvolution techniques. The PSF can be decomposed into Zernike polynomials $Z_n^m(\rho, \theta)$ (See Appendix D) in space

$$\text{PSF}(\rho, \theta) = \left| \mathcal{F} \left\{ \exp \left(-ik \sum_{m,n} c_n^m Z_n^m(\rho, \theta) \right) \right\} \right|^2, \quad (2.12)$$

where $\mathcal{F}\{\}$ is the Fourier transform operator, $k = 2\pi/\lambda$ is the wavenumber and the c_n^m coefficients are contributions of each Zernike component defined in the polar coordinates ρ and θ . The c_n^m coefficients correspond to particular optical aberrations, so detailed characterization of the imaging system follows from the retrieval of the sign and magnitude of these coefficients.

Decomposing an image into Zernike polynomials relies on numerical algorithms [56, 57] or semi-analytical calculations [58]. We obtain a full aberration characterization by using a least-squares fit to the measured data, using the c_n^m coefficients and the exit pupil radius as fitting parameters. Although this method omits consideration of vector (polarization) effects, it remains a generally applicable technique since these effects can be neglected at numerical apertures above 0.6 NA [59].

2.5.2 Fitting algorithm

We use the MATLAB's nonlinear fit algorithm (`fitnlm`) for fitting the aberrations. This routine estimates the fitting parameters using the Levenberg-Marquardt [60] method for nonlinear least squares curve-fitting problems. We use Zernike polynomials (Appendix C) up to the fifteenth order and four additional parameters defining the Gaussian smoothing function ($A \exp(-[(x - x_0)^2 + (y - y_0)^2]/w)$) as fitting parameters. The Gaussian function is introduced to account for mechanical drifts at long integration times as it is convolved with the Zernike PSF. For shot-noise level integration times, this function should not be necessary.

The output of the algorithm gives the coefficient of determination, which is a measure of goodness-of-fit for values close to 1. Furthermore, we obtain the errors on the fitting parameters by taking the diagonal of the square root of the covariance matrix calculated with the above method. We compute the confidence intervals of each fitting parameter by multiplication of the standard error with the Student's t-distribution for 95% confidence.

We do not include the first three Zernike polynomials Z_0^0 (piston), Z_1^{-1} and Z_1^1 (x and y tilt) since they only displace the point spread function and do not model curvature in the wavefront. We find that the error on the Gaussian waist are is negligible.

2.5.3 Position sensing

An additional result making use of our lens resolving power, is the measurement of the sensitivity on the ion position. We take N images at 1 ms exposure time, binning them over total time duration intervals τ and calculating the Allan variance of the central position [61] using eq. 2.9, where M is now defined as the number of samples per bin and y_n is the centroid of the ion image integrated over time τ .

Each image was integrated along one direction and fit to a one dimensional Gaussian linear count density function. The same procedure taken at different times τ leads to a curve of position uncertainty δ_x vs integration time as shown in Fig.

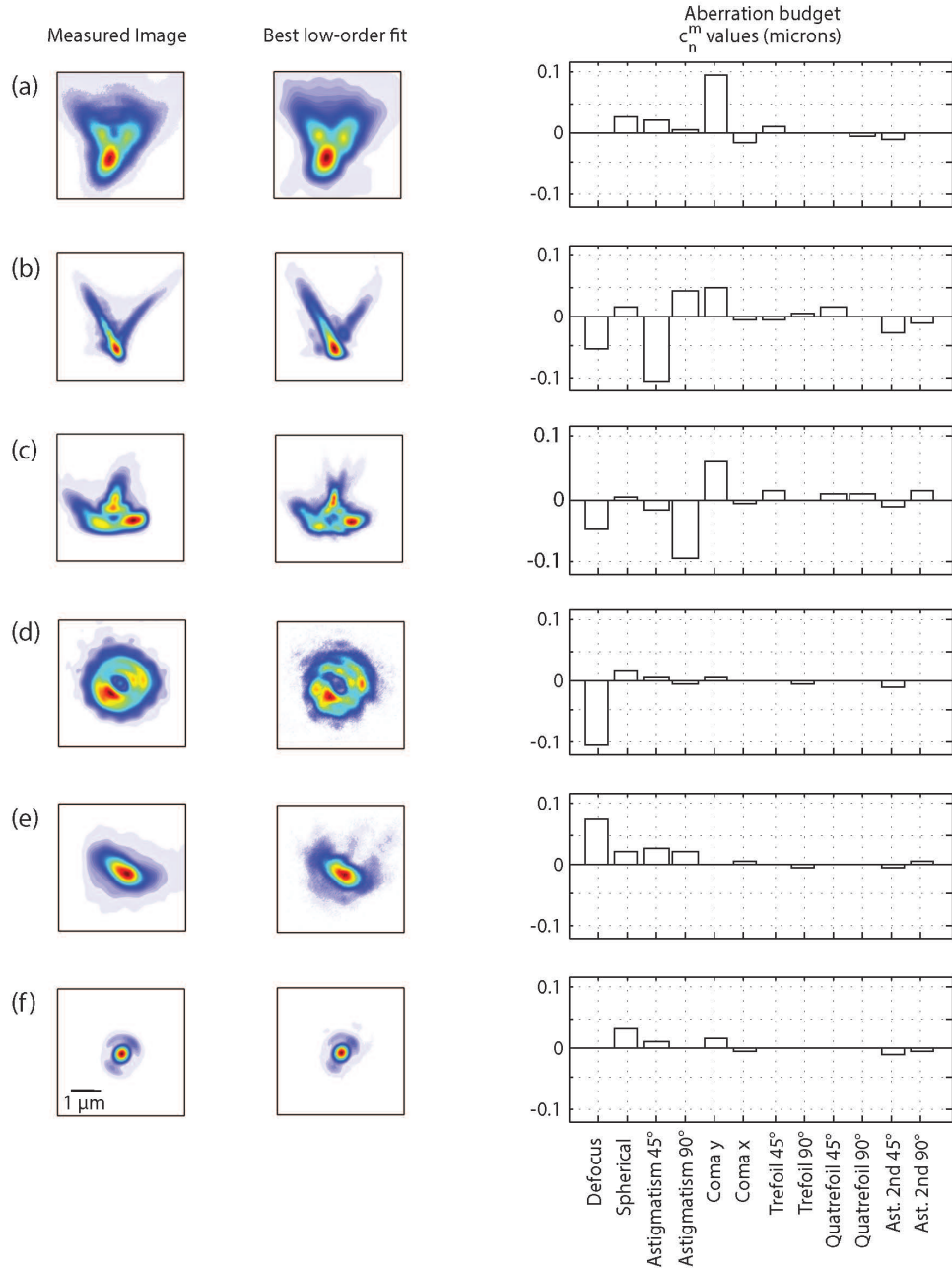


Figure 2.12: Aberration retrieval results. (a,b,c) Single shot images of the misaligned system. (d,e,f) depict the optimally aligned system at various distances from the focal plane, with (f) at the best focus. For (d) and (e) a high contribution from the defocus term is evident with low contributions of astigmatism and coma. Large contributions of coma and astigmatism (a-c) are corrected with a 5-axis stage and cylindrical lens (See text). The goodness of fit obtained for these examples approaches unity at coefficients of determination of 0.989, 0.965, 0.958, 0.957, 0.983 and 0.994 for images (a,b,c,d,e) and (f) respectively. These images are integrated for ~ 0.5 s. Figure from ref. [54]

[2.13](#). The data is corrected for a dead time of 5 ms between each 1 ms frame, allowing for state preparation and laser cooling (See [61, 62]) and Appendix D.

The net position sensitivity is a quadrature of three main (uncorrelated) sources of uncertainty: shot noise, pixelation and background noise [63, 64]

$$\delta_x = \sqrt{\frac{2\rho_0^2}{R_0\tau} + \frac{l_p^2}{12R_0\tau} + \frac{16\pi\rho_0^4 b}{R_0^2\tau^2}} \quad (2.13)$$

where $b \approx 0.07$ is the mean background count rate per pixel, $l_p \approx 33$ nm is the pixel size referred to the object (image pixel size divided by magnification) and $R_0 = \eta_D F \gamma / 2$ is the maximum (saturated) measured fluorescence count rate from the atom, $F \approx 10\%$ is the solid angle fraction of fluorescence collected, and $\eta_D \approx 25\%$ is the quantum efficiency of the camera. Finite pixel size and background counts have negligible impact on the measured position sensitivity in this experiment. The observed sensitivity of $\sim 0.5\text{nm}/\sqrt{\text{Hz}}$ at small integration times is somewhat higher than the expected level of shot noise (shown as the blue line in Fig. 3), and is consistent with observed super-Poissonian noise on the camera. We measure a minimum uncertainty of $\delta_x \approx 1.7(3)$ nm at an integration time of $\tau = 0.2$ s. For longer integration times, drifts in the relative position between the optical objective and the trapped ion degrade the position uncertainty as shown in Fig. [2.13](#), and with simple mechanical improvements in the imaging setup, the resolution can likely be well below 1 nm.

Given this uncertainty in the position of the harmonically-bound ion, the sensitivity to detecting external forces is $\delta F = m\omega_x^2 \delta_x$. For a single $^{174}\text{Yb}^+$ ion with $\omega_x/2\pi = 10$ kHz, this would correspond to a force sensitivity in the yoctonewton

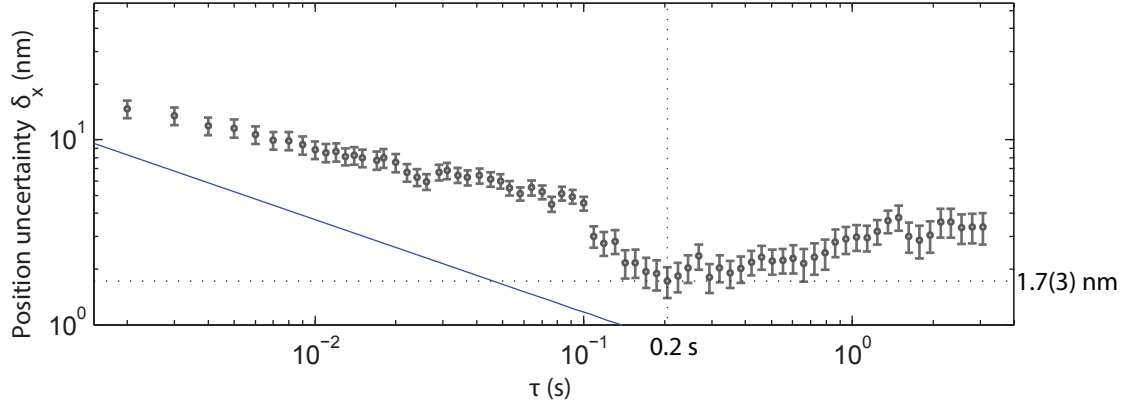


Figure 2.13: Measured position uncertainty δ_x of the trapped ion centroid position versus image integration time τ . The blue line shows the expected uncertainty limited by photon counting shot noise in the imaging system. A sensitivity of $\sim 0.5\text{nm}/\sqrt{\text{Hz}}$ is measured for $\tau < 0.1\text{ s}$, which is ~ 3 times higher than shot noise, presumably from camera noise. The ultimate position sensitivity is found to be $1.7(3)\text{ nm}$ at $\tau = 0.2\text{ s}$. These measurements include small corrections for dead time bias, as described in Appendix E. The error bars on each point are given by the root-mean-square error.

(10^{-24} N) scale, or an electric field at the $\mu\text{V}/\text{cm}$ scale. Unlike earlier work [65], this imaging force sensor applies to single ions and does not require resolution of optical sidebands.

2.5.4 Imaging system for two ions

The high magnification of our imaging system allows high spatial distinguishability between two trapped ions. In real space, they are separated by about $5\ \mu\text{m}$ and due to the ~ 500 magnification, it leads to a separation of about 2.5 mm at the image plane. Using the setup shown in fig. 2.14a, it is possible to individually detect the two emitters by using two identical PMTs and a D-shaped mirror. Figure 2.14a shows a microwave time scan for two ions. Although histogram fitting could

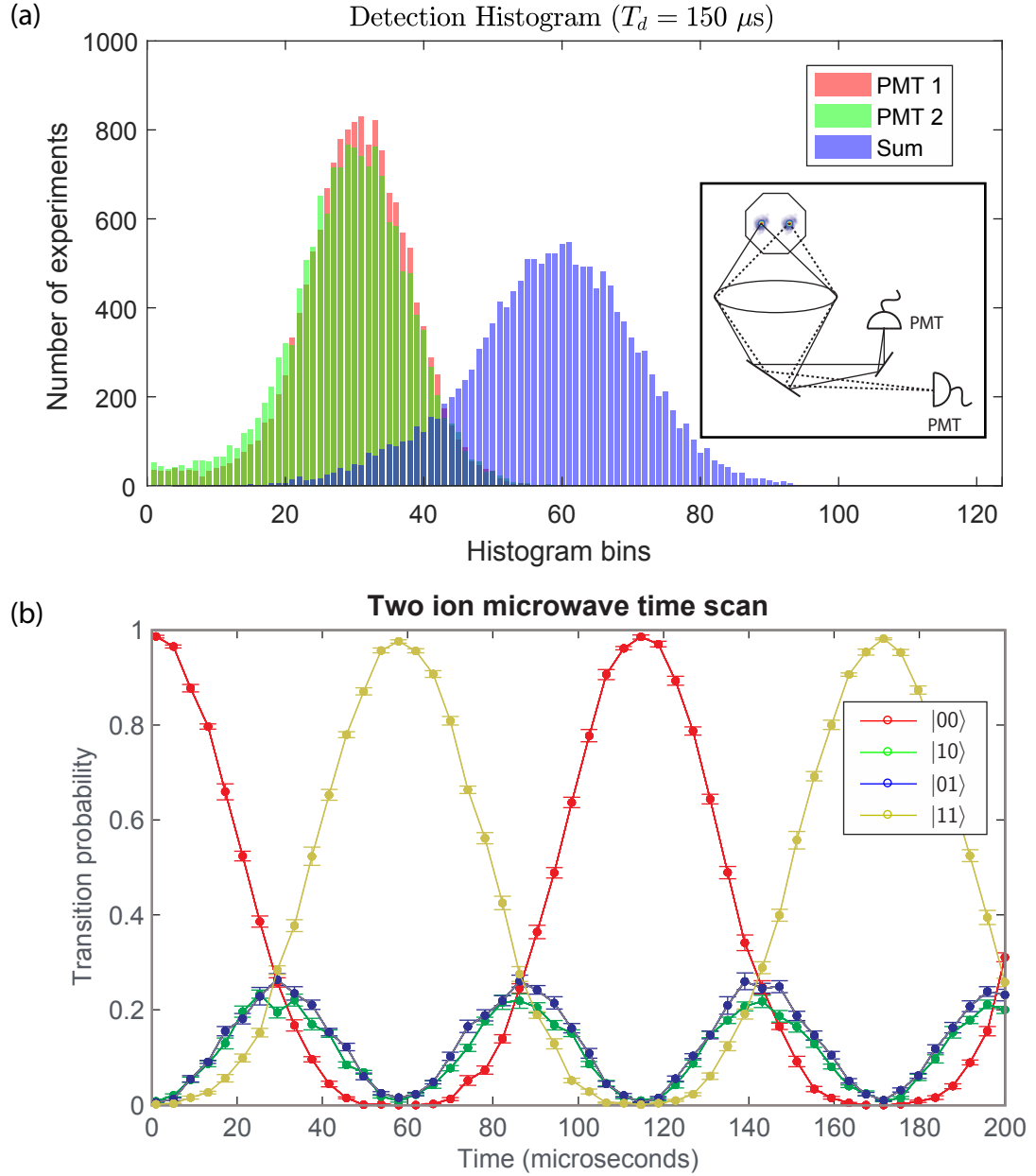


Figure 2.14: Two ion detection. (a) Histogram for 100 shots of 150 experiments with $150 \mu\text{s}$ of detection time depicting the photons arriving at both PMTs. The inset shows a cartoon schematic of the system used with two identical detectors. Small differences between both PMTs do not affect the detection fidelity greatly. (b) Microwave Rabi flopping of two ions showing the correct dependence.

be used for two ion detection with a single PMT, calibration errors makes difficult working with such configuration. After installing the two PMT scheme, we realized that two qubit detection was crucial for demonstrating two qubit entanglement.

Chapter 3: Ultrafast spin control

The biggest challenge in the scaling of any quantum computer technology is qubit interconnection. Ion trap quantum computers are capable of full connection due to the long range interaction of the Coulomb force. However, as the qubit number increases, problems such as spectral crowding (See chapter 1) and qubit addressing severely limits the number to about ~ 100 for a single linear trap. This chapter describes an alternative route for scaling by using interactions faster than any state evolution by means of the spin-orbit coupling through dipole allowed off resonant levels that flip the spin and couple to the motion. The ultrafast excitation described below is achieved by driving Raman transitions from the $^2S_{1/2}$ to the P levels that also provides directionality for flipping either state $|1\rangle \leftrightarrow |0\rangle$. We point out that, contrary to classical computation, faster clock speeds do not affect the scaling of the presented quantum scheme.

We will focus on the basic concepts for spin manipulation and leave the motional control for the next chapter. We start by deriving a general Rabi frequency of a Raman driven interaction and experimentally show spin rotations with a single ~ 20 ps pulse

3.1 Raman spin interactions

Typical operations performed on ion qubits employ laser beams due to the possibility of focusing them and produce high field gradients that affects their motion [23]. We will expand such concept by considering a manifold for a free atom of both ground states $\{|g_1\rangle, |g_2\rangle, \dots\}$ and excited states $\{|e_1\rangle, |e_2\rangle, \dots\}$ ignoring spontaneous emission from the $|e_n\rangle$ states. These states are the ground $^2S_{1/2}$ states or $^2P_{1/2,3/2}$ respectively of $^{171}\text{Yb}^+$ and are an orthonormal basis

$$|\psi\rangle = \sum_n (c_{g_n} |g_n\rangle + c_{e_n} |e_n\rangle). \quad (3.1)$$

If we now consider an interaction H_{int} that only couples to states from a different manifold and substitute 3.1 in the Schrödinger equation we obtain

$$i\dot{c}_{g_n} = \omega_{g_n} c_{g_n} + \sum_m \langle g_n | H_{\text{int}} | e_m \rangle c_{e_m} \quad (3.2)$$

$$i\dot{c}_{e_n} = \omega_{e_n} c_{e_n} + \sum_m \langle e_n | H_{\text{int}} | g_m \rangle c_{g_m}, \quad (3.3)$$

where ω_k is the frequency (relative to some predefined zero) of the state c_k . Following [37] and working in the rotating reference frame, we can define:

$$\tilde{c}_k = c_k e^{i\omega_k t}$$

In the rotating reference frame, our equations become:

$$\dot{\tilde{c}}_{g_n} = -i \sum_m V_{g_n,e_m} \tilde{c}_{e_m} e^{-i(\omega_{e_m} - \omega_{g_n})t}, \quad (3.4)$$

$$\dot{\tilde{c}}_{e_n} = -i \sum_m V_{e_n,g_m} \tilde{c}_{g_m} e^{-i(\omega_{g_m} - \omega_{e_n})t}, \quad (3.5)$$

where we have replaced $V_{i,j} = \langle i|H_{\text{int}}|j\rangle$ for notation shortness.

We want to describe the atom-light coupling and although an atom has no net charge, it will develop an induced dipole moment due to the presence of an electric field. The interaction Hamiltonian is then given by $H_{\text{int}} = -\mu \cdot \text{Re}[\vec{E}]$, where \vec{E} is the incident electric field and we have taken its real part.

We will assume a collection of laser beams with the same frequency ω_L , different wavevectors k_j , phases ϕ_j and polarizations $\hat{\epsilon}_j$ with electric fields defined as

$$\vec{E} = \sum_j \hat{\epsilon}_j \mathcal{E}_j(t) e^{i(\vec{k}_j \cdot \vec{r} - \omega_L t + \phi_j)}. \quad (3.6)$$

The interaction Hamiltonian then becomes

$$H_{\text{int}} = -\frac{\vec{\mu}}{2} \cdot \sum_j \left[\hat{\epsilon}_j \mathcal{E}_j(t) e^{i(\vec{k}_j \cdot \vec{r} - \omega_L t + \phi_j)} + \hat{\epsilon}_j^* \mathcal{E}_j(t) e^{-i(\vec{k}_j \cdot \vec{r} - \omega_L t + \phi_j)} \right], \quad (3.7)$$

which implies

$$\begin{aligned} V_{g,e} &= \frac{1}{2} e^{-i\omega_L t} \left[- \sum_j \mathcal{E}_j(t) \langle g | \vec{\mu} \cdot \hat{\epsilon}_j | e \rangle e^{i(\vec{k}_j \cdot \vec{r} + \phi_j)} \right] \\ &\quad + \frac{1}{2} e^{i\omega_L t} \left[- \sum_j \mathcal{E}_j(t) \langle e | \vec{\mu} \cdot \hat{\epsilon}_j | g \rangle e^{-i(\vec{k}_j \cdot \vec{r} + \phi_j)} \right] \\ &= \frac{1}{2} e^{-i\omega_L t} \Omega_{g,e} + \frac{1}{2} e^{i\omega_L t} \Omega_{e,g}^*, \end{aligned} \quad (3.8)$$

where we have used the fact that the matrix elements $\langle g | \vec{\mu} \cdot \hat{\epsilon}_j^* | e \rangle = \langle e | \vec{\mu} \cdot \hat{\epsilon}_j | g \rangle$ are real and we have defined the complex Rabi frequency $\Omega_{g,e}$

$$\Omega_{g,e} = - \sum_j \mathcal{E}_j(t) \langle g | \vec{\mu} \cdot \hat{\epsilon}_j | e \rangle e^{i(\vec{k}_j \cdot \vec{r} + \phi_j)} \quad (3.9)$$

Substituting equation 3.8 into equations 3.4 and 3.5 and defining a detuning $\Delta_{e_n} =$

$\omega_{e_n} - \omega_L$ we get

$$\dot{\tilde{c}}_{g_n} = \frac{-i}{2} \sum_m \Omega_{e_m, g_n}^* \tilde{c}_{e_m} e^{-i(\Delta_{e_m} - \omega_{g_n})t} \quad (3.10)$$

$$\dot{\tilde{c}}_{e_n} = \frac{-i}{2} \sum_m \Omega_{e_n, g_m} \tilde{c}_{g_m} e^{i(\Delta_{e_n} - \omega_{g_m})t} \quad (3.11)$$

In the above line we have used the Rotating Wave Approximation (RWA) to ignore the terms $\omega_L + \omega_{e_n, e_m}$. We can adiabatically eliminate the excited states by assuming that they will not be populated during the interaction, this is performed by directly integrating 3.11

$$\int_0^{\tilde{c}_{e_n}} d\tilde{c}_{e_n} = \int_0^t \frac{-i}{2} \sum_m \Omega_{e_n, g_m} \tilde{c}_{g_m} e^{i(\Delta_{e_n} - \omega_{g_m})t} dt \quad (3.12)$$

$$\tilde{c}_{e_n} = \sum_k \frac{\Omega_{e_n, g_k} \tilde{c}_{g_k}}{2(\Delta_{e_n} - \omega_{g_k})} \left(1 - e^{i(\Delta_{e_n} - \omega_{g_k})t} \right) \quad (3.13)$$

Substituting in equation 3.10,

$$\dot{\tilde{c}}_{g_n} = \frac{-i}{2} \sum_m \Omega_{e_m, g_n}^* \left[\sum_k \frac{\Omega_{e_m, g_k} \tilde{c}_{g_k}}{2(\Delta_{e_m} - \omega_{g_k})} \left(1 - e^{i(\Delta_{e_m} - \omega_{g_k})t} \right) \right] e^{-i(\Delta_{e_m} - \omega_{g_n})t} \quad (3.14)$$

$$= \frac{-i}{2} \sum_{m,k} \frac{\Omega_{e_m, g_n}^* \Omega_{e_m, g_k}}{2(\Delta_{e_m} - \omega_{g_k})} \tilde{c}_{g_k} e^{i\omega_{g_n} t} (e^{-i\Delta_{e_m} t} - e^{-i\omega_{g_k} t}) \quad (3.15)$$

$$= \frac{-i}{2} \sum_{m,k} \frac{\Omega_{e_m, g_n}^* \Omega_{e_m, g_k}}{2(\Delta_{e_m} - \omega_{g_k})} \tilde{c}_{g_k} (e^{-i(\Delta_{e_m} - \omega_{g_n})t} - e^{i(\omega_{g_n} - \omega_{g_k})t}) \quad (3.16)$$

$$\approx \frac{i}{2} \sum_{m,k} \frac{\Omega_{e_m, g_n}^* \Omega_{e_m, g_k}}{2(\Delta_{e_m} - \omega_{g_k})} \tilde{c}_{g_k} e^{i(\omega_{g_n} - \omega_{g_k})t} \quad (3.17)$$

$$= \frac{i}{2} \sum_k \Omega_{g_n, g_k} \tilde{c}_{g_k} e^{i\delta_{g_n, g_k} t} \quad (3.18)$$

Here I have applied another RWA and have assumed that $\Delta_{e_m} \gg \omega_{g_k}$ for all values of m and k . I have also defined the effective Rabi frequency and the ground state

frequency separation:

$$\Omega_{g_n, g_k} = \sum_m \frac{\Omega_{e_m, g_n}^* \Omega_{e_m, g_k}}{2(\Delta_{e_m} - \omega_{g_k})} \approx \sum_m \frac{\Omega_{e_m, g_n}^* \Omega_{e_m, g_k}}{2\Delta_{e_m}}, \quad (3.19)$$

$$\delta_{g_n, g_k} = \omega_{g_n} - \omega_{g_k}.$$

All the physics involved in the Raman manipulation of our trapped ion is encapsulated in equation 3.19. Further derivation involving numerical values of the matrix elements are found in [37] and will not be discussed here. Instead, we will work with the main result derived from neglecting the differential light shift due to large detuning from the P states when using a 355 nm laser

$$\frac{H_{\text{effective}}}{\hbar} = -\frac{1}{2}\Omega(t)\hat{\sigma}_x - \frac{1}{2}\omega_{\text{hf}}\hat{\sigma}_z, \quad (3.20)$$

where $\Omega(t)$ is a function of the time-dependent light intensity and $\hat{\sigma}_{x,z}$ are the usual Pauli matrices.

3.2 Single pulse rotation

Pulses from a mode locked laser are theoretically described by hyperbolic secant, which after being frequency tripled, become $\text{sech}(t)^3$. For an easier description, such pulses are approximated by $\text{sech}(at)$ functions alone, where a is a fitting parameter that does not affect the physics of the interaction.

The full dynamics of an atom subject to a secant pulse with finite width τ was originally discussed by Rosen-Zener [66] and it is beyond the scope of this section. We instead focus on the final population transfer and not the dynamics during the pulse. For a pulse with large enough bandwidth to drive a two level transition, the

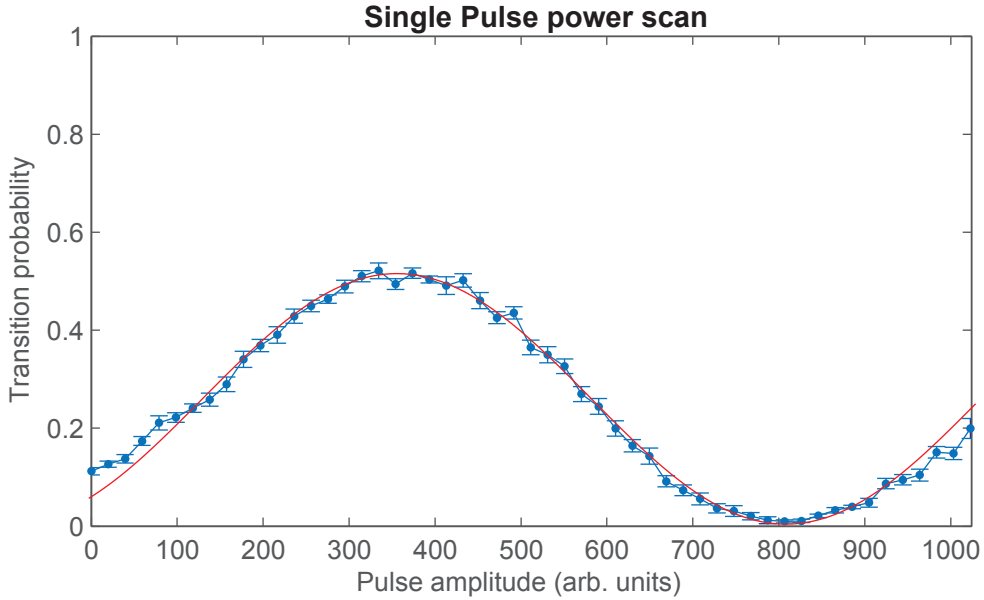


Figure 3.1: Single pulse power scan. By scanning the pulse area θ , we can estimate the pulse duration by recording the transition probability of $|0\rangle \rightarrow |1\rangle$ at each $\Delta\theta$. The plot does not start at 0 because of inefficient switching at low amplitudes. Nonetheless, the important feature is the maximum amplitude that correlates to a pulse duration of 22.2 ps.

probability to drive a $|0\rangle \rightarrow |1\rangle$ is

$$P_{|0\rangle \rightarrow |1\rangle} = \operatorname{sech}^2\left(\frac{\omega_{\text{hf}}\tau}{2}\right) \sin^2\left(\frac{\theta}{2}\right), \quad (3.21)$$

where θ is the pulse area. We notice that the maximum population transfer is bounded by the sech term and is a consequence of the finite bandwidth pulse. We can experimentally test this expression by shinning a single pulse with circular polarization to an ion. The results are shown in fig. 3.1

An immediate consequence of eq. 3.21 is that for a given single non-delta pulse, it is impossible to completely transfer the population to the $|1\rangle$ state. This constraint can be overcomed by using two pulses separated in time such that they constructively interfere and fully drive a transition.

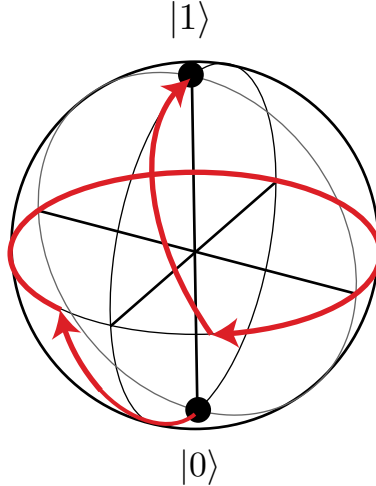


Figure 3.2: Two pulse spin flip. Although a single pulse with sufficient bandwidth is unable to fully transfer all population from $|0\rangle$ to $|1\rangle$, two pulses correctly timed can. The first flips the spin to a superposition of the qubits states, after a definite wait, a second pulse can then transfer all the state to $|1\rangle$.

3.3 Multiple pulses and weak regime

We have assumed in the previous section that a single pulse had enough energy to significantly affect the ion internal state. If now we apply a high number of pulses with a small amplitude ($\theta \ll 1$), we expect each weak pulse to drive a small amount of $\hat{\sigma}_x$ rotations. This intuition is true and we can obtain [34] a transition probability given by

$$P_{|0\rangle \rightarrow |1\rangle} = \operatorname{sech}^2\left(\frac{\omega_{\text{hf}}\tau}{2}\right) \sin^2\left(\frac{\theta}{2}\right) \sin^2\left(\frac{N\varphi}{2}\right) / \sin^2\left(\frac{\varphi}{2}\right), \quad (3.22)$$

where φ is a rotation axis and it is clear that the probability can be made one with the right choice of parameters. As a physical consideration, for $N \geq 1$, we need the repetition rate to be an integer multiple of the hyperfine splitting.

$$\omega_{\text{hf}} = n\omega_{\text{rep}}, n \in \mathbb{Z}, \quad (3.23)$$

that is, the “small” rotation of each pulse should add up in a way that they constructively interfere, leading to population transfer. Experimentally, we need to lock the laser comb beatnote corresponding to the closest frequency of the hyperfine splitting ($\omega_{\text{hf}} = 12.6$ GHz). The next section discusses the schemes that we have used for the three different lasers.

3.3.1 Beatnote lock

Table 3.1: Specs of the lasers used in our experiments.

	Paladin 24W	Paladin 4W	PicoTrain (HighQ)
Average power (Watts)	24	4	“8”
Repetition rate $\omega_{\text{rep}}/2\pi$ (MHz)	81.419	118.305	80.160
Pulse duration τ (ps)	22.2	14.8	7.6

The most straightforward method to match the resonance condition (eq. 3.23) involves the active stabilization of the cavity of the laser for repetition rate tuning. From the three lasers used during my studies (see table 3.1), only the HighQ laser had this capability by giving the flexibility to mount one of the cavity mirrors to a motorized stage and actively feedback the error to a PID control unit. The stabilized 157th harmonic of the repetition rate is the used for coherent operations.

Because not all laser cavities feature a PZT, we used another more flexible and less direct way of stabilizing the laser beatnote using two AOMs. We notice that eq. 3.23 can be relaxed to

$$\omega_{\text{hf}} = n\omega_{\text{rep}} + \tilde{\omega}_A, \quad (3.24)$$

where $\tilde{\omega}_A$ is a total frequency offset given by either one or two AOMs. At a practical level, we used two AOMs $\tilde{\omega}_A = \omega_{A_1} + \omega_{A_2}$ with opposite direction frequency shifts. The Paladin 24W featured a repetition rate of 81.41 MHz, which means that we picked the 150th harmonic at 12.211 Ghz and AOM frequency of $2\pi \times 468.73$ MHz to drive the carrier

Chapter 4: Ultrafast spin-motional control

Here we describe the basic spin dependent interaction needed for our quantum phase gate. Although most of the theory has been laid by previous members of the Ultrafast lab [37, 38, 67], I will briefly describe the main concepts and key calculations. I finish with a discussion of the strong and weak coupling regimes where we work in resolve the motional sidebands regime compared to the impulsive limit.

4.1 Coherent state displacements and properties

The motional state of trapped ions in a trap is usually described in terms of Fock states since Doppler cooling leaves the ion in an incoherent mixture of number states with mean number \bar{n} . Although sideband cooling allows the preparation of true Fock states [68], a continuous variable description is better suited for calculating momentum kicks. Coherent states $|\alpha\rangle$ provide a better theoretical framework since they mirror the behavior of classical states and are best described in the phase space of x vs. p . They are superpositions of Fock states with a complex amplitude α

$$|\alpha\rangle = \exp(-|\alpha|^2/2) \sum_{n=0}^{\infty} \frac{\alpha^n}{\sqrt{n!}} |n\rangle \quad (4.1)$$

and eigenstates of the annihilation operator $a |\alpha\rangle = \alpha |\alpha\rangle$ following the identity

$$\langle \alpha | \beta \rangle = e^{-\frac{1}{2}(|\alpha|^2 + |\beta|^2 - 2\alpha^* \beta)}, \quad (4.2)$$

since they form an overcomplete basis. Moreover, time evolution is obtained by evolving its state by a phase

$$|\alpha(t)\rangle \Rightarrow |e^{-i\omega t}\alpha\rangle, \quad (4.3)$$

where ω is the Harmonic oscillator frequency. Sudden displacement of coherent state is described by the displacement operator $D[\beta]$ and its effect is

$$D[\beta]|\alpha\rangle = e^{(\beta\alpha^* - \beta^*\alpha)/2}|\alpha + \beta\rangle,$$

which adds an extra phase factor in front of the coherent state. For completeness, description of a thermal state in the coherent state basis is performed by the density matrix formalism

$$\rho = \int \left(\frac{1}{\pi \bar{n}} e^{-|\alpha|^2/\bar{n}} \right) |\alpha\rangle \langle \alpha| d^2\alpha, \quad (4.4)$$

where the integration is over the complex plane and the Gaussian factor accounts for the thermal distribution of fock states. If the ion is initialized in $|\downarrow, \alpha\rangle$ and we apply unitary operations \hat{U} , the measured brightness B is computed by tracing the motional part

$$B = \int \left(\frac{1}{\pi \bar{n}} e^{-|\alpha|^2/\bar{n}} \right) \langle \downarrow, \alpha | \hat{U}^\dagger | \uparrow \rangle \langle \uparrow | \hat{U} | \downarrow, \alpha \rangle d^2\alpha, \quad (4.5)$$

This equation is general for any \hat{U} and is the main result of this section due to its experimental importance. We can calculate any signal involving motional operations by measuring the spin states. Moreover, calculations can be simplified by taking a pure coherent state and then computing the thermal average at the very end.

4.2 Spin and motion coupling

Chapter 3 discussed the conditions for the coupling of the internal states of the ion with an electromagnetic pulse. This section is devoted to expanding these ideas to the coupling of light and the motional state of the ion.

First, we notice that the Rabi frequency (eq. 3.19) is maximized (See appendix E) when the fields acting on the atom have orthogonal polarization. Moreover, maximum momentum transfer is accomplished when two beams driving the Raman transition are counter propagating along the quantization axis. Taking into account such conditions, we start our analysis of spin-motion coupling by defining a quantization axis along \hat{z} (perpendicular to the direction of the ion chain), write any polarization as a superposition of three unit vectors

$$\hat{\epsilon} = (\sin \beta \cos \alpha) \hat{\sigma}^+ + (\sin \beta_j \sin \alpha) \hat{\sigma}^- + (\cos \beta) \hat{\pi}, \quad (4.6)$$

and defining the matrix elements in eq. 3.9 as

$$\langle g | \vec{\mu} \cdot \hat{\epsilon}_q | e \rangle = C_{g,e,q} B \quad (4.7)$$

Here, $q = +1, 0, -1$ corresponds to σ^+ , π , and σ^- , respectively, $C_{g,e,q}$ is a Clebsch-Gordon coefficient that is a function of the ground state, excited state, and without loss of generality, we have written B as a constant that is dependent on other atomic parameters. (the transition linewidth is proportional to the reduced matrix element so is the saturation parameter. [34]. The configuration of two laser beams linearly polarized but with orthogonal polarizations, usually called “lin perp lin” configuration implies $\beta = 0$, $\alpha_1 = \pi/4$ and $\alpha_2 = -\pi/4$, with these conditions, eq.

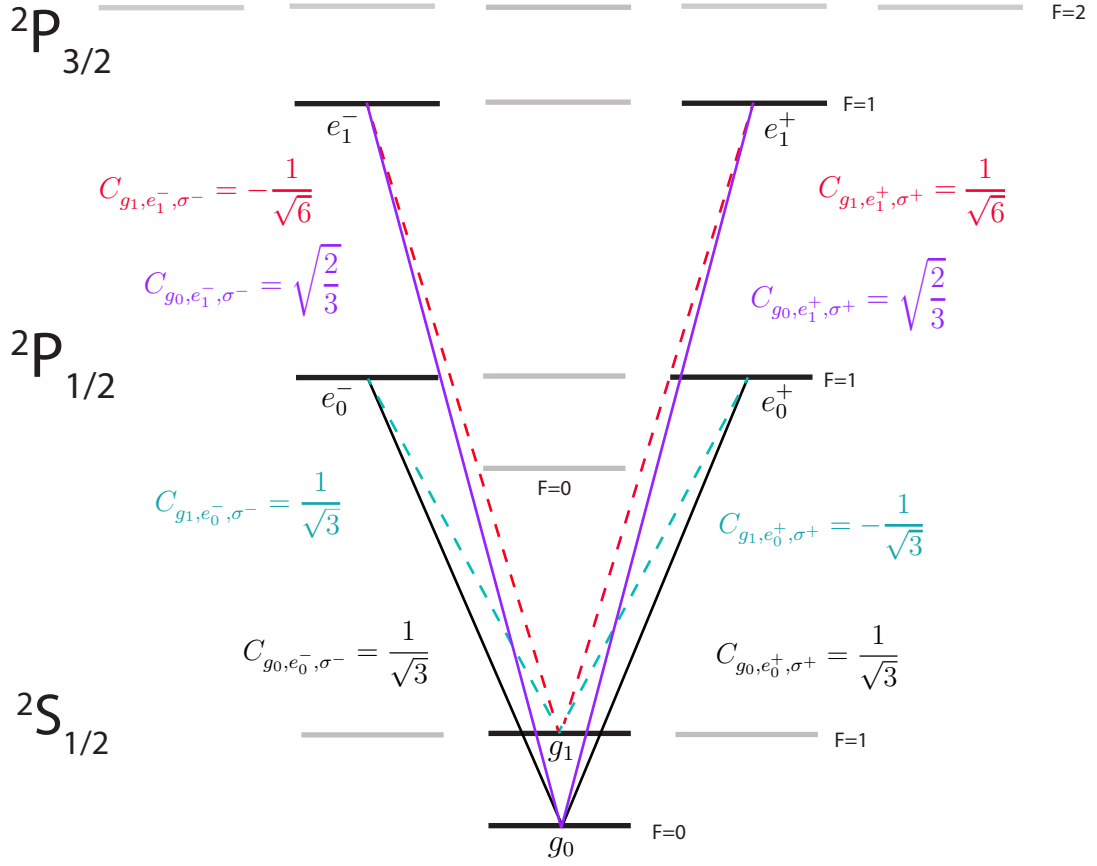


Figure 4.1: Clebsch-Gordan coefficients for the relevant Raman processes and energy levels.

3.9 takes the form:

$$\Omega_{g,e} = -\frac{B}{\sqrt{2}} ((C_{g,e,\sigma^+} + C_{g,e,\sigma^-}) \mathcal{E}_1(t) e^{-ikz+\phi_1} + (C_{g,e,\sigma^+} - C_{g,e,\sigma^-}) \mathcal{E}_2(t) t e^{ikz+\phi_2}) \quad (4.8)$$

To compute the Raman-Rabi frequency, we will use the same notation for the levels $^2P_{1/2}$ and $^2P_{3/2}$, and respective Clebsch-Gordan coefficients as in fig 4.1. Notice that the $|^2P_{3/2}, F = 2, m_F = \pm 1\rangle$ states do not participate in the Raman interaction since they do not connect the g_0 and g_1 states (a transition with g_0 is not dipole allowed).

Equation 3.9 with $\Delta_{e_0^+} \approx \Delta_{e_0^-}$ and $\Delta_{e_1^+} \approx \Delta_{e_1^-}$ is

$$\Omega_{g_1,g_0} = \frac{\Omega_{e_0^+,g_1}^* \Omega_{e_0^+,g_0}}{2\Delta_{e_0^+}} + \frac{\Omega_{e_1^+,g_1}^* \Omega_{e_1^+,g_0}}{2\Delta_{e_1^+}} + \frac{\Omega_{e_0^-,g_1}^* \Omega_{e_0^-,g_0}}{2\Delta_{e_0^-}} + \frac{\Omega_{e_1^-,g_1}^* \Omega_{e_1^-,g_0}}{2\Delta_{e_1^-}} \quad (4.9)$$

we compute the first term

$$\begin{aligned} \Omega_{e_0^+,g_1}^* \Omega_{e_0^+,g_0} &= \left(\frac{B^2}{2} \right) \left(-\frac{1}{\sqrt{3}} \right) (\mathcal{E}_1(t)e^{-ikz+\phi_1} + \mathcal{E}_2(t)te^{ikz+\phi_2})^* \times \\ &\quad \left(\frac{1}{\sqrt{3}} \right) (\mathcal{E}_1(t)e^{-ikz+\phi_1} + \mathcal{E}_2(t)te^{ikz+\phi_2}) \\ &= \left(-\frac{B^2}{6} \right) |\mathcal{E}_1(t)e^{-i(kz+\phi_1)} + \mathcal{E}_2(t)e^{i(kz+\phi_2)}|^2 \\ &= -\left(\frac{B^2}{6} \right) (\mathcal{E}_1(t)^2 + \mathcal{E}_2(t)^2 + 2\mathcal{E}_1(t)\mathcal{E}_2(t)\cos(2kz + \Delta\phi)), \end{aligned}$$

where we have defined the difference frequency between the phase shifts:

$$\Delta\phi = \phi_1 - \phi_2$$

Similar conditions apply to the other terms, leading to the final simplified result

$$\Omega_{g_1,g_0} = 2K\mathcal{E}_1(t)\mathcal{E}_2(t)\cos(2kz + \Delta\phi), \quad (4.10)$$

where K is a constant related to the saturation intensities, detuning from the P states, Δ_{e_0} and Δ_{e_1} and natural transition linewidths. This result is consistent with eq. 4. 113 in [37] when writing the equivalence $K\mathcal{E}_1(t)\mathcal{E}_2(t) \equiv \sqrt{\Omega_1(t)\Omega_2(t)}$.

4.3 Evolution operator for a single ultrafast pulse

Inserting eq. (4.10) in eq. (3.20) of the full effective Hamiltonian, leads to

$$\frac{H_{\text{effective}}}{\hbar} = -\sqrt{\Omega_1(t)\Omega_2(t)} \cos(2kz + \Delta\phi) \hat{\sigma}_x - \frac{\omega_{\text{hf}}}{2} \hat{\sigma}_z. \quad (4.11)$$

We approximate the Rabi frequencies Ω by delta functions weighted by the pulse area $\Omega(t)_{1,2} \rightarrow \theta\delta(t)_{1,2}$ and the evolution operator can be obtained by simple integration since the Hamiltonian commutes with itself at later times:

$$\begin{aligned} U &= \exp\left(-\frac{i}{\hbar}\int H_{\text{effective}}(t)dt\right) \\ &= \sum_{n=-\infty}^{\infty} i^n J_n(\theta\hat{\sigma}_x) e^{in(\eta[a^\dagger+a]+\Delta\phi)} \end{aligned} \quad (4.12)$$

where $\eta = \Delta k \sqrt{\frac{\hbar}{2m\omega}}$ is the Lamb-Dicke parameter defined for an ion of mass m , oscillator frequency ω and subject to light. The Bessel functions J_n were obtained by the Jacobi-Anger expansion during the derivation of eq. (4.12). We can write the evolution operator in a more familiar form

$$U = \sum_{n=-\infty}^{\infty} i^n J_n(\theta) e^{in\Delta\phi} \mathcal{D}[in\eta] \hat{\sigma}_x^n. \quad (4.13)$$

The equation above follows a simple physical explanation: The ion will absorb and emit one photon from one of the counter propagating beams, leading to change in momentum of $2\hbar k$. Since that process happens n times, the motional wavefunction of the ion is diffracted in momentum orders as integer multiples of the Lamb-Dicke parameter. The probability amplitudes on each of these orders is modulated by the Bessel function and is dependent on the pulse area θ . Figure 4.2 shows an example of how the momentum orders are populated as the pulse area increases. This phenomenon is similar to the diffraction of BECs by standing waves, where the number of diffraction orders is dependent on how strong is the light modulated at the BEC position (pulse area), leading a Raman-Nath scattering [69].

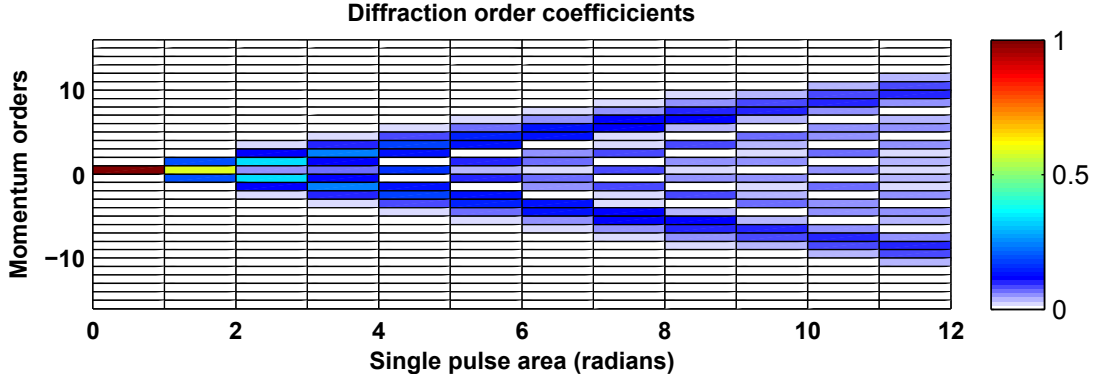


Figure 4.2: Single pulse motional wavepacket diffraction. We start at the zeroth order momentum order (see arrow). As the pulse area increases, the motional wavefunction diffracts into higher momentum orders.

4.3.1 Spin dependent kick

The full effect of a single pulse lin perp lin pair is described by eq. 4.13 but it is not what we need for a true spin dependent displacement since each diffraction event is accompanied by other orders with alternating spin states, which is a consequence of the symmetry of the system. We instead need an operator that will displace the motional state depending on the initial displacement. This can only be accomplished by concatenating several pulses timed in such a way that instead of diffracting to different orders, they coherently interfere to a single momentum state. In our experiment (see fig. 4.3), we chose to split one laser pulse into eight sub-pulses using a system comprised of three delay stages. The delay values were numerically optimized to transfer all the motional population to the first diffraction order. The final theoretical fidelity is 99.7 % only limited by the pulse spectrum. We set the stages at 16, 8 and 6.5 periods of the hyperfine evolution and ω_A . With a total interaction time of ≈ 2.5 ns, we produce a unitary evolution best described by

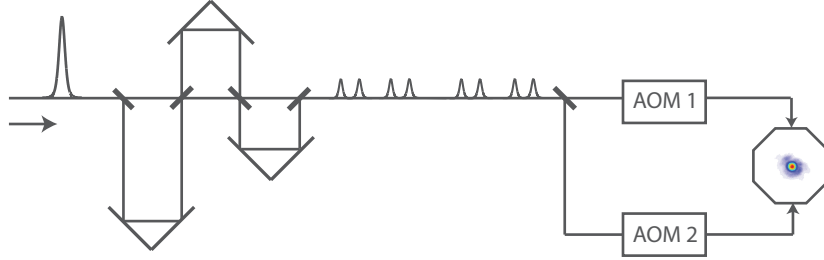


Figure 4.3: Experimental schematic. A single pulse from a mode-locked 355 nm laser is divided into 8 sub-pulses by three sequential optical delay stages. The shaped pulse is then split into two paths directed through independent AOMs, used to make the interaction direction-dependent. The pulses overlap in space and time at the position of the ions in a counterpropagating lin \perp lin polarization configuration that produces an spin dependent kick (SDK) [67].

$$U_{\text{SDK}} = e^{i\phi(t)} \hat{\mathcal{D}}(i\eta) \hat{\sigma}_+ + e^{-i\phi(t)} \hat{\mathcal{D}}(-i\eta) \hat{\sigma}_-, \quad (4.14)$$

where the phase $\phi(t) = \omega_A t + \phi_L$ is related to the AOM frequency and the absolute optical phase ϕ_L of the driving laser, assumed to be common mode for the two beam paths and constant during the interaction. The raising and lowering operators $\hat{\sigma}_{\pm}$ act on the qubit, and the displacement operator $\hat{\mathcal{D}}(\pm i\eta)$ acts on the motional state of the ion along the axis of transverse motion, translating the momentum in phase space by $\Delta p = \pm \hbar(\Delta k) = \pm 2p_0\eta$. Here $\Delta k = 2k$ is the wavevector difference between the counter-propagating beams and $p_0 = \sqrt{m\hbar\omega/2}$ is the zero-point momentum spread of harmonic motion at frequency ω for an ion of mass m ($x_0 = \hbar/2p_0$ is the zero-point position spread). The Lamb-Dicke parameter $\eta = \hbar\Delta k/(2p_0) \approx 0.17$ thus parametrizes the momentum kick in natural units. In contrast to conventional forces applied in the resolved sideband regime [24], the impulsive SDK is about three hundred times faster than the oscillation period and does not rely on confinement

to the Lamb-Dicke regime.

4.3.2 From weak to strong coupling

We experimentally demonstrate (fig. 4.4) that, as a longer and weaker train of pulses is sent to the ion, the normal mode picture is recovered using the same setup. This can be seen from eq. 4.11 by taking the Lamb-Dicke approximation $\eta\sqrt{2n+1} \ll 1$ and working in the interaction picture of the free spin and trap evolution we obtain

$$U_{\text{weak}}(t) = 1 + \frac{\sqrt{\Omega_1(t)\Omega_2(t)}}{2} (e^{i\Delta\phi}[1 + i\eta(e^{i\omega_{\text{trap}}}a^\dagger + e^{-i\omega_{\text{trap}}}a)] \times \quad (4.15)$$

$$[e^{i(\omega_{hf}+\omega_A)t}\hat{\sigma}_+ + e^{i(\omega_{hf}-\omega_A)t}\hat{\sigma}_-] + \text{H.c.}) \quad (4.16)$$

where a (a^\dagger) are the lowering (raising) operators and ω_{trap} is the trap frequency. Concatenating such operations and matching conditions like $(\omega_{hf} + \omega_A + \omega_{\text{trap}})/2\pi \in \mathbb{Z}$ we converge to

$$U_{\text{weak train}} = \cos \frac{\Theta\eta}{2} + i \sin \frac{\Theta\eta}{2} (ie^{i\Delta\phi}a^\dagger\hat{\sigma}_-ie^{-i\Delta\phi}a\hat{\sigma}_-). \quad (4.17)$$

The above expression drives the blue sidebands where a spin flip also adds or subtract a phonon. As we sweep the ω_A around the carrier with condition $(\omega_{hf} + \omega_A)/2\pi \in \mathbb{Z}$ we resolve each motional mode (see fig. 4.11a). We realize that when we are deep in the Lamb-Dicke regime, no second order sidebands are resolved.

In the ultrafast regime, each pulse is strong enough to affect all the motional modes and justifies the concept of “impulsive limit”. A consequence of such interaction is that spurious modes and transitions are also driven such as drive to the

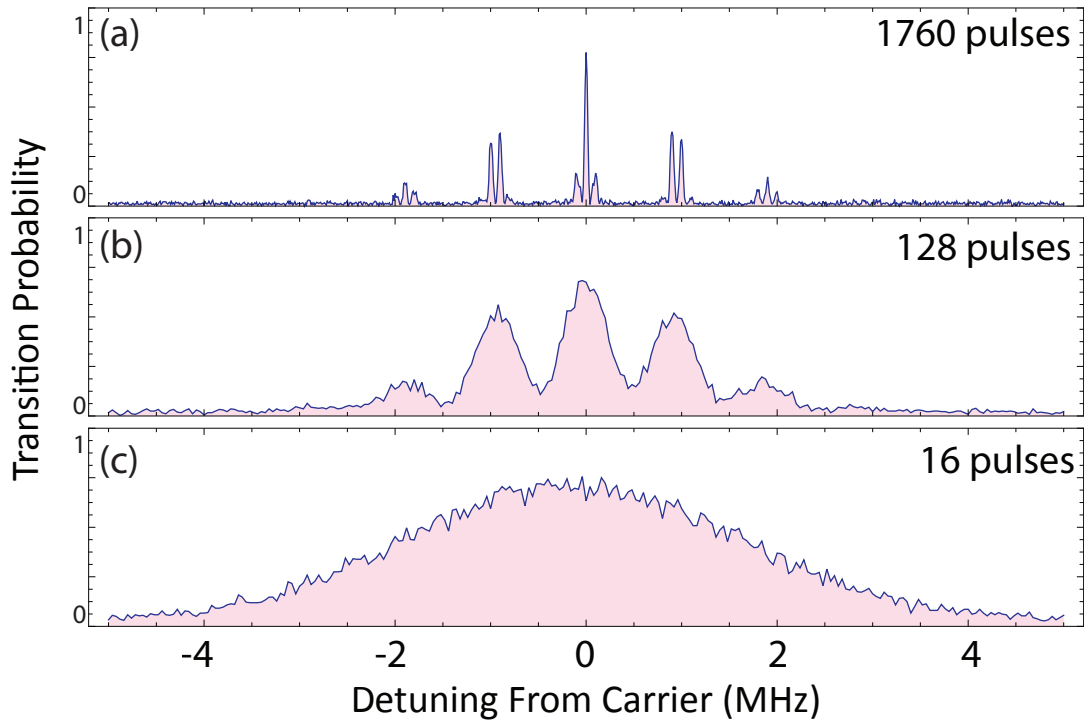


Figure 4.4: Crossover between the resolved motional sidebands and the impulsive limit. For a weak train of pulses, the spectrum is given by a comb. The locked frequency difference between the two Raman beams drive transitions at the trap frequency harmonics. In the impulsive limit, no beat note lock is necessary since the bandwidth of each pulse covers the whole spectrum.

Zeeman states and coupling to the axial modes. Careful experimental analysis is required to ameliorate such effects.

Chapter 5: SDK characterization, and validation.

I developed in chapter 4 the theory for ultrafast SDK and showed a few conceptual experiments. This chapter is devoted to discuss the experimental issues in the proper coherent transfer from one momentum order to another. The first part is the experimental checklist that characterizes the efficiency of the SDK. Magnetic fields, laser power fluctuations, coupling to the wrong motional modes and proper quantization axis alignment are added to the theoretical model 4.12 to study their influence and see how they affect the performance.

We then apply the SDKs for a particular application that validates the features of our base operator. We perform thermometry by spatially separating the motional wavefunction and performing an autocorrelation using the light that we collect. We find that our interaction is capable of measuring temperatures from the ground state to Kelvin temperatures. Although similar techniques have been used in tapered nanofiber systems [70], such large dynamic range is possible, in our system, because we can operate far outside the Lamb-Dicke regime, only limited by laser focusing.

Following the demonstration of large dynamic range thermometry, we prepare large mesoscopic states and non trivial motional states. By applying momentum kicks at the ion in either a synchronized or consecutive way, we create the largest

mesoscopic superposition of an atom in a harmonic trap. Furthermore, we also demonstrated the creation of multicomponent “cat” states. The experimental results we present here are based on references [71, 72].

5.1 Experimental considerations

We analyze next the effect of coupling to the wrong motional mode, Hilbert space leakage to the Zeeman states and spin independent kicks. Each issue potentially contribute to the fidelity decrease of a perfect SDK.

5.1.1 Drive to the Zeeman levels

When the Raman beams are perfectly aligned in the lin \perp lin configuration, only the $|0\rangle \leftrightarrow |1\rangle$ can be driven. However, if there is a component of π light due to misalignment, spurious transitions such as the $|0\rangle \leftrightarrow |1\rangle_{\text{Zeeman}}$ are driven instead, where $|1\rangle_{\text{Zeeman}}$ represents the $|F = 1, m_f = \pm 1\rangle$ states. Population of these states represent a leakage of the Hilbert space of the qubits and degrades the SDK fidelity.

There are two ways this transition can occur: If the magnetic field is not properly oriented with respect to the polarization of the Raman lasers or if we focus the beam too tightly, thereby getting an axial polarization component [59, 73]. Since the axial polarization is an unavoidable feature of any tightly focused Gaussian beam, it is important to understand how small we can make the beam before this becomes an issue.

We estimate the axial polarization component by considering the Gauss’ law

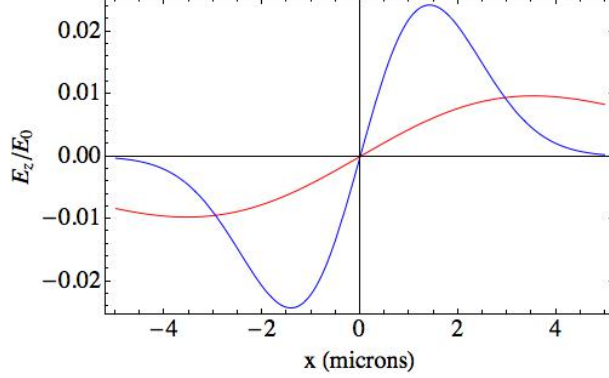


Figure 5.1: Component of electric field along the axial direction vs. distance from the center of the beam for a 2 (blue) and 5 (red) μm waist.

in free space equation, $\vec{\nabla} \cdot \vec{E} = 0$, which for a Gaussian beam polarized along the transverse \hat{x} direction simplifies to [59]:

$$E_z = - \int \frac{\partial E_x}{\partial x} dz \quad (5.1)$$

and relative to E_0 , the field strength at the center of the beam, the z component is

$$\frac{E_z(x, y, 0)}{E_0} = \frac{2xe^{-x^2/w^2}}{k\omega_0^2}, \quad (5.2)$$

where k is the wavevector and ω_0 is the beam waist.

Figure 5.1 shows two examples for beams with 2 and 5 μm waist. A reasonable consideration is that the ion will be within 0.5 μm of the center of the beam. In that case, E_z/E_0 should be less than 1%, even for a 2 μm beam. In the resolved sideband limit (weak regime), all the Zeeman transitions are far detuned from the main carrier operations and the effect of axial polarizations are well suppressed due to spectral selectivity. Unfortunately, in the ultrafast regime, we spectrally address all transitions over a much larger bandwidth and the only way of suppressing the

Zeeman state population is through a better light polarization control.

We take two approaches for ameliorating this issue: scanning the shim coils for proper quantization axis setting , and use of larger beams where the axial component of the polarization is small. The main difficulty with the former is that the Zeeman states contribute to the brightness (eq.) since they are detected as if they were in the $|1\rangle$ state but they do not contribute to the motional states of interest, thus making the troubleshooting difficult.

5.1.2 Model

We obtain an approximation of this effect by considering transitions to the clock states, with Rabi frequency Ω and pulse area θ and transitions to the Zeeman states with Rabi frequency and pulse area Ω' and θ' , respectively. Ideally $\Omega' \ll \Omega$ and $\theta' \ll \theta$. For simplicity we consider coupling to only one of the Zeeman transitions since generalization to multiple levels is straightforward.

The Zeeman coupling modifies eq. 4.11 to include an additional term:

$$H_{\text{eff}}(t) = -\theta\delta(t - t_0)\cos(\Delta k\hat{x} + \Delta\phi(t))\hat{\sigma}_x^C - \theta'\delta(t - t_0)\cos(\Delta k\hat{x} + \Delta\phi(t))\hat{\sigma}_x^Z \quad (5.3)$$

where the superscript on the $\hat{\sigma}_x$ operators denotes which manifold (C = clock and Z = Zeeman) that operator acts on. Now calculating $U_p(t_0)$, we get the product of two infinite sums:

$$U_p(t_0) = \sum_n i^n J_n(\theta)(\hat{\sigma}_x^C)^n e^{in(\eta(\hat{a} + \hat{a}^\dagger) + \Delta\phi(t_0))} \otimes \quad (5.4)$$

$$\sum_m i^m J_m(\theta')(\hat{\sigma}_x^Z)^m e^{im(\eta(\hat{a} + \hat{a}^\dagger) + \Delta\phi(t_0))}. \quad (5.5)$$

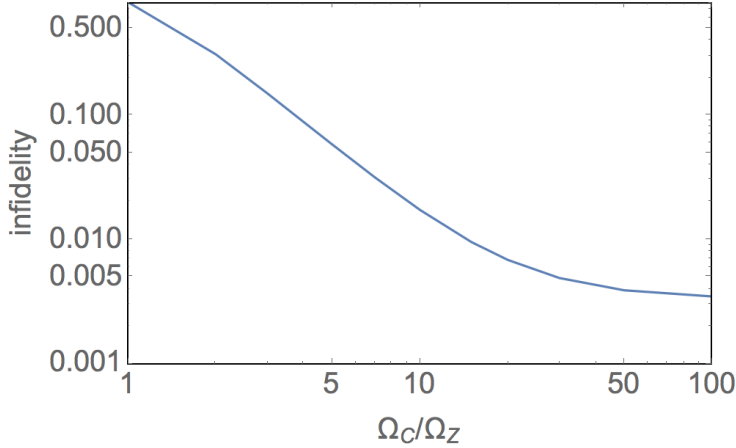


Figure 5.2: Infidelity vs. the ratio of the Rabi frequencies of the qubit and Zeeman transitions.

We find that when $\theta' \ll \theta$ only the carrier term on the Zeeman level is populated and its momentum orders do not participate in the interaction to first order.

The SDK infidelity as a function of Ω/Ω' is shown in Fig. 5.2 for our delay settings. Here, the infidelity is 0.002-0.003, even if there is no Zeeman coupling. We realize that as long as the ratio Ω_C/Ω_Z is larger than 20 or 30, the infidelity can be considered negligible. However, this still places a stringent requirement on the polarization, since the Rabi frequencies scale as $\mathcal{E}_1(t)\mathcal{E}_2(t)$, and to obtain a ratio of 20-30 means the polarization should be pure to a part in 500~1000.

5.1.3 Polarization imperfection

Polarization imperfection on the two counterpropagating Raman arms drive motionless transitions and arise from circular polarization contributions from single arms or from polarization leakage of a defective optic, i.e. a polarizing beam splitter.

Better polarization control is achieved by a high extinction ratio polarizer such as a Glan Thomson or by placing $\lambda/2$ and $\lambda/4$ plates before the beam enters the vacuum chamber. Modelling of this effect is similar to the Zeeman case (eq. 5.4) except that there is no motional dependence

$$U_p(t_0) = \sum_n i^n J_n(\theta)(\hat{\sigma}_x)^n e^{in(\eta(\hat{a}+\hat{a}^\dagger)+\Delta\phi(t_0))} \sum_m i^m J_m(\theta')(\hat{\sigma}_x)^m e^{im\Delta\phi(t_0)}. \quad (5.6)$$

5.1.4 Axial mode coupling

Misalignment of the Raman beams respect the quantization axis can drive axial modes since the selection rule for Δk is met. The Hamiltonian in this case becomes

$$H_{\text{eff}}(t) = -\theta\delta(t-t_0)\cos(\Delta k_x \hat{x} + \Delta k_z \hat{z} + \Delta\phi(t))\hat{\sigma}_x, \quad (5.7)$$

with evolution operator

$$U_p(t_0) = \sum_n i^n J_n(\theta)(\hat{\sigma}_x)^n e^{in(\eta(\hat{a}+\hat{a}^\dagger)+\eta'(\hat{b}+\hat{b}^\dagger)+\Delta\phi(t_0))}, \quad (5.8)$$

where η is for the normal transverse coupling and η' is for the axial coupling (with $\eta' \approx \eta \sin \alpha$, where α is the angle of the beams respect the transverse direction), and \hat{b} (\hat{b}^\dagger) are the annihilation (creation) operators for phonons in the axial direction. For our normal operating conditions, $\omega_r/2\pi \approx 1.3$ MHz and $\omega_z/2\pi \approx 480$ kHz. With two ions, this becomes the center of mass axial mode, and the frequency of the relative axial mode is $\sqrt{3}$ times higher, so around 830 kHz. Indeed the coupling to the relative axial mode may be more detrimental.

We will have coupling to the axial mode if the Δk vector has some projection onto the axial direction, so the ratio of Rabi frequencies, $\Omega_{\text{axial}}/\Omega_{\text{trans}}$ should be low.

We can mitigate it by aligning the beams to be counterpropagating perpendicular to the axis of the trap. The Lamb-Dicke parameter is different for the axial mode, meaning that the size of the kicks is different.

5.1.5 Leakthrough light

Imperfect polarization control due to the first Pockels cell allows a small train of pulses go through the table. The time length of this train depends on how long we turn on the chopping AOM. Wrong switching let pass a small fraction of the neighbour pulses and the train that was not properly blocked due to a finite extinction ratio of the modulator. The small pulses are an inherent problem in the speed of the polarization switching and its effect is hard to cancel. The effects of the long leakthrough light can be cancelled by detuning one of the AOMs to not let this light hit any sideband.

5.2 Experiments with SDKs

We next describe two experiments used to benchmark our basic building blocks. The first one aims to demonstrate that the performance of the SDKs is immune to the motional state of the ion and works outside the Lamb-Dicke regime. We use ultrafast techniques for accurate thermometry of ion motion ranging from $\bar{n} \sim 0.1$ to $\bar{n} \sim 10^4$ and show how this method extends to higher energies. We also measure particular quantum states through more complete motional tomography.

The second experiment involves the creation of mesoscopic quantum super-

positions or ‘‘Cat’’ states. Such large superpositions are required for the ultrafast gate (See chapter 6 for a general discussion) and studying them is a requirement for our understanding of highly spatially separated coherent states in our trap. We achieve a maximum separation of $\Delta\alpha \approx 24$ or 259 nm in real space, compared to the $x_0 = 5.4$ nm of the ground state motional state. Moreover, we demonstrate excellent coherent control by creating multicomponent superposition states, never created in massive systems before.

5.2.1 Thermometry with ultrafast pulses

We create an interferometer to sense motion by applying two sets of N SDK operations within a Ramsey experiment on the qubit levels with time duration T (time separation of microwave $\pi/2$ pulses). First the ion is prepared in a coherent superposition of $|0\rangle$ and $|1\rangle$ by applying a near-resonant microwave $\pi/2$ pulse of duration τ_μ . A set of N SDKs is applied, and following this first set, the ion evolves for a time Θ/ω before a second set of N SDKs is applied. After a time T from the first microwave $\pi/2$ pulse, another microwave $\pi/2$ pulse with the same duration and tuning drives the qubit to close the Ramsey interferometer. This sequence is diagrammed in Fig. 5.3(a). By scanning the microwave detuning $\delta \ll 1/\tau_\mu$ from resonance, we observe sets of Ramsey fringes with phase $\phi = \delta T$ that chronicle the ion motion (shown in Fig. 5.3(b) and 5.3(c)).

Starting from a pure initial state $|\Psi^\alpha\rangle_i = |0\rangle|\alpha\rangle$, where α is a coherent state

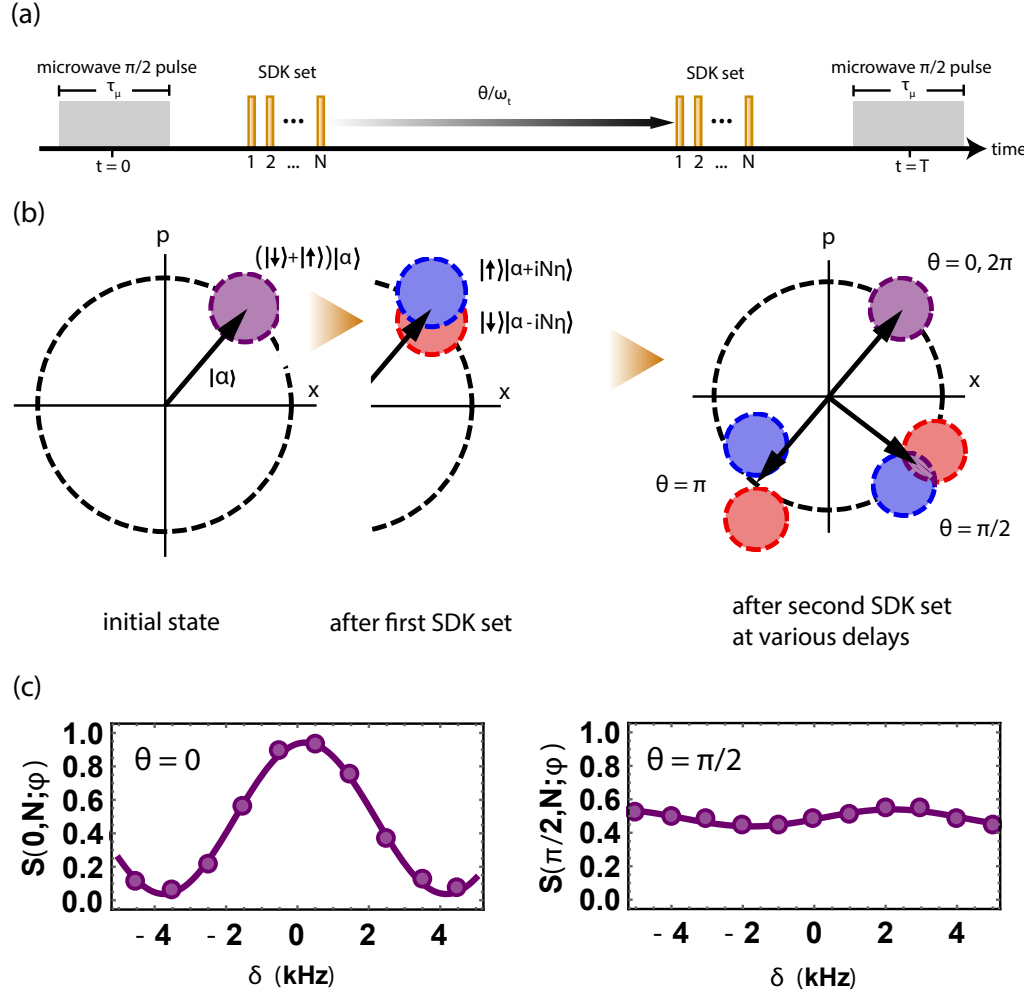


Figure 5.3: Ultrafast atom interferometry [71]. (a) Timeline of a single experiment, where a full SDK set is made of N single SDKs. (b) Phase space diagram of an initial state $(|0\rangle + |1\rangle)|\alpha\rangle$ evolving under two sets of SDKs separated by time delay Θ/ω_t , where $|\alpha\rangle$ is a coherent state of motion. (c) Typical Ramsey fringes as a function of microwave frequency detuning δ . These two plots correspond to the points $\Theta = 0$ and $\Theta = \pi/2$ of an initial thermal state ($N = 1$ for the data shown). The function $S(\Theta, N; \phi)$ is described by Eq. 5.10.

of the ion motion, the state following a Ramsey experiment is [37]

$$\begin{aligned} |\Psi^\alpha\rangle = \frac{1}{2} & \left[e^{i\gamma} \left(|0\rangle + ie^{-i\phi} |1\rangle \right) |(\alpha + iN\eta)e^{-i\Theta} - iN\eta\rangle \right. \\ & \left. + ie^{-i\gamma} \left(|1\rangle + ie^{i\phi} |0\rangle \right) |(\alpha - iN\eta)e^{-i\Theta} + iN\eta\rangle \right], \end{aligned} \quad (5.9)$$

where $\gamma = N\eta[\text{Re}(\alpha)(1 - \cos\Theta) - \text{Im}(\alpha)\sin\Theta]$.

Given an arbitrary initial state of motion in phase space described by the Glauber P-distribution [74, 75], the final density matrix is $\hat{\rho} = \int P(\alpha) |\Psi^\alpha\rangle \langle \Psi^\alpha| d^2\alpha$. The probability of measuring the state spin-up after the Ramsey experiment is therefore

$$S(\Theta, N; \phi) = \langle 1 | \hat{\rho} | 1 \rangle = \frac{1}{2} + \frac{1}{2} \int P(\alpha) e^{-4(N\eta)^2(1-\cos\Theta)} \cos(4\gamma - \phi) d^2\alpha. \quad (5.10)$$

Two types of motional state that are readily accessible in the laboratory are thermal states and small Fock states. First we discuss ultrafast partial state tomography to determine the average phonon number in a thermal state. Then we extend this method to create a nearly complete map of the motion of an $n = 1$ Fock state in phase space, showing clear nonclassical signatures.

5.2.2 Sensing of a thermal state

An ion prepared in a thermal state with mean phonon number \bar{n} and P-function $P_{therm}(\alpha) = \frac{1}{\pi\bar{n}} e^{-|\alpha|^2/\bar{n}}$, eq. 5.10 yields an expected Ramsey fringe pattern

$$S_{therm}(\Theta, N; \phi) = \frac{1}{2} + \frac{1}{2} e^{-4(N\eta)^2(2\bar{n}+1)(1-\cos\Theta)} \cos\phi. \quad (5.11)$$

The fringe contrast has periodic peaks at $\Theta = 2\pi m$, where m is a positive integer. For a hot ion where $\bar{n} \gg 1/(N\eta)^2$, these revivals in contrast become narrow and

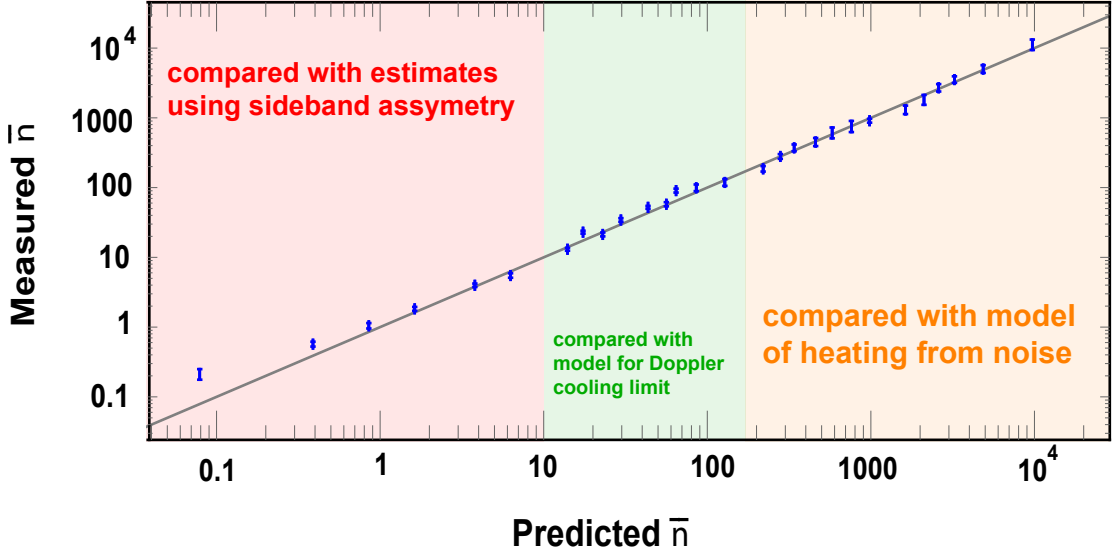


Figure 5.4: Ultrafast sensing measurements of \bar{n} (with $N = 1$) [71]: Measurements of \bar{n} versus predicted values. There are three regimes of thermal state preparation—red being sideband-cooling then heating (see fig. 5.5), green being Doppler cooling with different detunings (see fig. 5.6) and orange being heating with applied noise (see fig. 5.7)

approximately Gaussian with full width at half maximum FWHM= $0.83/(N\eta\sqrt{\bar{n}})$.

With $N = 1$, we measure the Ramsey fringe contrast as a function of Θ for a variety of initial thermal states of motion, and fit the contrast revival peaks to eq. 5.11 to determine the average phonon number \bar{n} of the thermal stat [76–78]. In the fit, we allow the peak Ramsey contrast at $\Theta = 2\pi m$ to be less than unity in order to parametrize imperfect fidelity of the SDK operations. This reduction in fidelity is mainly attributed to variations in the Raman beam intensity over the spatial extent of the ion wave packet (beam waist is $\approx 2 \mu\text{m}$), and becomes apparent at high \bar{n} ($\bar{n} = 10000$ has a spread of $\approx 1 \mu\text{m}$). This does not affect the width (it does affect the height) of the contrast revival peak, and thus the accuracy of the thermometer, and can be mended by widening the beam waist. Ramsey contrast revival lineshapes

are measured in experiments spanning over five orders of magnitude in \bar{n} . Figure 5.4 shows these measurements plotted versus the expected value of \bar{n} from theory and other measurements. The figure is broken into three regions according to the manner in which the motional state is prepared and calibrated before measurement of the contrast revival lineshapes. Low energy thermal states ($\bar{n} < 10$) are generated by first sideband-cooling the ion to its zero point motion and then allowing the ion to weakly heat (the trap has a natural heating rate of 310(10) quanta/s due to trap electrode noise and anomalous heating [79]) in the trap by known amounts. In this regime, we compare ultrafast interferometric measurements of \bar{n} (shown in Fig. 5.5a) to values extracted from measured sideband asymmetries [23]. The deviation of the two measurements are shown in the red section of Fig. 5.4.

Thermal states of $10 < \bar{n} < 150$ are prepared by Doppler cooling with various frequency detunings from resonance. Ultrafast measurements in this regime are shown in Fig. 5.6a. Each of these measurements and the predicted value of \bar{n} from Doppler cooling theory [80] (Fig. 5.6b) are plotted against each other in the green section of Fig. 5.4. As a check on the expected values of \bar{n} in this range, we also measure the Debye-Waller suppression of Rabi flopping amplitude transitions between the ion qubit states [23] for several cases, resulting in expected values consistent with Doppler theory.

Hot thermal states are prepared by inducing a high heating rate with a noisy electrical potential to a trap electrode for varied amounts of time after Doppler cooling. The ultrafast measurements of these states are shown in Fig. 5.7a. Measurements in this regime are compared to a predicted \bar{n} given by the equation

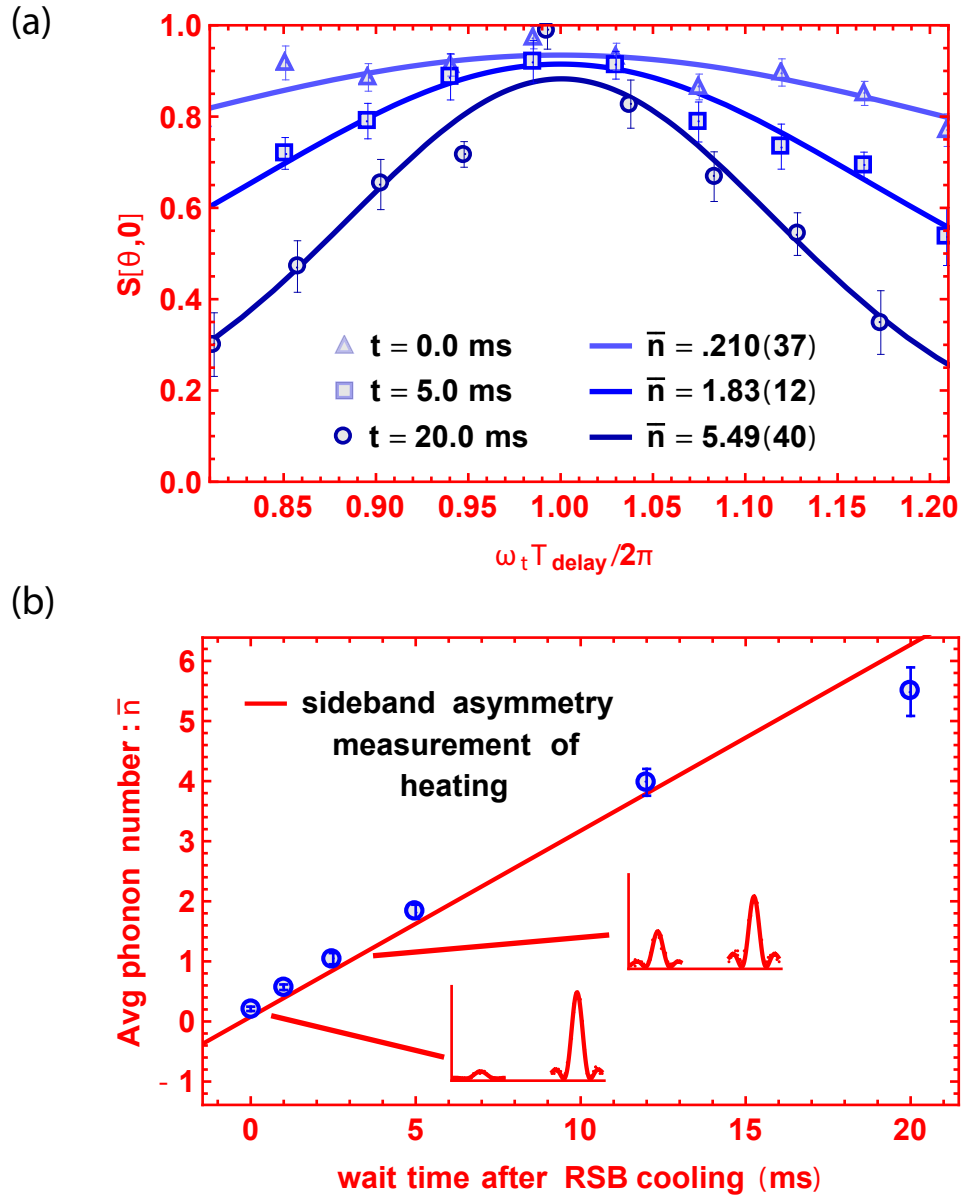


Figure 5.5: Ultrafast thermometry in the sideband cooling regime. (a) Sampling of Ramsey revival contrast lineshapes with initial states prepared by resolved sideband cooling to the ground state and subsequent heating. Data is fit to $S_{\text{therm}}(\Theta, 1; \phi)$. The amplitude of each fit is a free parameter to account for SDK infidelity (also done in fig. 5.6 and 5.7). This does not significantly affect the width of the peak, which is used to determine \bar{n} . (b) Using identical state preparation to (a) but then a conventional sideband asymmetry measurement to determine ion temperature, a heating rate is determined and used to model the phonon number for wait times (solid line). The thermometry measurements from (a) are plotted to compare.

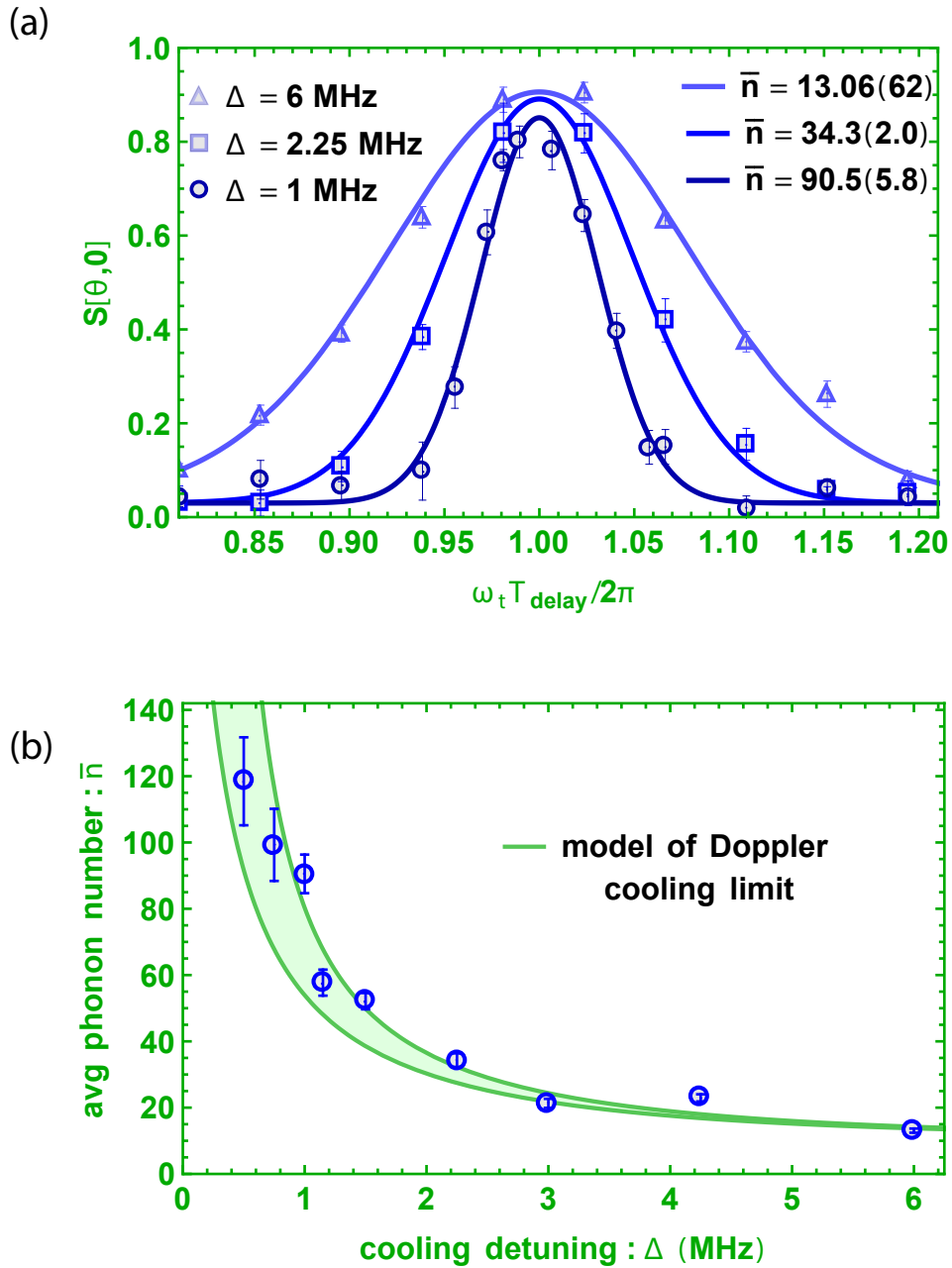


Figure 5.6: Ultrafast thermometry in the Doppler cooling regime. (a) Sampling of Ramsey revival contrast lineshapes with initial states prepared by Doppler cooling only, with \bar{n} varied by changing the cooling beam detuning. (b) A model for average phonon occupation when preparing each state with various Doppler cooling beam detunings—the Doppler limit is a function of detuning (solid lines). Data from (a) is compared to the model.

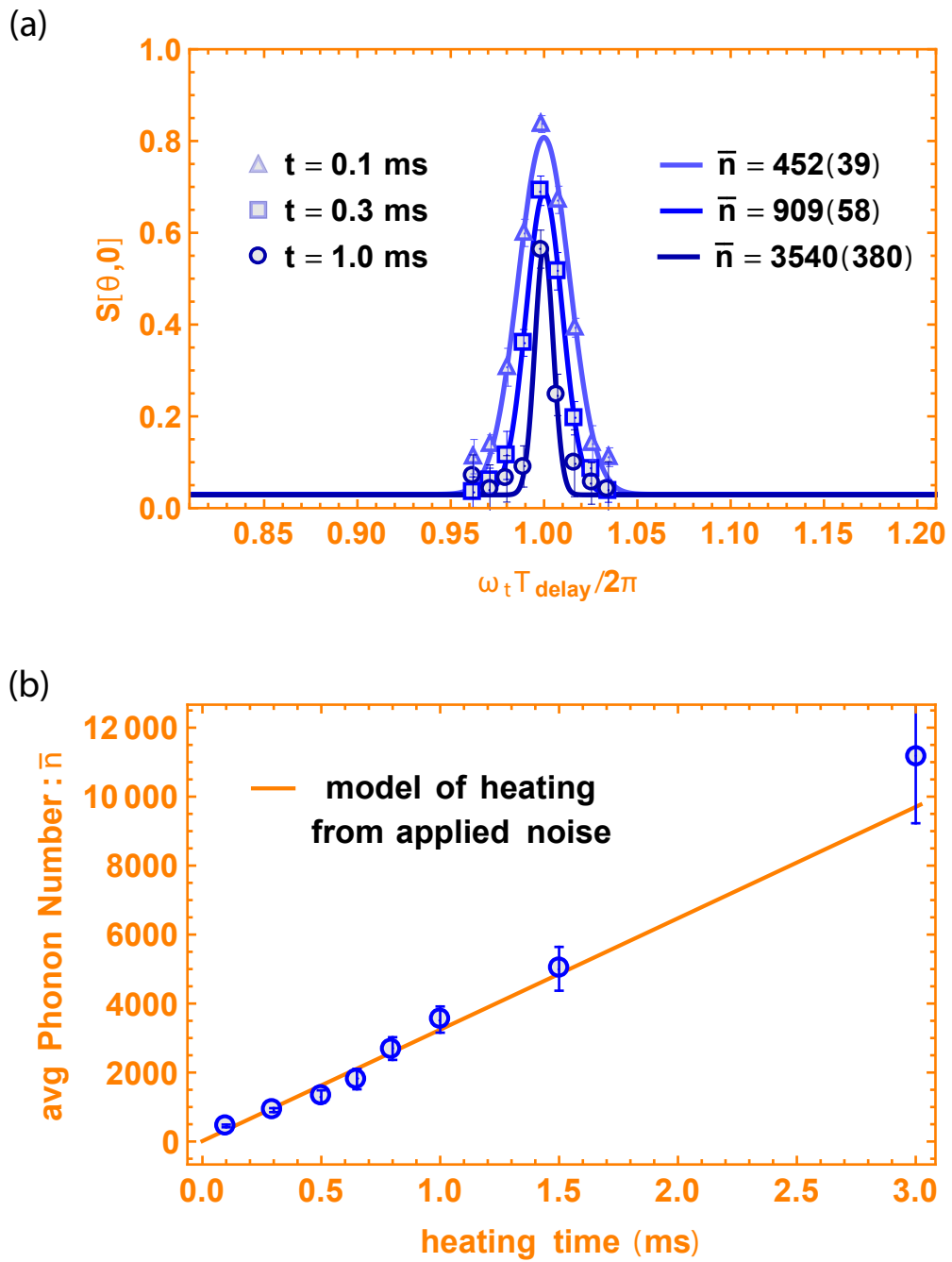


Figure 5.7: Ultrafast thermometry in the high \bar{n} regime. (a) Sampling of Ramsey revival contrast lineshapes with initial states prepared by inducing a high heating rate with white noise applied to a trap electrode. (b) A model for the phonon occupation after applying electrode noise is shown (solid line). Data from fits like that of (a) are plotted for comparison.

$\dot{n} = \frac{e^2 S_V(\omega)}{4M\hbar\omega d^2}$ [81], where e is the ion charge, and $S_V(\omega)$ (V^2/Hz) is the applied power noise spectral density of the electric-potential, which is white over the measurement bandwidth (Fig. 5.7a). The effective distance d of the electrode to the ion is calibrated by applying a static potential offset to the same electrode and observing the resulting displacement of the ion in space [48]. The predicted and measured values for this regime are plotted against each other in the orange region of Fig. 5.4.

5.2.3 Fock State Tomography

We next perform more complete tomography of a nearly pure quantum state of motion by extracting the characteristic function

$$\chi_W(\alpha) = e^{-|\alpha|^2/2} \int P(\beta) e^{2i\text{Im}(\alpha\beta^*)} d^2\beta, \quad (5.12)$$

where $P(\beta)$ is again the Glauber P-distribution (integrated over the complex plane). This quasiprobability distribution contains all the information about the quantum state and is the Fourier transform of the better-known Wigner distribution [82, 83].

We measure $\chi_W(\alpha)$ in terms of the observable $S(\Theta, N; \phi)$ using the equations

$$\text{Re}[\chi_W(\alpha)] = 2S(\Theta, N; 0) - 1, \quad (5.13)$$

$$\text{Im}[\chi_W(\alpha)] = 2S(\Theta, N; \frac{\pi}{2}) - 1, \quad (5.14)$$

where $\alpha = 2N\eta[\sin \Theta + i(1 - \cos \Theta)]$. Scanning Θ and N while measuring $S(\Theta, N; \phi)$ maps the characteristic function over rings in phase space, shown in Fig. 5.8(a). In order to scan the negative imaginary part of α , we can change the direction of the initial momentum kick associated with the spin flip operators by shifting the relative

optical phase of the counter-propagating beams by π [33]. These reversed kicks can be thought of as effectively flipping the sign of η , and for simplicity, we represent them here by negative values of N .

We measure the characteristic function $\chi_W(\alpha)$ of the ion in the $n=1$ Fock state, prepared by sideband cooling to the ground state and transferring population to the $n=1$ state through application of a blue sideband operation [24]. To have a grid that spans the domain of the state, we scan around 16 rings in phase space set by $\pm N$, where $N = 1, 2, 3, 4, 5, 6, 8, 10$. Two of the 16 rings along which we measure are highlighted in Fig. 5.8(a), and plots of $S(\Theta, N; 0)$ versus Θ along those two rings are shown in Fig. 5.8(b). Notice in Fig. 5.8(b) that the larger SDK set ($N = 5$) separates the interferometer enough to see the oscillation of the motional distribution, while the smaller SDK set does not. Mapping along all 16 curves gives a nearly complete motional state map. The real part of the characteristic function is shown in Fig. 5.8(c) alongside the corresponding model of $\text{Re}[\chi_W(\alpha)]$ for an $n = 1$ Fock state in Fig. 5.8(d). The negative values of the characteristic quasiprobability function highlight the nonclassical nature of the motional state of the ion.

5.2.4 Limits of Measurement

These ultrafast tomographic techniques are capable of measuring motional energies far beyond the data presented here, which was limited to $\bar{n} \sim 10^4$ because of re-cooling issues during state preparation (it becomes difficult to cool the ion in a reasonable amount of time to start a new experiment after it has been heated to

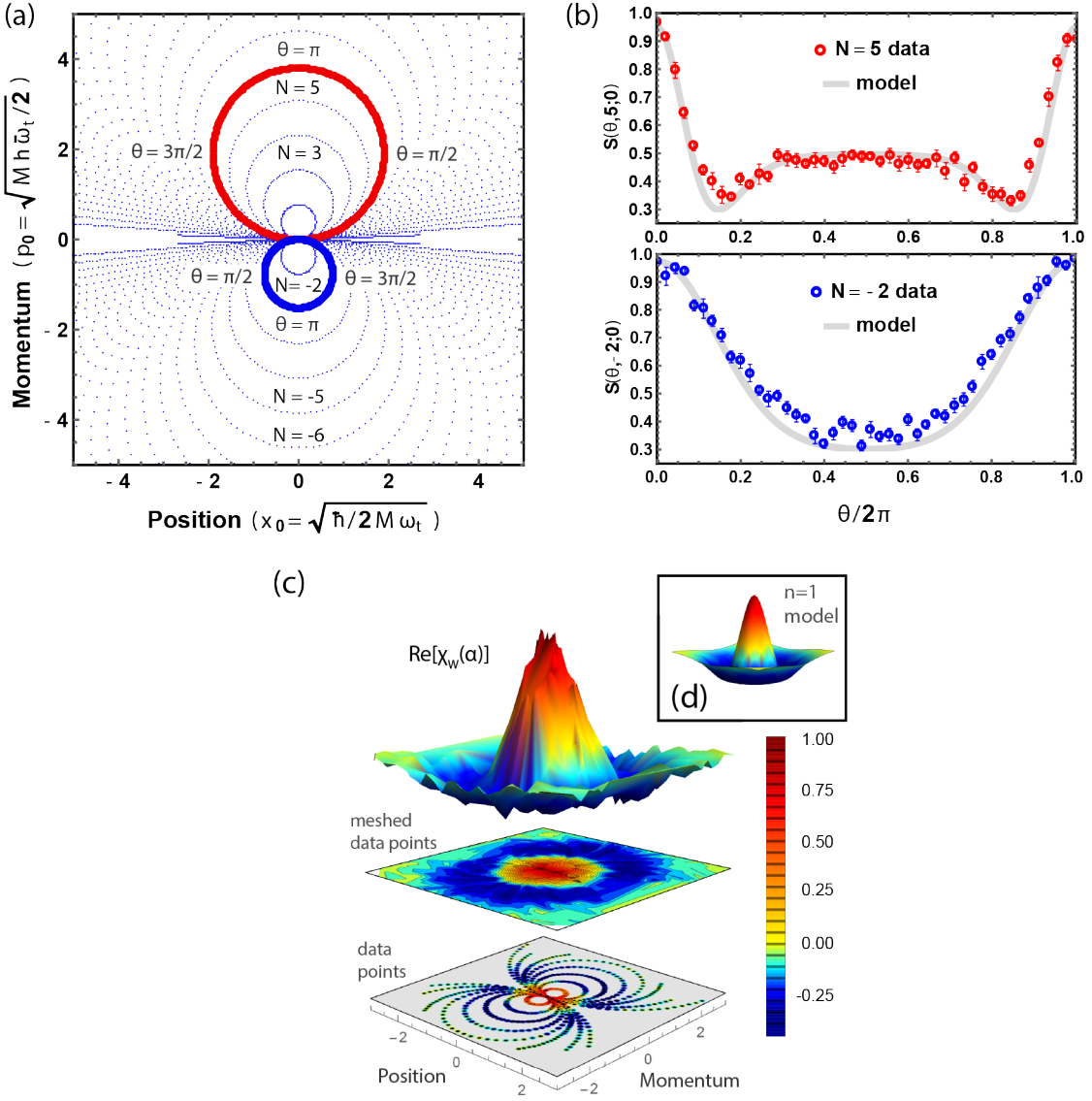


Figure 5.8: Ultrafast phase space tomography [71] (a) Points in phase space accessible in our tomographic measurements. The radius of each circle ($2N\eta$) is set by the number of kicks N , and the angular position on each circle is set by the SDK delay Θ . The sign of N represents the direction of the initial momentum kicks associated with the spin flip operators. (b) Sample of measurements of the Ramsey fringe at $\phi = 0$ for a nominal $n = 1$ Fock state, using two sets of kicks with $N = 5$ (red) and $N = -2$ (blue) and scanning the delay Θ . [The coordinates of these particular scans in phase space are highlighted in (a)]. (c) Motional state tomography of an ion prepared in the $n = 1$ Fock state. In ascending order: the value-colored data points of $\text{Re}[\chi_w(\alpha)]$ taken on 16 rings in phase space set by $\pm N$ where $N = 1, 2, 3, 4, 5, 6, 8, 10$, the interpolated data mapped in contour, and a 3D interpolation of the data. (d) Theory prediction for a Fock state with $n = 1$.

a very high tempertaure). In the experiment, we scan the motional interferometric angular delay Θ in steps set by the repetition rate of the laser, giving a resolution of $\omega/f_{rep} \sim 50$ mrad. For revival lineshapes narrower than this laser repetition rate limit, we scan Θ by changing the trap frequency ω though accurate control of the trap rf drive voltage. With fine drive-voltage control, we can achieve a resolution in Θ of 0.1 mrad, which would correspond to a contrast revival linewidth from a thermal state with $\bar{n} \sim 10^9$. Other factors also come into play when measuring such high-energy states: First, the spatial extent of motion swells beyond the laser beam waist. At $\bar{n} = 10^6$ for instance, or equivalent temperature $T = \hbar\omega\bar{n}/k_B = 80$ K, the ion would experience a significant gradient in the Rabi frequency across a beam with a $3\mu\text{m}$ waist. A second factor is the decreased detection fluorescence due to larger Doppler shifts at these energies. The detection fluorescence at $\bar{n} = 10^6$ would be reduced by a factor of $\sim 10^3$ from a cold ion [80]. Finally, when measuring these very narrow lineshapes, instabilities in the trap frequency ω and laser repetition rate f_{rep} would have to be sufficiently stable over the measurement time. At $\bar{n} = 10^6$, this would require a fractional stability from both the trap frequency and laser repetition rate of better than 0.1%. These factors put ultrafast interferometric measurements of $\bar{n} \geq 10^6$ neither fundamentally nor technically beyond reach.

5.3 Generation of quantum superpositions (“Cat states”)

Mesoscopic quantum superpositions, are widely studied for fundamental investigations of quantum measurement and decoherence [84] as well as potential ap-

plications in sensing [85] and quantum information science [86]. The generation and maintenance of such states relies upon a balance between efficient external coherent control of the system and sufficient isolation from the environment. Here we create a variety of cat states of a single trapped atom in a harmonic oscillator using ultra-fast laser pulses. These pulses produce high fidelity impulsive forces that separate the atom into widely-separated positions, without restrictions that typically limit the speed of the interaction or the size and complexity of the resulting motional superposition. This allows us to quickly generate and measure cat states larger than previously achieved in a harmonic oscillator, and create complex multi-component cat state superpositions in atoms.

Quantum superposition is the primary conceptual departure of quantum mechanics from classical physics, giving rise to fundamentally probabilistic measurements, nonlocal correlations in spacetime [13], and the ability to process information in ways that are impossible using classical means [86]. Quantum superpositions of widely separated but localized states, sometimes called “Schrödinger cat states” [87], exacerbate the quantum/classical divide. These states can be created in systems such as cold atoms and ions [88–90], microwave cavity QED with Rydberg atoms [91] and superconducting circuits [92–94], nanomechanical oscillators [95], and van der Waals clusters and biomolecules [96, 97]. All these systems gain sensitivity to outside influences with larger separations. The natural localized quantum state of a harmonic oscillator is the coherent state $|\alpha\rangle$ [74], which is a Poissonian distribution of oscillator quanta with mean $|\alpha|^2$. For a mechanical oscillator with mass m and frequency ω , the complex number α characterizes the position \hat{x} and momentum

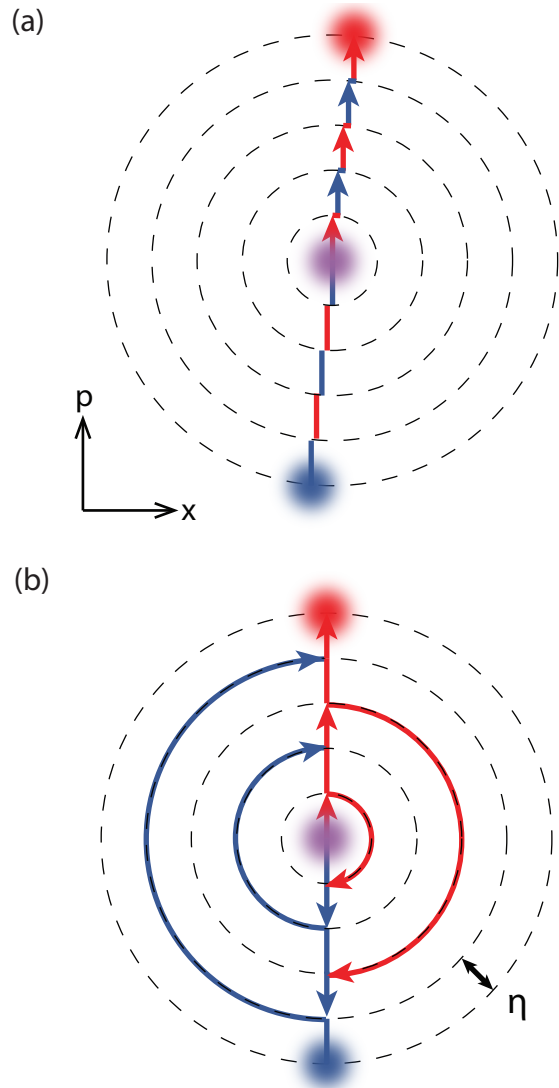


Figure 5.9: Every pulse from the laser can be used to create a large cat state by switching the kick direction between each SDK. We accomplish this change in Δk with a pulse picker right before it is split in the counterpropagating configuration. (b) Applying SDKs at intervals synchronous with half the trap follows a different scheme as (a) but with the trap switching the direction instead of the beams. Free evolution appears as circular orbits in this plot.

\hat{p} operators of the oscillator, with $\text{Re}[\alpha] = \langle \hat{x} \rangle / (2x_0)$ and $\text{Im}[\alpha] = \langle \hat{p} \rangle x_0 / \hbar$, where $x_0 = \sqrt{\hbar / (2m\omega)}$ is the zero-point width. Schrödinger Cat superpositions of coherent states $|\alpha_1\rangle + |\alpha_2\rangle$ of size $\Delta\alpha = |\alpha_1 - \alpha_2| \gg 1$ have been created in the harmonic motion of massive particles (phonons) [98] and in single mode electromagnetic fields (photons) [99]. In trapped ion systems, coherent states of motional oscillations are split using a qubit derived from internal electronic energy states [89, 100]. For photonic cat states, coherent states in a single mode microwave cavity are split using atoms or superconducting Josephson junctions. Recent experiments have created cat states with more than two components [101] for qubit storage and error protection [94]. In superconducting cavities, the size of the cat state is restricted to a maximum photon number of $\Delta\alpha^2 \sim 100$, due to nonlinearity of the self-Kerr and dispersive shift [94]. For trapped ions, cat states have been restricted to a regime where the motion is smaller than the wavelength of the light providing the dispersive force, or the “Lamb-Dicke” regime, which usually restricts phonon numbers also to $\Delta\alpha^2 \sim 100$ in the previous largest case (to our knowledge) [100] and $\Delta\alpha^2 \ll 100$ for the heavier Yb atom. Multicomponent cat states have not previously been created in the motion of atoms.

In the first of three experiment types, we demonstrate our fastest method for generating cat states by using every pulse that is emitted from a mode locked laser (repetition rate $f_{rep}=81.4$ MHz) to generate a set of N SDKs. This is achieved by separating each pulse from the laser into the eight pulses required for an SDK, in addition to adding optical elements capable of physically swapping the direction of the counter-propagating pulses (see fig. 5.9). Swapping the direction compensates

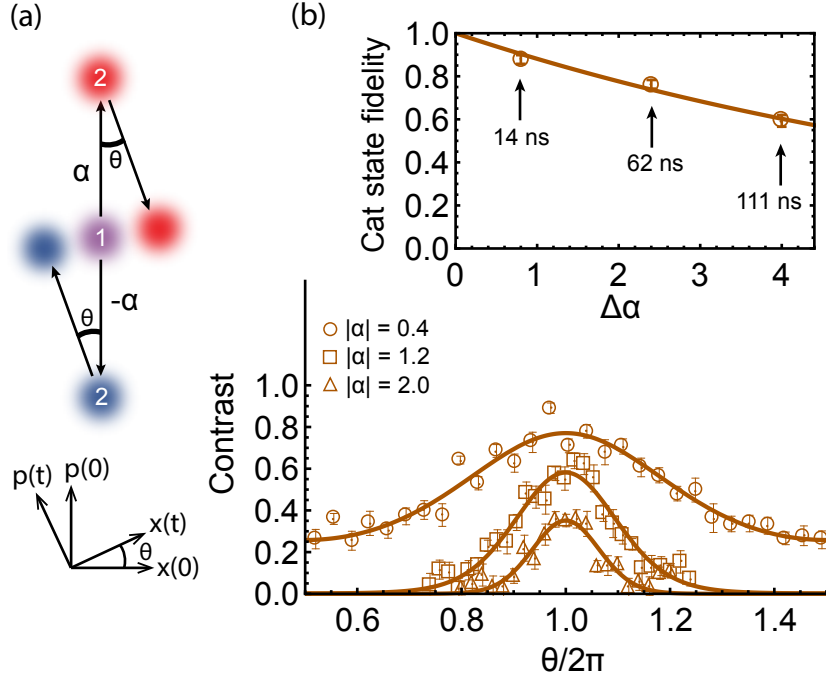


Figure 5.10: Fast Cat state creation and verification. (a) The state $|\psi_1\rangle$ (labeled “1”) is split using a set of SDKs to create the cat state $|\psi_2\rangle$ (“2”). After evolution $\theta = \omega T$, a second set of SDKs drives the state to $|\Psi_{cat}\rangle$. (b) The cat state $|\psi_2\rangle$ with $\alpha = 0.4$ is generated in about 14 ns, $\alpha = 1.2$ in 62ns, and $\alpha = 2.0$ in 111 ns. The states are verified by observing contrast in the state $|\Psi_{cat}\rangle$ (lower plot). We find the fidelity of each cat state $|\psi_2\rangle$ to be 0.88(2), 0.76(2), and 0.59(3), respectively (upper plot).

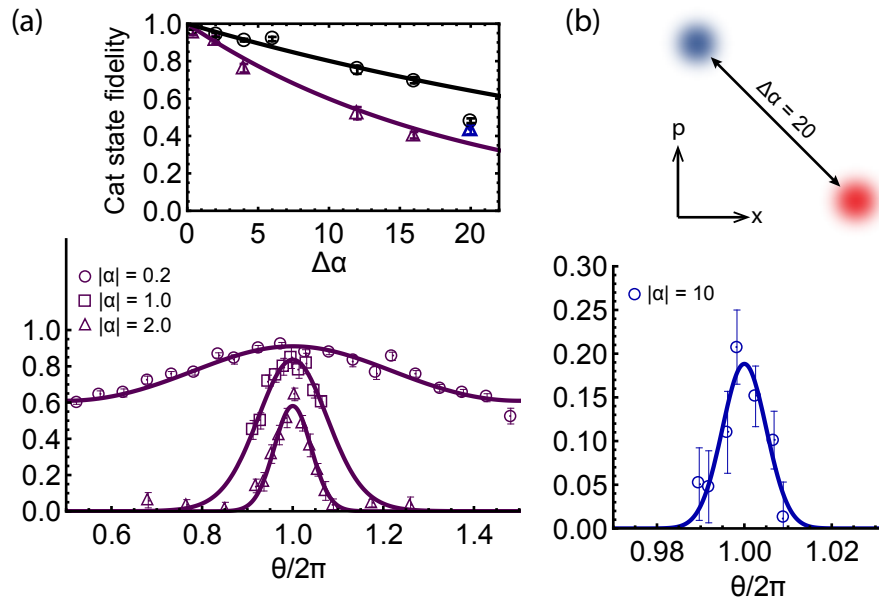


Figure 5.11: Slower Cat state creation and verification. (a) Using a higher fidelity technique which grows in α at an average rate $\eta\omega/\pi$, cat states are generated and verified by observing contrast revival (lower plot). Shown in the upper plot, cat state fidelity decays with the number of SDKs applied, and the effective single SDK fidelities are 0.9912(6) and 0.978(2) for Doppler (black, circles) and ground state cooled atoms(purple, triangles). (b) A cat state of $\Delta\alpha = 20$ is measured with a contrast revival peak of $C_0 = 0.19(3)$. Error bars are calculated with confidence interval of one sigma.

for the spin flip that occurs after each SDK and allows for fast concatenation of constructive momentum transfers. Starting each experiment, the ion is initialized in the state $|\psi_1\rangle = \frac{1}{\sqrt{2}}(|0\rangle + |1\rangle)|0\rangle$ using resonant microwaves. We apply a series of N SDKs which cause the superposition to grow in size at a rate $\frac{d|\alpha|}{dt} \approx \eta f_{rep}$ (this rate holds for small enough N , see fig. 5.9), approximately generating the cat state $|\psi_2\rangle = \frac{1}{\sqrt{2(1+e^{-|\alpha|^2})}}(|1\rangle|\alpha\rangle + |0\rangle|-\alpha\rangle)$. After allowing the state to evolve for varying amounts of time T , then applying a second identical set of displacement operators, the state

$$|\Psi_{cat}\rangle \propto |1\rangle|-\alpha e^{-i\Theta} + \alpha\rangle + |0\rangle|\alpha e^{-i\Theta} - \alpha\rangle \quad (5.15)$$

is ideally created, where $\Theta = \omega T$ (Fig. 5.10a). The phase of the second microwave $\pi/2$ pulse is scanned to probe the qubit contrast [34]

$$C(\Theta) = C_0 e^{-4|\alpha|^2(1-\cos\Theta)} \quad (5.16)$$

where C_0 is the signal amplitude and being < 1 accounts for imperfect operations. At integer multiples of the trap period $\Theta = 2\pi m; m \in \mathbb{Z}$, we observe revivals in contrasts, and when $|\alpha| \gg \frac{1}{\sqrt{2}}$, the revival lineshape is approximately Gaussian with a FWHM of $1.18/|\alpha|$. In fig. 5.10b, revival lineshapes at $\Theta = 2\pi$ are shown in which the state $|\psi_2\rangle$ is generated for (up to) $\Delta\alpha = 4.0$ in 111 ns with fidelity of $F = 0.59(3)$ estimated using the relation $F = C_0^{1/2}$. This gives an effective single SDK fidelity of 0.951(4), which is lower than that of a true single SDK because of power fluctuations associated with swapping laser directions. Such a demonstration is an important benchmark for ultrafast quantum information processing.

Following a second set of experiments, we create large cat states using a technique that does not require switching laser beam paths and instead works by delivering an SDK at every half trap period to excite large superpositions (Fig. 5.9 a). This maintains high SDK fidelity by leaving the beam paths stationary, and the cat state grows at an average rate of $\frac{d|\alpha|}{dt} = \eta\omega/\pi$. Using this method we produce and verify states $|\Psi_{cat}\rangle$ up to $\Delta\alpha = 20$ (Fig. 5.11 a,b). This largest state, with $100\hbar k$ of momentum in each coherent state, has a 209 nm maximum separation and contrast $C_0 = 0.19(2)$. Generating the large superposition state requires a high level of trap stability, which is achieved using a rf stabilization procedure [45]. Additionally, the trap frequency ω is scanned for fine control in Θ [71]. The total measured fidelity of each SDK is found to be 0.978(2) for displacing coherent states, and 0.9912(6) for Doppler cooled states. This discrepancy is most likely due to the slower rate of coherent cat state creation due to ground state cooling allowing slower drifts to have effects.

The speed, fidelity, and high level of control in ultrafast operations allows us to make more complicated, multicomponent cat states. First, we create three and four component cat states with one additional microwave pulse and SDK set. Starting from the state $|\psi_2\rangle$, a microwave $\pi/2$ pulse rotates the state to $|\psi_3\rangle \propto (|1\rangle - |0\rangle)|\alpha\rangle + (|1\rangle + |0\rangle)|-\alpha\rangle$. A set of SDKs then produces three and four component cat states of the form

$$|\Psi_{cat}^{3,4}\rangle \propto |1\rangle (e^{i\phi_1} |\alpha e^{-i\Theta} + \alpha\rangle + e^{i\phi_2} |\alpha e^{-i\Theta} - \alpha\rangle) + |0\rangle (e^{i\phi_3} |-\alpha e^{-i\Theta} + \alpha\rangle + e^{i\phi_4} |-\alpha e^{-i\Theta} - \alpha\rangle), \quad (5.17)$$

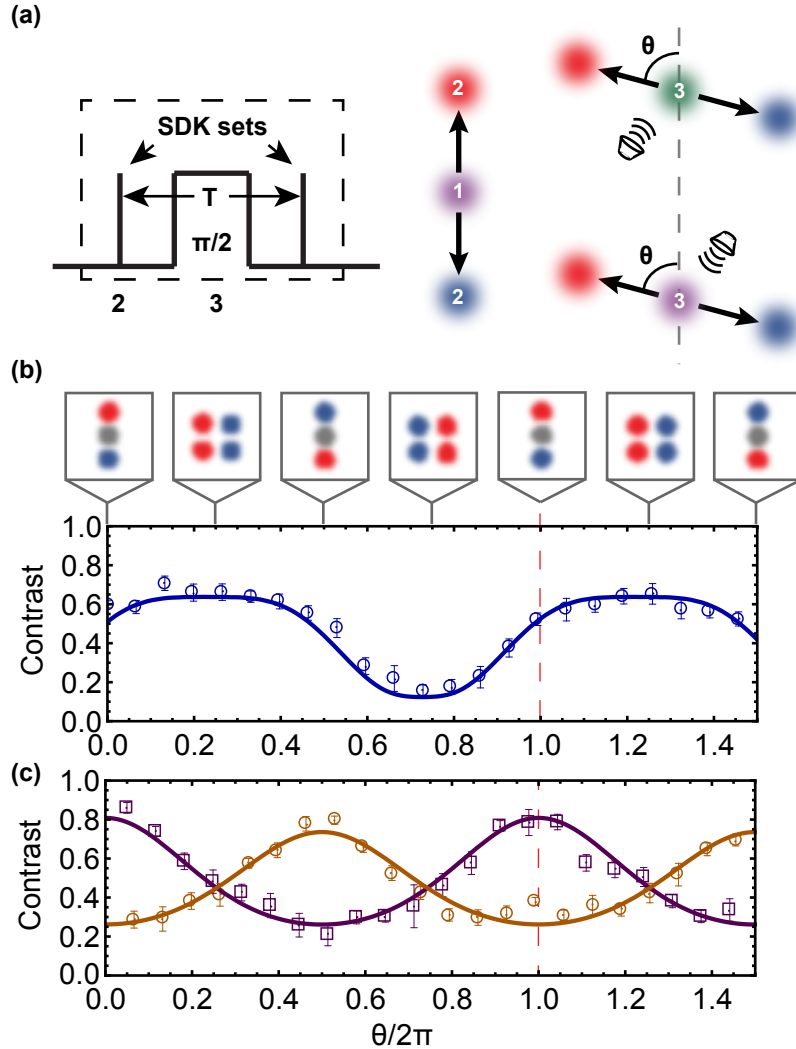


Figure 5.12: Three and four-component cat states. (a) Creation of a multicomponent cat state begins by applying a set of SDKs to take the state $|\psi_1\rangle$ (1) to the state $|\psi_2\rangle$ (2). A microwave $\pi/2$ pulse rotates the qubit to produce the state $|\psi\rangle \propto (|1\rangle + |0\rangle)|\alpha\rangle + (|1\rangle - |0\rangle)|-\alpha\rangle$ (3). Another set of SDKs generates the three or four-component cat state. (b) If $\Theta = 0$, two of the components rejoin and the state has the form $|\alpha\rangle + |0\rangle + |-\alpha\rangle$. If $\Theta = \pi/4$, for instance, then a four-component cat state of the form $|\alpha\rangle + |-\alpha\rangle + |i\alpha\rangle + |-i\alpha\rangle$ is generated. The final microwave pulse analyzes the state contrast, and is plotted as a function of Θ , which is compared with the predicted contrast curve with only the amplitude as a fitting parameter. Error bars are calculated with confidence interval of one sigma. (c) If the microwave $\pi/2$ pulse in (a) is replaced by a $m\pi$ pulse, then the second SDK set behaves as it would in the 2-component experiment, with the exception that odd values of m are shifted by half of a trap period. We see this behavior fits the predicted model well.

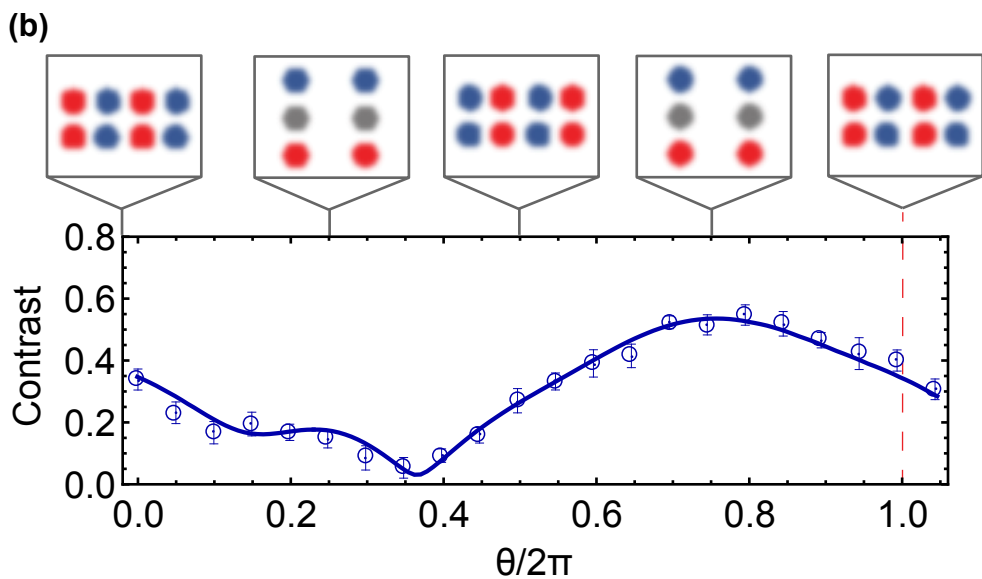
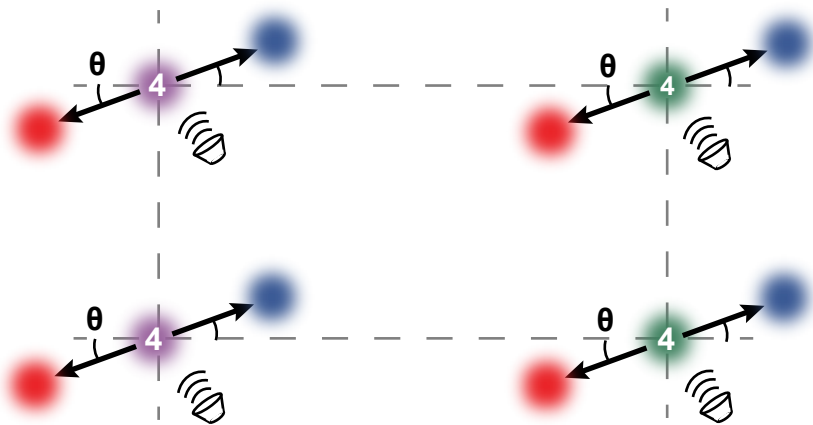
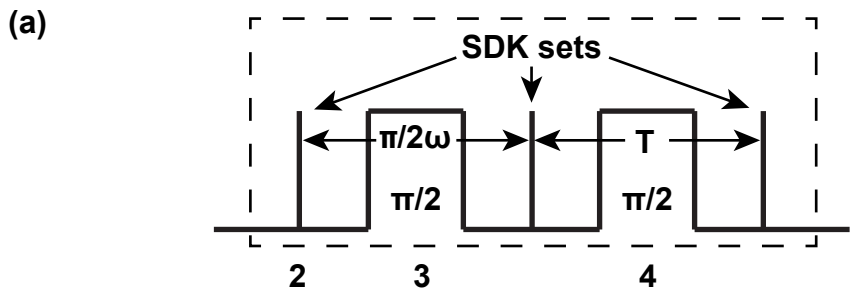


Figure 5.13: Six and eight-component cat states. (a) The six and eight-component state is created by extending the technique for the three and four-component state with an additional microwave pulse and SDK set. (b) Contrast as a function of Θ is used to verify the creation of the cat state when compared to the model (solid line).

with configuration depending on Θ (Fig. 5.12a). (phases ϕ_1 , ϕ_2 , ϕ_3 , and ϕ_4 discussed in Three and Four-Component Cat Contrast section). It is evident from Eq. 5.17 that a three-component cat state is created when $\Theta = m\pi$, and a four-component cat state is generated for other values of Θ . Scanning Θ and the phase of a final analysis microwave $\pi/2$ pulse, we observe a contrast lineshape indicative of the desired state (Fig. 5.12b). To further verify that these multicomponent states are being created, we run the same sequence but apply either no microwave pulse, or a π pulse, to the state $|\psi_2\rangle$. An SDK set then generates the cat states $|\Psi_{cat,0}\rangle \propto |1\rangle |-ae^{-i\Theta} + \alpha\rangle + |0\rangle |\alpha e^{-i\Theta} - \alpha\rangle$ and $|\Psi_{cat,\pi}\rangle \propto |0\rangle |\alpha e^{-i\Theta} + \alpha\rangle + |1\rangle |-ae^{-i\Theta} - \alpha\rangle$. These states revive at the same frequency, but out of phase by π , which is verified in Fig. 5.12c.

Continuing to unfold the state in phase space, another microwave $\pi/2$ rotation and SDK set generates a six and eight-component cat state (Fig. 5.13a). In this case, the four component cat state is generated with a separation along one quadrature double that of the other to allow for a square lattice once the eight component state is created. Again, scanning Θ and the phase of a final microwave pulse, Ramsey fringes are observed which compare well with the expected behavior (Fig. 5.13b). (See next sections for more details.)

Ultrafast laser pulses are capable of generating Schrödinger cat states larger than presented here, theoretically limited by the anharmonicity of the trap at large displacements. This technique can also be used to make even more complicated multicomponent states, as well as generate them in two and three dimensions by modifying the trapping potential and orientation. If a larger separation is desired

for a measurement such as rotation sensing [102], lowering the trap frequency by 10 times would increase the separation by 10 times.

5.3.1 Three and Four-Component Cat Contrast

The contrast function which overlays the data in Fig. 5.12b is derived here. We write the time evolution operator for a coherent state as $\hat{U}_T[\Theta]|\alpha\rangle = |\alpha e^{-i\Theta}\rangle$. The microwave rotation operator in the z-basis is written as

$$\hat{R}_\mu[\phi_\mu] = \frac{1}{\sqrt{2}}\hat{\mathbb{1}} \otimes \begin{bmatrix} 1 & e^{i\phi_\mu} \\ -e^{-i\phi_\mu} & 1 \end{bmatrix}, \quad (5.18)$$

where all rotations have pulse area $\pi/2$. A full Ramsey experiment to create three and four-component cat states, including microwave rotations, SDKs, free evolution, and a final analysis microwave pulse produces the final state

$$|\Psi_f^\beta\rangle = \hat{R}_\mu[\phi_\mu'''] \cdot \hat{O}_{SDK} \cdot \hat{U}_T[\pi] \cdot \hat{O}_{SDK} \cdot \hat{U}_T[\Theta] \cdot \hat{R}_\mu[\phi_\mu''] \cdot \hat{O}_{SDK} \cdot \hat{U}_T[\pi] \cdot \hat{O}_{SDK} \cdot \hat{R}_\mu[\phi_\mu'] \cdot |0\rangle |\beta\rangle. \quad (5.19)$$

The spin-up portion of the final state is given as

$$\begin{aligned} & \exp(-2i\eta\beta_R + 2i\eta\text{Re}[e^{-i\Theta}(2i\eta - \beta)] + i\phi_\mu'' - i\phi_\mu' - i\phi_\mu''') | -2i\eta - e^{-i\Theta}(2i\eta - \beta) \rangle \\ & - \exp(-2i\eta\beta_R - 2i\eta\text{Re}[e^{-i\Theta}(2i\eta - \beta)] - i\phi_\mu') | 2i\eta - e^{-i\Theta}(2i\eta - \beta) \rangle \\ & - \exp(2i\eta\beta_R - 2i\eta\text{Re}[e^{-i\Theta}(-2i\eta - \beta)] - i\phi_\mu'') | 2i\eta - e^{-i\Theta}(-2i\eta - \beta) \rangle \\ & - \exp(2i\eta\beta_R + 2i\eta\text{Re}[e^{-i\Theta}(-2i\eta - \beta)] - i\phi_\mu''') | -2i\eta - e^{-i\Theta}(-2i\eta - \beta) \rangle, \end{aligned} \quad (5.20)$$

where the normalization factor and spin-up ket is left out for simplicity. The brightness for any thermal state with average phonon occupation \bar{n} is given as

$$B = \frac{1}{\pi\bar{n}} \int_{-\infty}^{\infty} e^{-|\beta|^2/\bar{n}} \langle 1 | \Psi_f^\beta \rangle \langle \psi_f^\beta | 1 \rangle d^2\beta. \quad (5.21)$$

For an ion initially in a thermal motional state the brightness is

$$\begin{aligned} & \frac{1}{4} \left[1 + e^{16(1+2\bar{n})\eta^2(\cos\Theta-1)} \cos(\phi_\mu' - \phi_\mu''') \right] \\ & + \frac{1}{4} \left[1 - e^{-32(1+2\bar{n})\eta^2 \cos^2(\frac{\Theta}{2})} \cos(2\phi_\mu'' - \phi_\mu' - \phi_\mu''') \right] \\ & + \frac{1}{\sqrt{8}} e^{-8(1+2\bar{n})\eta^2} \sin(16\eta^2 \sin\Theta) \sin(\phi_\mu'' - \phi_\mu'''). \end{aligned} \quad (5.22)$$

5.3.2 Six and Eight-Component Cat Contrast

This calculation is carried out in the same fashion, using the full set of operations

$$\begin{aligned} |\Psi_f^\beta\rangle &= \hat{R}_\mu[\phi_\mu'''] \cdot \hat{O}_{SDK} \cdot \hat{U}_T[\pi] \cdot \hat{O}_{SDK} \cdot \hat{U}_T[\Theta] \\ &\cdot \hat{R}_\mu[\phi_\mu'''] \cdot \hat{O}_{SDK} \cdot \hat{U}_T[\pi] \cdot \hat{O}_{SDK} \cdot \hat{U}_T[\pi] \\ &\cdot \hat{O}_{SDK} \cdot \hat{U}_T[\pi] \cdot \hat{O}_{SDK} \cdot \hat{U}_T[\frac{\pi}{2}] \cdot \hat{R}_\mu[\phi_\mu''] \\ &\cdot \hat{O}_{SDK} \cdot \hat{U}_T[\pi] \cdot \hat{O}_{SDK} \cdot \hat{R}_\mu[\phi_\mu'] \cdot |1\rangle |\beta\rangle. \end{aligned} \quad (5.23)$$

We do not show the full brightness calculation here because of its length. The solid line in Fig. 5.13b is a fit assuming that the initial motional state is $\beta = 0$. Our initial thermal occupation number is $\bar{n} = 0.15$, or about 87% in the ground state. We do not take the thermal average because our computer could not perform the intensive calculation in less than a couple of days per run. A simpler calculation

including only the lowest phonon states would be simpler, but was not done because of the good agreement without averaging.

5.3.3 Sources of Error

Several factors lead to less than perfect fidelity of the cat states we create. One restriction on the size of cat states we can generate and measure comes from Doppler cooling issues. Frequency instability leads to fluctuations in the initial thermal state, leading to slower data taking (cooling takes longer, and the noisier data requires more averaging) and sensitivity to slow noise. The ion is exposed to off resonant light during the time that SDKs are being applied. This causes a Stark shift in the qubit splitting. SDK fidelity is discussed in other references [33, 71]. The trap axes are rotated so that the Raman beam couples only to a single mode. Misalignment of this means some amount of motion is excited in other directions, and is not recovered. Detection fidelity is discussed in other work [53]. Finally, it is worth acknowledging that the trap is about 1 mm across in both directions (the motional wave packet for the larges state has a spread of about 200 nm), and non-harmonic contributions are negligible to the motion behavior.

Chapter 6: Demonstration of a quantum gate with ultrafast pulses

Having build the theory and benchmarks of motional control using pulses we now focus on the main result of this thesis. For these experiments, we harmonically confine and laser cool two $^{171}\text{Yb}^+$ atomic ions to near the Doppler limit in a Paul trap [45]. Their motion is best described by two normal modes along each trap axis. The common, or center-of-mass (COM) mode, with frequency ω_C , describes motion where the ions oscillate in phase, while the relative mode, with frequency ω_R , describes oscillations where the ions oscillate out of phase. In this work, we tune these frequencies to $(\omega_C, \omega_R)/2\pi = (1.267, 1.170)$ MHz. The qubit levels are defined by the $^2S_{1/2}$ hyperfine levels $|F = 0, m_F = 0\rangle \equiv |0\rangle$ and $|F = 1, m_F = 0\rangle \equiv |1\rangle$, separated by $\omega_{\text{hf}}/2\pi = 12.64$ GHz. High fidelity state initialization and detection is performed by resonant excitation of the $^2S_{1/2}$ to the $^2P_{1/2}$ transition [54]. The collected light is imaged by a 0.6 NA lens with 500x magnification (see Fig.6.1). The large ion separation at the image plane allows individual state detection with two spatially separated photomultiplier tubes (PMTs), see [54]. The following chapter is based on the paper [103]

We achieve motional control through Raman interactions produced by counterpropagating pulses from a mode-locked laser with center wavelength $\lambda = 355$ nm,

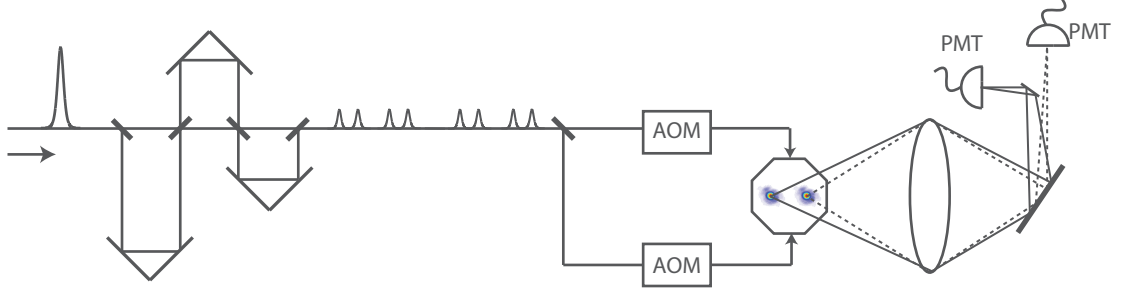


Figure 6.1: Experimental schematic. A single pulse from a mode-locked 355 nm laser is divided into 8 sub-pulses by three sequential optical delay stages. The shaped pulse is then split into two paths directed through independent AOMs, used to make the interaction direction-dependent. The pulses overlap in space and time at the position of the ions in a counterpropagating lin \perp lin polarization configuration that produces an SDK [104]. Following gate operations, the ion qubits are measured by collecting state-dependent fluorescence from the two ions on respective PMTs when resonant lasers are applied (not shown).

repetition rate $\omega_{\text{rep}}/2\pi = 81.42$ MHz and pulse duration $\tau \sim 20$ ps. Since further pulse shaping is necessary to achieve spin-motion dependence, we use three delay stages connected in series to divide each single pulse into eight subpulses. The pulse train is then split into two arms, and an acousto-optic modulator (AOM) shifts the frequency of each arm, with the two frequency shifts of opposite sign. The total frequency difference between the two arms is $\omega_A/2\pi = (\omega_{\text{AOM}1} + \omega_{\text{AOM}2})/2\pi = 468.73$ MHz. The pulse trains, which have orthogonal linear polarizations, are then sent to the ions. The timings of the subpulses, set by the lengths of the delay stages, is set so that the eight pulses coherently transfer population from $0|\alpha\rangle$ ($1|\alpha\rangle$) to $1|\alpha + 2\hbar k\rangle$ ($0|\alpha - 2\hbar k\rangle$), where $|\alpha\rangle$ is an arbitrary coherent state, and $k = 2\pi/\lambda$. This gives rise to a Spin Dependent Kick (SDK), with ideal unitary given by $\hat{U}_{\text{SDK}}(t_0) = \exp[i\phi_0]\hat{D}(i\eta)\hat{\sigma}_+ + \exp[-i\phi_0]\hat{D}(-i\eta)\hat{\sigma}_-$, where $\phi_0 = \omega_A t_0 + \phi_L$ is a laser phase related to the evolution of the AOMs and an offset ϕ_L assumed to be

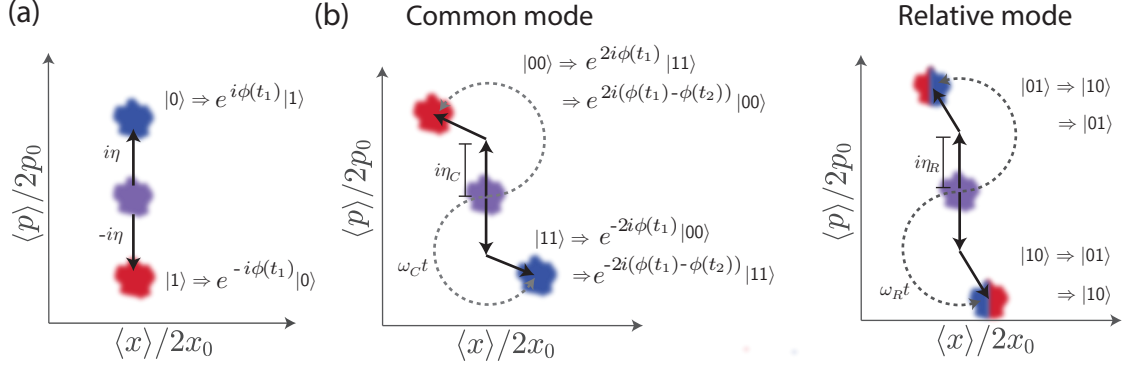


Figure 6.2: Setup of the displacements in phase space (a) The SDK displaces the motional state $|\alpha_0\rangle$ along the momentum axis with a magnitude proportional to η and flips the internal spin state. (b) A sequence comprised of an SDK, free evolution, and another SDK traces a different path in phase space of the two motional modes, which stems from the different displacement amplitudes and trap frequencies. Note that these plots are in a frame rotating at the trap frequency, so that free evolution corresponds to no displacement and the direction of an SDK depends on the time elapsed since the previous SDK.

constant during the interaction, $\hat{\sigma}_{\pm}$ are the spin raising and lowering operators, and $\hat{D}(\pm i\eta)$ are the coherent state displacement operators that impart momentum $\Delta p = \pm 2\hbar k = \pm \eta \hbar / x_0$. The Lamb-Dicke parameter $\eta = \Delta k x_0$, where $x_0 = \sqrt{\frac{\hbar}{2m\omega}}$ is the harmonic oscillator length for an atom with mass m , trap frequency ω , and wavevector difference Δk between the counterpropagating beams ($\Delta k \approx 2k$). In contrast to the resolved sideband regime used extensively in ion trapping experiments, the SDK operates in the impulsive limit and is about three orders of magnitude faster than either trap oscillation period ($\tau_{SDK} \ll 2\pi/\omega_{C,R}$). Note that the Lamb-Dicke approximation is not invoked in the derivation of the SDK operator [24].

The action of a SDK on two ions is given by

$$\begin{aligned}\hat{U}_{SDK}(t_0) = & e^{2i\phi(t_0)} \hat{\sigma}_{+1} \hat{\sigma}_{+2} \hat{D}_C[i\eta_C] + \\ & e^{-2i\phi(t_0)} \hat{\sigma}_{-1} \hat{\sigma}_{-2} \hat{D}_C[-i\eta_C] + \\ & \hat{\sigma}_{+1} \hat{\sigma}_{-2} \hat{D}_R[i\eta_R] + \hat{\sigma}_{-1} \hat{\sigma}_{+2} \hat{D}_R[-i\eta_R],\end{aligned}\quad (6.1)$$

where $\eta_C = \sqrt{2}\eta = 0.24$ and $\eta_R = \sqrt{2\omega_C/\omega_R}\eta = 0.25$ are the Lamb-Dicke parameters for the COM and relative modes, respectively. We note that the laser phase ϕ affects the COM mode only. Due to the different displacement amplitudes and different amounts of trap evolution, the COM and relative modes trace a different path in phase space when subjected to a sequence of SDKs and free trap evolution. It is most convenient to display the trajectories in a frame rotating at the trap frequency (see Fig. 6.2c), where free evolution corresponds to no displacement and the each kick has magnitude $\eta_{C,R}$, and at an angle of $\omega_{C,R}t$ from the previous kick.

A sequence of SDK pulses indexed to uniform time steps of duration $T = 1/f_{\text{rep}}$ can be expressed by N displacement indices $\{b_1, b_2, \dots, b_N\}$ with $b_n = 1$ corresponding to a kick as described above, $b_n = -1$ corresponding to a kick with reversed beam directions ($\Delta k \rightarrow -\Delta k$), and $b_n = 0$ corresponding to a wait (no pulse). This sequence leads to displacements of initial coherent states for each mode m from $|\alpha_0\rangle_m$ to $e^{i\phi_m}|\alpha\rangle_m$, with [31]

$$\alpha = e^{-iN\omega_m T} \left(\alpha_0 + i \sum_{n=1}^N \eta_m b_n e^{in\omega_m T} \right) \quad (6.2)$$

$$\begin{aligned}\phi_m &= \mathcal{R}e \left(\alpha_0 \sum_{n=1}^N \eta_m b_n e^{-in\omega_m T} \right) \\ &+ \sum_{n=2}^N \sum_{j=1}^{n-1} \eta_m^2 b_n b_j \sin[\omega_m T(n-j)].\end{aligned}\quad (6.3)$$

We design pulse sequences $\{b_n\}$ so that the sum in Eq. 6.2 vanishes and both motional phase spaces close. Given an even number of pulses, this produces a phase gate described with truth table

$$\begin{aligned} |00\rangle &\Rightarrow e^{i\gamma} e^{i\Phi_g} |00\rangle \\ |10\rangle &\Rightarrow |10\rangle \\ |01\rangle &\Rightarrow |01\rangle \\ |11\rangle &\Rightarrow e^{-i\gamma} e^{i\Phi_g} |11\rangle, \end{aligned} \tag{6.4}$$

The nonlinear geometric phase $\Phi_g = \phi_C - \phi_R$ is set to $\pi/2$ for maximum entanglement. The residual linear phase from the series of optical kicks is

$$\gamma = 2\omega_A T \sum_{n=1}^N (-1)^{\sum_{j=1}^n |b_j| + 1} n |b_n|, \tag{6.5}$$

where the alternating signs account for the qubit spin flip after each SDK. Note that because the number of pulses is even, the net gate evolution is insensitive to the optical phase ϕ_L , which is assumed to be constant over the course of the gate.

Here, we implement a quantum gate with fast pulses by finding gate sequences with the least number of SDKs, without reversing the beam directions (restricting $b_n = 0$ or 1). For N_p individual pulses separated in time by an integer multiple M of the laser pulse period T , the condition for closing phase spaces is similar to the tracing of a regular polygon in the complex plane. We achieve the largest nonlinear gate phase for a given number of pulses by driving the COM and relative modes in opposite directions in phase space so that $\phi_R \approx -\phi_C$.

Using the above trap parameters with $N_p = 10$, we find that the phase space

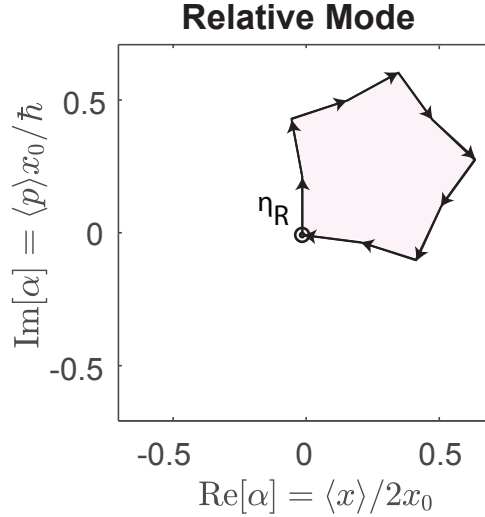
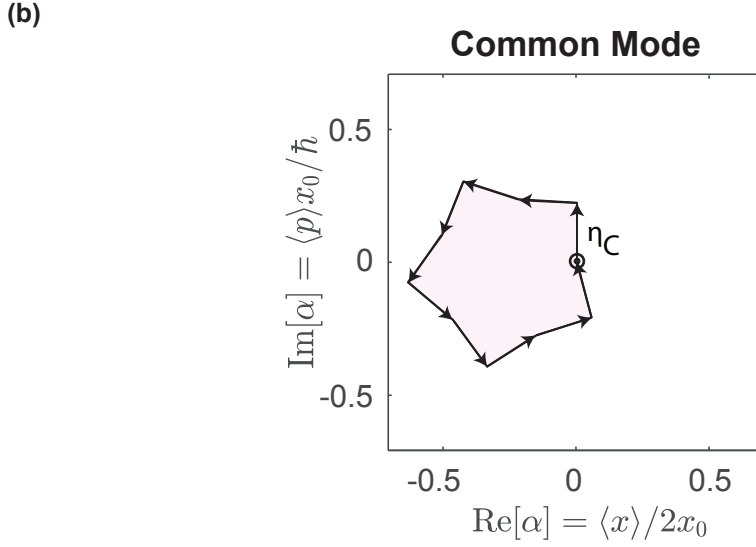
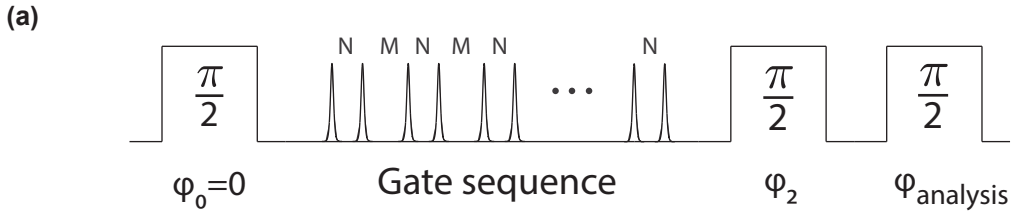


Figure 6.3: Gate sequence and parity measurements (a) The gate sequence is applied within a Ramsey experiment. The entangling gate contains 5 repetitions of a sequence consisting of a single SDK ($b_n = 1$), followed by a wait of N time steps ($b_n = 0$), another SDK ($b_n = -1$), and a final wait of M time steps. (b) Depiction of the trajectories followed by the COM and relative modes for a fully entangling sequence. They follow opposite circulations, enclose similar areas, and the sum leads to the gate phase.

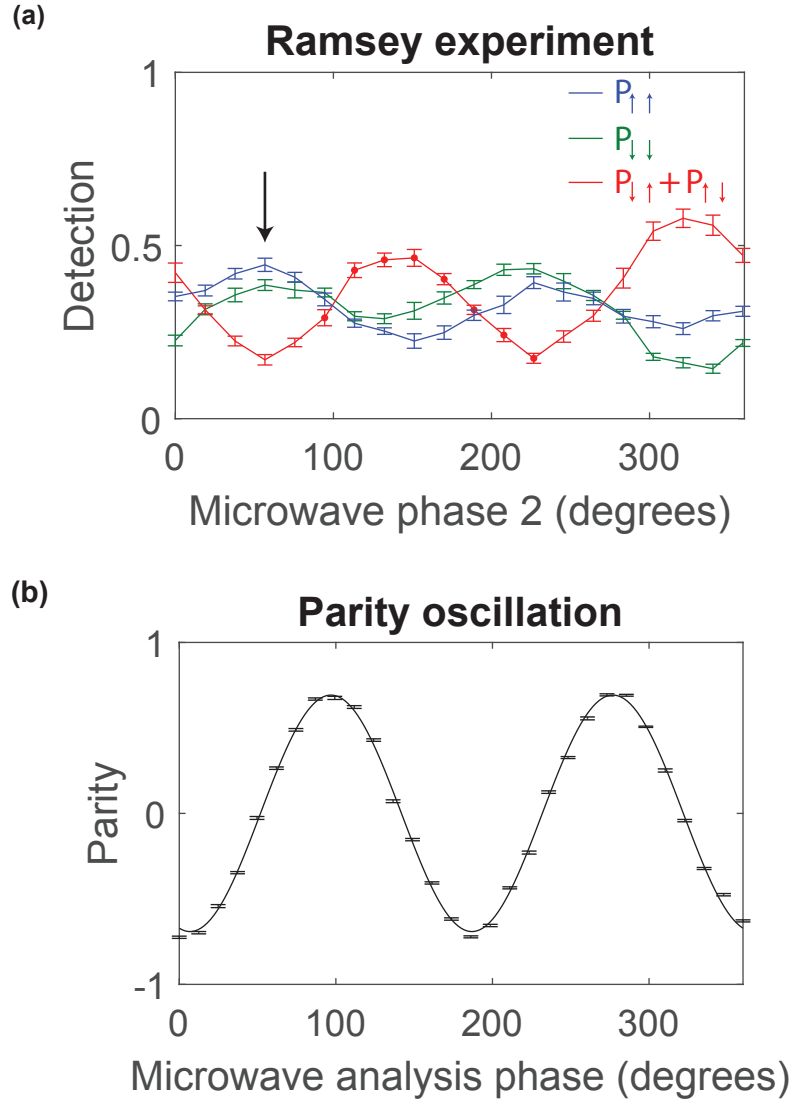


Figure 6.4: Gate sequence and parity measurements results. (a) We choose ϕ_2 such that we maximize P_{11} , P_{00} and minimize P_{01} , P_{10} (black arrow). Population in $|10\rangle$ and $|01\rangle$ is due mostly to SDK infidelity. (b) The parity oscillation amplitude after choosing the leftmost value of ϕ_2 in (a) is proportional to $2\rho_{11,00}$, which allows us to compute the fidelity. The best parity oscillation amplitude achieved is 0.69(1), leading to a final gate fidelity of 76(1)%.

trajectories of COM and relative modes trace out regular decagons of opposite circulation for $M = 166$, with corresponding gate phase $\Phi_g = \pi/1.67$. Other values of Φ_g can be realized by alternating between two different integer multiples of the pulse periods, M_1 and M_2 , such that $M_1 + M_2 = 2M$. This deforms the trajectories to decagons with two distinct vertex angles (see Figs. 6.3b and 6.5a), allowing the fine tuning of Φ_g . For $M_1 = 175$, $M_2 = 157$, we find $\Phi_g = \pi/2.06$, nearly a fully entangling gate in a total duration of $(N_p M - M_2)T = 18.5 \mu\text{s}$. There are many more types of pulse solutions with even more complex polygonal trajectories given the delay times between pulses.

We characterize the phase gate by applying the gate operation within a three-pulse Ramsey interferometer on the qubits. We start the sequence by optically pumping the ions to the state $|00\rangle$. A first microwave $\pi/2$ -pulse rotates both spins to populate an equal superposition of all 4 basis states. The entangling laser pulse sequence is then applied, which according to the truth table (eq. 6.4) should ideally produce the state

$$\Psi_e = \frac{e^{i\Phi_g}}{2} (e^{i\gamma}|00\rangle + e^{-i\gamma}|11\rangle) - \frac{1}{2} (|10\rangle + |01\rangle), \quad (6.6)$$

where in the above expression we have suppressed the motional state, since both phase spaces should be closed at this point.

A second $\pi/2$ microwave Ramsey pulse of variable phase with respect to the first pulse is then applied. We choose its phase to ideally create the state

$$\Psi_f = \frac{e^{-i\gamma}}{2} (e^{i\Phi_g} - 1)|00\rangle + \frac{e^{i\gamma}}{2} (e^{i\Phi_g} + 1)|11\rangle. \quad (6.7)$$

We experimentally determine the appropriate phase of the second Ramsey $\pi/2$ pulse

by maximizing the populations P_{11} and P_{00} of the even parity states, as shown in the Ramsey fringes of Fig. 6.4a.

In order to verify the coherence of the above entangled state, we apply a third $\pi/2$ “analysis pulse” and measure the parity of the two qubits as a function of this last pulse, as shown in Fig. 6.4b. The parity oscillates with twice the period of a single spin, and the contrast C of the oscillation reveals the coherence between the entangled superposition in Eq. 6.7. The state fidelity with respect to the ideal Bell state is then $F = (P_{11} + P_{00} + C)/2$ [105]. We measure a Bell state fidelity of $F = 76(1)\%$.

As a further validation of our control over various gate sequences, we vary the gate phase Φ_g by changing the number of pulses M_1 and M_2 over a wider range. In Fig. 6.5a we show a measurement of the parity oscillation contrast C for different values of Φ_g . The measured parity oscillation amplitude for each gate sequence agrees well with the expected $\sin \Phi_g$ dependence. Finally, we note that the linear phase γ can be regarded as a constant offset phase in the above data and does not affect the amount of entanglement or its diagnosis.

The entangling gate presented here is fundamentally different than the Mølmer-Sørensen [8] and Cirac-Zoller [7] gates for trapped ions, since individual motional modes are not resolved. Moreover, the (thermal) motion of the ions occupies a spatial extent of $x_0\sqrt{2\bar{n}+1} \approx 0.8/\Delta k$, outside the Lamb-Dicke regime.

The gate can be made much faster by dynamically switching the laser beam wavevector difference Δk and thus using negative values of b_n in the pulse schedule to close phase spaces more quickly [32]. We have identified potential gate se-

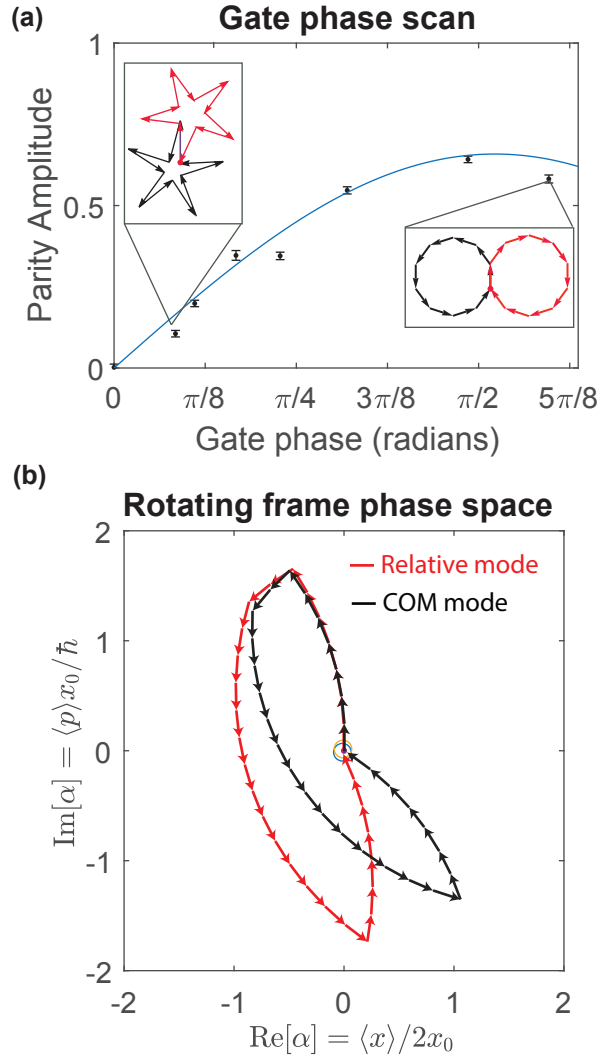


Figure 6.5: Parity vs. Gate phase. (a) Measured parity oscillation amplitude for various values of the gate phase Φ_g , which should be proportional to $\sin \Phi_g$ (solid blue line). The gate phase is modified by changing the pulse schedule given by the integers M_1 and M_2 (see main text). The insets show phase space trajectories for the COM (red) and relative (black) modes for $\Phi_g = \pi/1.67$ (right) and $\Phi_g = \pi/11.9$ (left). The fidelity of the entangled state produced in each case, referenced to the ideal state $\Psi_f(\Phi_g)$ in Eq. 6.7, is roughly 0.7 for all the measurements. (b) Theoretical pulse sequence for a maximally entangling gate made out of 30 SDKs with a total gate time of 921 ns. The modes are kicked consecutively by switching the directions of the beams to create a “lever arm” for geometrical phase acquisition.

quences with net gate times shorter than $1 \mu\text{s}$, as shown in Fig. 6.5b, with the same trap parameters used above. Experimentally, fast switching can be accomplished by inserting a second electrooptic Pockels cell after the two AOMs, as previously demonstrated for the generation of large Schrödinger cat states [72]. However, extension of this setup for high-fidelity 2-qubit gates remains challenging because of instabilities in the positioning and polarization of the high power ultraviolet beams traversing the Pockels cell. In the future, it may be possible to control infrared optical sources instead of the ultraviolet lasers used here, by frequency-upconverting to the ultraviolet after pulse-shaping/switching, or exploiting a longer-wavelength atomic transition for the SDK.

Chapter 7: Conclusions and outlook

We have described a different scheme of atom entanglement that operates in the fast regime by using ultrafast pulses. The strong atom-light coupling allows operation speeds comparable to that of solid state systems. Physically, the speed of the presented entangling operation is only limited by the Coulomb interaction with a lower bound given by $T_{\text{Coulomb}} = d/c \approx 10^{-14}$ s where d is the distance between the ions. A reasonable practical implementation is only limited by the laser repetition rate, which can go as high as few Terahertz and thus bounding the maximum entanglement rate by a few nanoseconds.

It is interesting to notice that in the quantum case, contrary to the classical case, higher clock/operation rates do not imply an overhead in heat management since lattice vibrations do not play a role, on the contrary, the quantum operations in the fast regime become less sensitive to any external disturbance since the evolution during the interaction can be considered frozen in time. Dissipation would only take part when the number of operations is commensurate to the probability of spontaneous emission of about $\sim 10^6$ in our case [37]. The possibility of noise insensitive operations and exceptionally long atom coherence times results in a promising and exciting route for scaling a quantum computer.

Not limited to quantum information applications, the SDKs presented here are building blocks for other experiments such as:

1. Pulse shaping of Infrared (IR) pulses for quantum control applications.
2. Imaging of large cat states separated by more than a hundred times the ground state spread.
3. Studies of the delta-kicked Harmonic Oscillator and quantum chaos.
4. Superfast cooling.

Future experimental work should focus on gaining a better understanding of the SDK fidelity since for the experiments described above, high SDK numbers are required. Potential limitations include beam pointing instabilities, small couplings to the magnetically sensitive states in the ground state manifold, crosstalk between the desired modes and other motional modes along different trap axes, and imperfect polarization control due to the finite extinction ratio of UV Pockels cells. A good unexplored route would certainly be the creation of SDKs with IR femtosecond laser pulses since it would be able to circumvent the inherent issues of working with UV optics such as poor polarization control of the pulse picking devices. Such scheme could work by doubling the IR light immediately before going to the ions. Unfortunately, by the time of writing this thesis, the experiment is no longer active and no answers to the fidelity problem will be seen in the foreseeable future.

Appendix A: Normal mode spectrum numerical calculation

Routine for finding the ions' equilibrium position:

```
1 function F = equilibrium_positions(u)
2
3 F = length(u);
4 N = length(u);
5 %first summation
6 for m = 1:N
7     S1 = 0;
8     S2 = 0;
9     %first summation
10    for n = 1:m-1
11        S1_aux = 1/((u(m)-u(n)).^2);
12        S1 = S1 + S1_aux;
13    end
14    %second summation
15    for jj = m+1:N
16        S2_aux = 1/((u(m)-u(jj)).^2);
17        S2 = S2 + S2_aux;
18    end
19
20 %whole expression
21 F(m) = u(m) - S1 + S2;
22
23
24 end
25
26 end
```

Routine to calculate the transverse and axial normal modes

```
1 clear
2 clc
3 % Equations taken from
4
5 fun = @equilibrium_positions;
6 Number_of_modes = 55;
7 x0 = linspace(-4,4,Number_of_modes); %Arbitrary initial guess
8
9 u = fsolve(fun,x0) %Numerical solution for the equilibrium positions
10 omega_Z = 2*pi*0.20e6;
11 omega_COM = 2*pi*4.2e6;
12
13 % General variable declaration
14 A = zeros(length(u),length(u));
15 A_aux=0;
16 Summa = 0;
```

```

17
18 %% TRANSVERSE MODES
19 for n = 1:length(u)
20     for m = 1:length(u)
21
22         if n == m
23             %Runs for all the number of ions N which is the same as the normal modes
24             for p=1:length(u)
25                 % take the p's different than n to avoid self interaction
26
27                 val =(1/(abs(u(n)-u(p)).^3));
28
29                 if val == Inf
30                     Summa_aux = 0;
31                 else
32                     Summa_aux = (1/(abs(u(n)-u(p)).^3));
33                 end
34
35                 Summa = Summa + Summa_aux;
36
37             end
38
39             A_aux = (omega_COM/omega_Z)^2 - Summa;
40             Summa = 0;
41             elseif n ~= m
42
43                 A_aux = 1/(abs(u(n)-u(m)).^3);
44
45             end
46
47         end
48         A(n,m)= A_aux;
49     end
50 A_aux = 0;
51
52 end
53
54 [V,D] = eig(A,'nobalance')
55 f_traps = sqrt(diag(D)).*omega_Z/(2*pi)
56
57 figure1 = figure('Units','Centimeters','position',[2 2,16 6])
58 stem(f_traps/(1e6),ones(length(f_traps),1),'Marker','none')
59 axis([-1.5,omega_COM/(2*pi*1e6)+1,0,1.05])
60 title('Motional mode frequencies')
61 xlabel('Frequency (MHz)')
62 ylabel('Amplitude')
63 hold on
64
65 %%%%%% AXIAL MODES %%%%%%
66 for n = 1:length(u)
67     for m = 1:length(u)
68
69         if n == m
70
71             for p=1:length(u) %Runs for all the number of ions N which is the same as the
72                 % normal modes take the p's different than n to avoid self interaction
73
74                 val =(1/(abs(u(n)-u(p)).^3));
75
76                 if val == Inf
77                     Summa_aux = 0;
78                 else
79                     Summa_aux = (1/(abs(u(n)-u(p)).^3));
80                 end
81
82                 Summa = Summa + Summa_aux;
83
84             end

```

```

85
86     A_aux = 1 + 2*Summa;
87     Summa = 0;
88 elseif n ~= m
89
90     A_aux = -2 / (abs(u(n)-u(m)).^3);
91
92 end
93
94 A(n,m) = A_aux;
95 end
96 A_aux = 0;
97
98 end
99
100 [V,D] = eig(A,'nobalance')
101 f_Z_traps = sqrt(diag(D)).*omega_Z/(2*pi)
102 stem(f_Z_traps/(1e6),0.7*ones(length(f_Z_traps),1),'Marker','none','Color','r')
103 axis([-0.5,6.5,0,1.05])
104 title('Motional mode frequencies')
105 xlabel('Frequency (MHz)')
106 ylabel('Amplitude')

```

Appendix B: Ion loading code (Python)

```
1 % Standard imports
2 import cv2
3 from PIL import ImageGrab
4 import matplotlib.pyplot as plt
5 import numpy as np
6 from skimage.feature import blob_log, blob_dog, blob_doh
7
8
9 while(True):
10
11     % Read image
12     screen = np.array(ImageGrab.grab(bbox=(125, 440, 1000, 800)))
13     screen = cv2.cvtColor(screen, cv2.COLOR_BGR2RGB)
14     ions_raw = cv2.cvtColor(screen, cv2.COLOR_RGB2GRAY)
15     ions = cv2.medianBlur(ions_raw, 5)
16
17     blobs_points_unsorted = blob_log(ions, max_sigma=5 , threshold=0.10)
18
19     %Sorting elements
20     blobs_points = blobs_points_unsorted[blobs_points_unsorted[:,1].argsort()]
21
22     %Compute derivatives for dark ion count
23     single_derivative = np.diff(blobs_points[:,1],n=1,axis=0)
24     double_derivative = np.diff(np.diff(blobs_points[:,1],n=1,axis=0),n=1,axis=0)
```

Appendix C: Doppler Cooling limit

Following [51], we can calculate the equilibrium total energy of a bounded atom. First, an scattering event from an ion with mass m and velocity \vec{v} absorbing a photon from an incoming cooling laser with wavevector \vec{k} will emit a photon with wavevector \vec{k}_s and change its initial velocity to \vec{v}' . Conservation of momentum and energy in the non relativistic regime where the ion's velocity is much smaller than the speed of light is

$$\Delta\vec{p} = m(\vec{v}' - \vec{v}) = \hbar(\vec{k}_i - \vec{k}_s), \quad (\text{C.1})$$

$$\begin{aligned} \Delta E &= \frac{1}{2}m(\vec{v}')^2 + \frac{1}{2}(\vec{v})^2 \\ &= \frac{\hbar^2(\vec{k} - \vec{k}_s)^2}{2m} + \hbar(\vec{k} - \vec{k}_s) \cdot \vec{v} \\ \Delta E_i &= \frac{\hbar^2(k_i - k_{si})^2}{2m} + \hbar(k_i - k_{si})v_i \quad (i = x, y, z) \end{aligned} \quad (\text{C.2})$$

We write the cartesian components i for clarity in the next derivations.

We will assume that the cooling beam is close to the transition resonance ω_0 and that the recoilled photon's wave-vector is similar to the incident photon in magnitude ($|k| \approx |k_s|$). Equation C.3 can then be written in terms of the recoil energy $R = \hbar k^2/2m$

$$\Delta E_i = R(\hat{k}_i^2 - 2\hat{k}_i\hat{k}_{si} + \hat{k}_{si}^2) + \hbar(k_i - k_{si}), \quad (\text{C.4})$$

the \hat{k}_i and \hat{k}_i are the wave-vectors i unit components and are not necessary equal to unity when squared since they can represent different directions, some of them might be zero for the overall ΔE .

The situation described above accounts for a one photon in and one photon out event and if we want to calculate an average rate of energy, we must perform an average over all the angles where a photon can be scattered with probability $P_s(\hat{k}_s)$ into a solid angle $d\Omega$ in the \hat{k}_s direction:

$$\langle \Delta E_i \rangle_s = \int P_s(\hat{k}_s) \Delta E_i d\Omega = R(f_i + f_{si}) + \hbar k_i v_i, \quad (\text{C.5})$$

where $f_i = \hat{k}_i^2$, $f_{si} = \int P_s(\hat{k}_s) \hat{k}_{si}^2 d\Omega$ and we have dropped out the terms linear in \hat{k}_{si} since the probability $P_s(\hat{k}_s)$ is an even function and it depends of the transition. For isotropic emission, we have $P_s(\hat{k}_s) = 1/4\pi$ (same probability of emitting in 4π) and $f_{si} = 1/3$.

To obtain a rate, we must multiply eq. C.5 with the scattering rate [53] defined for a laser interacting with an atom moving at velocity \vec{v} as

$$R_{scat}(\omega_0, \vec{v}) = \frac{\Gamma}{6} \frac{s_0}{1 + \frac{2}{3}s_0 + \left(\frac{2(\omega_0 - \omega_L + \vec{k} \cdot \vec{v})}{\Gamma} \right)^2}, \quad (\text{C.6})$$

where ω_L is the laser frequency, ω_0 is the transition resonance, $\vec{k} \cdot \vec{v}$ to accounts for Doppler shifts, Γ is the natural transition linewidth and $s_0 = I/I_{\text{sat}} = 2\Omega^2/\Gamma^2$ is the fractional saturation transition intensity with Ω as the resonant Rabi frequency. The expression C.6 takes into account the pumping to dark states [106] and is suitable for $^{171}\text{Yb}^+$ (for $^{174}\text{Yb}^+$, only a few constants change).

The rate of change of energy is then

$$\frac{dE_i}{dt} = \langle R_{scat}(\omega_0, \vec{v}) R(f_i + f_{si}) + \hbar k_i v_i \rangle, \quad (\text{C.7})$$

and we can linearize expression C.6 in the low Doppler limit $\vec{k} \cdot \vec{v} \ll (\omega_0 - \omega_L) = \Delta$:

$$R_{scat}(\omega_0, \vec{v}) \approx \frac{\Gamma}{6} \frac{s_0}{1 + \frac{2}{3}s_0 + \left(\frac{4\Delta^2}{\Gamma^2}\right)} \left(1 - \frac{8\Delta \vec{k} \cdot \vec{v}}{\Gamma^2(1 + \frac{2}{3}s_0) + 4\Delta^2}\right), \quad (\text{C.8})$$

and the energy rate equation in steady state ($\frac{dE_i}{dt} = 0$) becomes

$$\begin{aligned} 0 &= \left\langle \left(1 - \frac{8\Delta k_i v_i}{\Gamma^2(1 + \frac{2}{3}s_0) + 4\Delta^2}\right) (R(f_i + f_{si}) + \hbar k_i v_i) \right\rangle \\ \langle R(f_i + f_{si}) \rangle &= \left\langle \frac{8\hbar \Delta f_i k^2 v_i^2}{\Gamma^2(1 + \frac{2}{3}s_0) + 4\Delta^2} \right\rangle \\ E_{k_i} &= \frac{m \langle v_i^2 \rangle}{2} = \frac{\hbar \Gamma}{8} \left(1 + \frac{f_{si}}{f_i}\right) \left[\frac{\Gamma(1 + \frac{2}{3}s_0)}{4\Delta} + \frac{\Delta}{\Gamma} \right]. \end{aligned} \quad (\text{C.9})$$

Where we have used the fact that $\langle v_i \rangle = 0$ and $\langle v_i v_j \rangle = 0$ for $i \neq j$.

Appendix D: Zernike Polynomials

Although optical aberrations can be described in terms of a Taylor expansion of the object height and pupil coordinates, Zernike polynomials $Z_n^m(\rho, \theta)$ are better suited since they form an orthogonal basis set of functions on a unit disk. Zernike polynomials are expressed in polar coordinates ρ and θ as [107]

$$Z_n^m(\rho, \theta) = \begin{cases} N_n^m R_n^m(\rho) \cos(m\theta) & \text{for } m \geq 0 \\ N_n^m R_n^m(\rho) \sin(m\theta) & \text{for } m < 0, \end{cases}$$

$$N_n^m = \sqrt{\frac{2(n+1)}{1+\delta_{m0}}},$$

$$R_n^{|m|}(\rho) = \sum_{s=0}^{(n-|m|)/2} \frac{(-1)^s}{s![(n+|m|)/2-s]!} \times \frac{(n-s)!}{[(n-|m|)/2-s]!} \left(\frac{\rho}{\rho_p}\right)^{n-2s}, \quad (\text{D.1})$$

where n is an integer number and m can only take values $n, n-2, n-4, \dots, -n$ for each n . The radial coordinate is scaled to the exit pupil radius ρ_p (the radius of the image of the input aperture at the camera). Importantly, each term of this polynomial expansion has a one-to-one relation with a specific kind of aberration. Given the Zernike expansion of a wavefront, we can calculate its deviation from a perfect wavefront using the c_n^m coefficients of eq. (2.12).

Appendix E: Allan deviation dead time analysis

Dead times in the experiment were corrected introducing the Allan B-functions [62]:

We first define the Bias functions with the help of the function

$$F(A) = 2A^{\mu+2} - (A + 1)^{\mu+2} - |(A - 1)|^{\mu+2} \quad (\text{E.1})$$

Noise	μ
White	-1
Flicker	0
Random walk	1

The B_1 Bias function

$$B_1(N, r, \mu) = \frac{\sigma^2(N, T, \tau)}{\sigma^2(2, T, \tau)} = \frac{1 + \sum_{n=1}^{N-1} \frac{N-n}{N(N-1)} F(nr)}{1 + (1/2)F(r)} \quad (\text{E.2})$$

This coefficient relates the standard variance $\sigma^2(N, T, \tau)$ with the Allan variance including dead times at the end of the measurement (without binning).

The B_2 Bias function

$$B_2(r, \mu) = \frac{\sigma^2(2, T, \tau)}{\sigma^2(2, \tau, \tau)} = \frac{1 + (1/2)F(r)}{2(1 - 2^\mu)} \quad (\text{E.3})$$

This coefficient relates the Allan variance with dead time $\sigma^2(2, T, \tau)$ with the Allan variance free of dead times $\sigma^2(2, \tau, \tau)$

The B_3 Bias function for a two sample variance

$$B_3(2, \mathcal{M}, r, \mu) = \frac{\sigma^2(2, \mathcal{M}T_0, \mathcal{M}\tau_0)}{\sigma^2(2, T, \tau)} \quad (\text{E.4})$$

$$= \frac{2\mathcal{M} + F(\mathcal{M}r)\mathcal{M} - \sum_{n=1}^{\mathcal{M}-1}(\mathcal{M} - n)[2F(nr) - F((\mathcal{M} + n)r) - F((\mathcal{M} - n)r)]}{\mathcal{M}^{\mu+2}[F(r) + 2]} \quad (\text{E.5})$$

This coefficient relates the Allan variance with periodic dead times $\sigma^2(2, \mathcal{M}T, \mathcal{M}\tau)$ where \mathcal{M} is the binning parameter and the Allan variance with dead times accumulated at the end of the sampling is $\sigma^2(2, T, \tau)$.

In this experiment, we bin $M = 200$ images of $\tau_0 = 1$ ms with a dead time of 5 ms obtaining $T_0 = 6$ ms. That is, we measure $\sigma^2(2, \mathcal{M}T_0, \mathcal{M}\tau_0)$. To obtain a dead time corrected Allan variance we need to:

$$\sigma^2(2, \tau, \tau) = \frac{\sigma^2(2, \mathcal{M}T_0, \mathcal{M}\tau_0)}{B_3 B_2} \quad (\text{E.6})$$

Or the standard deviation

$$\sigma(2, \tau, \tau) = \frac{\sigma(2, \mathcal{M}T_0, \mathcal{M}\tau_0)}{\sqrt{B_3 B_2}} \quad (\text{E.7})$$

Noise detection

To obtain a noise model we use the B_1 bias functions

$$B_1(N, r, \mu) = \frac{\sigma^2(N, T, \tau)}{\sigma^2(2, T, \tau)} \quad (\text{E.8})$$

For this we need the $\sigma^2(2, T, \tau)$ which can be obtained from the B_3 functions:

$$\frac{B_1(N, r, \mu)}{B_3(N, r, \mu)} = \frac{\sigma^2(N, T, \tau)}{\sigma^2(2, MT_0, M\tau_0)} \quad (\text{E.9})$$

To obtain the standard deviation, we then square root this expression and solve this equation for μ

$$\sqrt{\frac{B_1(N, r, \mu)}{B_3(N, r, \mu)}} = \frac{\sigma(N, T, \tau)}{\sigma(2, MT_0, M\tau_0)} \quad (\text{E.10})$$

We replace the obtained μ in equation (E.7) to find the Allan deviation correction with dead times.

Bibliography

- [1] Rainer Blatt and David Wineland. Entangled states of trapped atomic ions. *Nature*, 453(7198):1008, 2008.
- [2] C. Monroe and J. Kim. Scaling the ion trap quantum processor. *Science*, 339(6124):1164–1169, 2013.
- [3] P. T. H. Fisk, M. J. Sellars, M. A. Lawn, and G. Coles. Accurate measurement of the 12.6 GHz “clock” transition in trapped $^{171}\text{Yb}^+$ ions. *IEEE transactions on ultrasonics, ferroelectrics, and frequency control*, 44(2):344–354, 1997.
- [4] AH Myerson, DJ Szwarc, SC Webster, DTC Allcock, MJ Curtis, G Imreh, JA Sherman, DN Stacey, AM Steane, and DM Lucas. High-fidelity readout of trapped-ion qubits. *Phys. Rev. Lett.*, 100(20):200502, 2008.
- [5] C. J. Ballance, T. P. Harty, N. M. Linke, M. A. Sepiol, and D. M. Lucas. High-fidelity quantum logic gates using trapped-ion hyperfine qubits. *Phys. Rev. Lett.*, 117:060504, Aug 2016.
- [6] J. P. Gaebler, T. R. Tan, Y. Lin, Y. Wan, R. Bowler, A. C. Keith, S. Glancy, K. Coakley, E. Knill, D. Leibfried, and D. J. Wineland. High-fidelity universal gate set for 9+ ion qubits. *Phys. Rev. Lett.*, 117(6):060505, 2016.
- [7] J. I. Cirac and P. Zoller. Quantum computations with cold trapped ions. *Phys. Rev. Lett.*, 74:4091–4094, May 1995.
- [8] A. Sørensen and K. Mølmer. Quantum computation with ions in thermal motion. *Phys. Rev. Lett.*, 82:1971–1974, 1999.
- [9] Thomas Monz, Daniel Nigg, Esteban A Martinez, Matthias F Brandl, Philipp Schindler, Richard Rines, Shannon X Wang, Isaac L Chuang, and Rainer Blatt. Realization of a scalable shor algorithm. *Science*, 351(6277):1068–1070, 2016.

- [10] S. Debnath, N. M. Linke, C. Figgatt, K. A. Landsman, K. Wright, and C. Monroe. Demonstration of a small programmable quantum computer with atomic qubits. *Nature*, 536:63–66, 2016.
- [11] Raymond Laflamme Phillip Kaye and Michele Mosca. *An introduction to Quantum computing*. Oxford university press, 2007.
- [12] Ebrahim Karimi and Robert W. Boyd. Classical entanglement? *Science*, 350(6265):1172–1173, 2015.
- [13] A. Einstein, B. Podolsky, and N. Rosen. Can quantum-mechanical description of physical reality be considered complete? *Phys. Rev.*, 47:777–780, May 1935.
- [14] J. S. Bell. On the einstein podolsky rosen paradox. *Physics*, 1(3):195–200, 1964.
- [15] T. D. Ladd, F. Jelezko, R. Laflamme, Y. Nakamura, C. Monroe, and J. L. OBrien. Quantum computers. *Nature*, 464:45, 2010.
- [16] W. Nagourney, J. Sandberg, and H. Dehmelt. Shelved optical electron amplifier: Observation of quantum jumps. *Phys. Rev. Lett.*, 56:2797, 1986.
- [17] Th. Sauter, W. Neuhauser, R. Blatt, and P. E. Toschek. Observation of quantum jumps. *Phys. Rev. Lett.*, 57:1696, 1986.
- [18] J. C. Bergquist, R. G. Hulet, W. M. Itano, and D. J. Wineland. Observation of quantum jumps in a single atom. *Phys. Rev. Lett.*, 57:1699, 1986.
- [19] C. Monroe, D. M. Meekhof, B. E. King, W. M. Itano, and D. J. Wineland. Demonstration of a fundamental quantum logic gate. *Phys. Rev. Lett.*, 75:4714–4717, Dec 1995.
- [20] M. A. Lawn P. T. Fisk, M. J. Sellars and G. Coles. transactions on ultrasonics, ferroelectrics, and frequencycontrol. *IEEE*, 44:344, 1997.
- [21] T. Schaetz M. D. Barrett R. B. Blakestad J. Britton W. M. Itano J. D. Jost E. Knill C. Langer R. Ozeri J. Chiaverini, D. Leibfried and D. J. Wineland. Realization of quantum error correction. *Nature*, 432:602–605, 2004.
- [22] Bryce Yoshimura, Marybeth Stork, Danilo Dadic, Wesley C. Campbell, and James K. Freericks. Creation of two-dimensional coulomb crystals of ions in oblate paul traps for quantum simulations. *EPJ Quantum Technology*, 2(1):2, Jan 2015.
- [23] D. J. Wineland, C. Monroe, W. M. Itano, D. Leibfried, B. E. King, and D. M. Meekhof. Experimental issues in coherent quantum-state manipulation of trapped atomic ions. *J. Res. Nat. Inst. Stand. Tech.*, 103:259–328, 1998.
- [24] D. Leibfried, R. Blatt, C. Monroe, and D. Wineland. Quantum dynamics of single trapped ions. *Rev. Mod. Phys.*, 75:281–324, Mar 2003.

- [25] Brian Vlastakis. *Controlling Coherent State Superpositions with Superconducting Circuits*. PhD thesis, Yale University, 2015.
- [26] Anders Sørensen and Klaus Mølmer. Entanglement and quantum computation with ions in thermal motion. *Phys. Rev. A*, 62:022311, Jul 2000.
- [27] Klaus Mølmer and Anders Sørensen. Multiparticle entanglement of hot trapped ions. *Phys. Rev. Lett.*, 82:1835–1838, Mar 1999.
- [28] D.F.V. James. Quantum dynamics of cold trapped ions with application to quantum computation. *Applied Physics B*, 66(2):181–190, Feb 1998.
- [29] C. Monroe, R. Raussendorf, A. Ruthven, K. R. Brown, P. Maunz, L.-M. Duan, and J. Kim. Large-scale modular quantum-computer architecture with atomic memory and photonic interconnects. *Physical Review A*, 89(2):022317, 2014.
- [30] J. I. Cirac and P. Zoller. A scalable quantum computer with ions in an array of microtraps. *Nature*, 404:579–581, 2000.
- [31] J. J. García-Ripoll, P. Zoller, and J. I. Cirac. Speed optimized two-qubit gates with laser coherent control techniques for ion trap quantum computing. *Phys. Rev. Lett.*, 91(15):157901, 2003.
- [32] L.-M. Duan. Scaling ion trap quantum computation through fast quantum gates. *Phys. Rev. Lett.*, 93:100502, 2004.
- [33] J. Mizrahi, C. Senko, W. C. Campbell, K. G. Johnson, C. W. S. Conover, and C. Monroe. Ultrafast spin-motion entanglement and interferometry with a single atom. *Phys. Rev. Lett.*, 110:203011, 2013.
- [34] J. Mizrahi, B. Neyenhuis, K. G. Johnson, W. C. Campbell, C. Senko, D. Hayes, and C. Monroe. Quantum control of qubits and atomic motion using ultrafast laser pulses. *Appl. Phys. B*, 114:45, 2013.
- [35] E. Streed, Norton B., A. Jechow, Weinhold T., and D. Kielpinski. Imaging of trapped ions with a microfabricated optic for quantum information processing. *Phys. Rev. Lett.*, 106:010502, 2011.
- [36] M. Palmero, S. Martínez-Garaot, D. Leibfried, D. J. Wineland, and J. G. Muga. Fast phase gates with trapped ions. *Phys. Rev. A*, 95:022328, Feb 2017.
- [37] J. Mizrahi. *Ultrafast Control of Spin and Motion in Trapped Ions*. PhD thesis, University of Maryland, 2013.
- [38] Kale G. Johnson. *Experiments with Trapped Ions and Ultrafast Laser Pulses*. PhD thesis, University of Maryland, 2016.
- [39] Shantanu Debnath. *A Programmable Five Qubit Quantum Computer using Trapped Atomic Ions*. PhD thesis, University of Maryland, 2016.

- [40] David Alexander Hucul. *A Modular Quantum System of Trapped Atomic Ions*. PhD thesis, University of Maryland, 2015.
- [41] Dimitris Trypogeorgos and Christopher J. Foot. Cotrapping different species in ion traps using multiple radio frequencies. *Phys. Rev. A*, 94:023609, Aug 2016.
- [42] F. Major and H. Dehmelt. Exchange-collision technique for rf spectroscopy of stored ions. *Phys. Rev.*, 170:91–107, 1968.
- [43] M.J. Madsen, W.K. Hensinger, D. Stick, J.A. Rabchuk, and C. Monroe. Planar ion trap geometry for microfabrication. *Applied Physics B*, 78(5):639–651, Mar 2004.
- [44] M. G. Raizen, J. M. Gilligan, J. C. Bergquist, W. M. Itano, and D. J. Wineland. Ionic crystals in a linear paul trap. *Phys. Rev. A*, 45:6493–6501, May 1992.
- [45] K. G. Johnson, J. D. Wong-Campos, A. Restelli, K. A. Landsman, B. Neyenhuis, J. Mizrahi, and C. Monroe. Active stabilization of ion trap radiofrequency potentials. *Review of Scientific Instruments*, 87:053110, 2016.
- [46] J. D. Sivers, L. R. Simkins, S. Weidt, and W. K. Hensinger. On the application of radio frequency voltages to ion traps via helical resonators. *Appl. Phys. B*, 107:921, 2012.
- [47] H. Eriksson and R. W. Waugh. *A Temperature Compensated Linear Diode Detector, Design Tip*. Agilent Technologies, 2000.
- [48] S. Olmschenk. *Quantum Teleportation Between Distant Matter Qubits*. PhD thesis, University of Maryland, College Park, 2009.
- [49] D. Kielpinski, C. Monroe, and D. J. Wineland. Architecture for a large-scale ion-trap quantum computer. *Nature*, 417(6890):709–711, 2002.
- [50] J. P. Schiffer. Phase transitions in anisotropically confined ionic crystals. *Phys. Rev. Lett.*, 70:818–821, Feb 1993.
- [51] Wayne M. Itano and D. J. Wineland. Laser cooling of ions stored in harmonic and penning traps. *Phys. Rev. A*, 25:35–54, Jan 1982.
- [52] Mark Acton. *Detection and Control of Individual Trapped Ions and Neutral Atoms*. PhD thesis, University of Michigan, 2008.
- [53] R. Noek, G. Vrijzen, D. Gaultney, E. Mount, T. Kim, P. Maunz, , and J. Kim. High speed, high fidelity detection of an atomic hyperfine qubit. *Opt. Lett.*, 38(22):4735–4738, 2013.

- [54] J. D. Wong-Campos, K. G. Johnson, B. Neyenhuis, and J. Mizrahiand C. Monroe. High-resolution adaptive imaging of a single atom. *Nature Photonics*, 2016.
- [55] J. Goodman. *Introduction to Fourier Optics*. McGraw–Hill, 1996.
- [56] I. Iglesias. Parametric wave–aberration retrieval from point–spread function data by use of a pyramidal recursive algorithm. *Appl. Opt.*, 37:5427–5430, 1998.
- [57] R. Barakat and B. Sandler. Determination of the wave–front aberration function from measured values of the point–spread function: a two–dimensional phase retrieval problem. *J. Opt. Soc. Am. A*, 9:1715–1723, 1992.
- [58] C. Avoort, J. Braat, P. Dirksen, and A. Janssen. Aberration retrieval from the intensity point–spread function in the focal region using the extended nijboer–zernike approach. *J. Mod. Opt.*, 52:1695–1728, 2005.
- [59] I. Novotny and B. Hecht. *Principles of Nano-Optics*. Cambridge University Press, 2006.
- [60] Vetterling W Press W., Teukolsky S. and Flannery B. *Numerical Recipes: The Art of Scientific Computing*. Cambridge University Press, 2007.
- [61] W. Riley. *Handbook of frequency stability analysis*. Special Publication 1065. NIST, 2008.
- [62] J. Barnes and D. Allan. Variances based on data with dead time between the measurements. Technical report, NIST, 1990. 1318.
- [63] R. Thompson, D. Larson, and W. Webb. Precise nanometer localization analysis for individual fluorescent probes. *Biophys. J.*, 82:2775–2783, 2002.
- [64] T. Quan, S. Zeng, and Z. Huang. Localization capability and limitation of electron–multiplying charge-coupled, scientific complementary metal–oxide semiconductor, and charge–coupled devices for superresolution imaging. *J. Biomed. Opt.*, 15:066005, 2010.
- [65] M. Biercuk, H. Uys, J. Britton, A. VanDevender, and J. Bollinger. Ultrasensitive detection of force and displacement using trapped ions. *Nature Nanotech.*, 5:646–650, 2010.
- [66] N. Rosen and C. Zener. Double stern-gerlach experiment and related collision phenomena. *Phys. Rev.*, 40:502–507, May 1932.
- [67] W. C. Campbell, J. Mizrahi, Q. Quraishi, C. Senko, D. Hayes, D. Hucul, D. N. Matsukevich, P. Maunz, and C. Monroe. Ultrafast gates for single atomic qubits. *Phys. Rev. Lett.*, 105:090502, 2010.

- [68] F. Diedrich, J. C. Bergquist, Wayne M. Itano, and D. J. Wineland. Laser cooling to the zero-point energy of motion. *Phys. Rev. Lett.*, 62:403–406, Jan 1989.
- [69] Bryce Gadway, Daniel Pertot, René Reimann, Martin G. Cohen, and Dominik Schneble. Analysis of kapitza-dirac diffraction patterns beyond the raman-nath regime. *Opt. Express*, 17(21):19173–19180, Oct 2009.
- [70] J. A. Grover, P. Solano, L. A. Orozco, and S. L. Rolston. Photon-correlation measurements of atomic-cloud temperature using an optical nanofiber. *Phys. Rev. A*, 92:013850, Jul 2015.
- [71] K. G. Johnson, B. Neyenhuis, J. Mizrahi, J. D. Wong-Campos, and C. Monroe. Sensing atomic motion from the zero point to room temperature with ultrafast atom interferometry. *Phys. Rev. Lett.*, 115:213001, 2015.
- [72] K. G. Johnson, J. D. Wong-Campos, B. Neyenhuis, J. Mizrahi, and C. Monroe. Ultrafast creation of large schrödinger cat states of an atom. *Nature Communications*, 8(697), 2017.
- [73] W. L. Erikson and Surendra Singh. Polarization properties of maxwell-gaussian laser beams. *Phys. Rev. E*, 49:5778–5786, Jun 1994.
- [74] R. J. Glauber. Coherent and incoherent states of the radiation field. *Phys. Rev.*, 131:2766, 1963.
- [75] E. C. G. Sudarshan. Equivalence of semiclassical and quantum mechanical descriptions of statistical light beams. *Phys. Rev. Lett.*, 10:277, 1963.
- [76] Q. A. Turchette, C. J. Myatt, B. E. King, C. A. Sackett, D. Kielpinski, W. M. Itano, C. Monroe, and D. J. Wineland. Decoherence and decay of motional quantum states of a trapped atom coupled to engineered reservoirs. *Phys. Rev. A*, 62:053807, 2000.
- [77] C. J. Myatt, B. E. King, Q. A. Turchette, C. A. Sackett, D. Kielpinski, W. M. Itano, C. Monroe, and D. J. Wineland. Decoherence of quantum superpositions through coupling to engineered reservoirs. *Nature*, 403:269, 2000.
- [78] U. Poschinger, A. Walther, K. Singer, and F. Schmidt-Kaler. Observing the phase space trajectory of an entangled matter wave packet. *Phys. Rev. Lett.*, 105:263602, 2010.
- [79] L. Deslauriers, S. Olmschenk, D. Stick, W. K. Hensinger, J. Sterk, and C. Monroe. Scaling and suppression of anomalous heating in ion traps. *Physical Review Letters*, 97(10):103007, 2006.
- [80] D. J. Wineland and W. M. Itano. Laser cooling of atoms. *Phys. Rev. A*, 20(4):1521, 1979.

- [81] Q. Turchette, D. Kielpinski, B. King, C. Myatt, C. Sachett, W. Itano, C. Monroe, and D. J. Wineland. Heating of trapped ions from the quantum ground state. *Phys. Rev. A*, 61:063418, 2000.
- [82] C. Gehrke. *Quantitative Characterization of Nonclassicality*. PhD thesis, University of Rostock, 2008.
- [83] E. Wigner. On the quantum correction for thermodynamic equilibrium. *Phys. Rev.*, 40:749, 1932.
- [84] J. A. Wheeler and W. Zurek. *Quantum Theory and Measurement*. Princeton University Press, 1983.
- [85] V. Giovannetti, S. Lloyd, and L. Maccone. Quantum-enhanced measurements: Beating the standard quantum limit. *Science*, 306:1330–1336, 2004.
- [86] M. A. Nielsen and I. L. Chuang. *Quantum Computation and Quantum Information*. Cambridge University Press, 2000.
- [87] E. Schrödinger. Die gegenwärtige situation in der quantenmechanik. *Naturwissenschaften*, 23:807–812; 823–828; 844–849, 1935.
- [88] M. Kasevich and S. Chu. Atomic interferometry using stimulated raman transitions. *Physical review letters*, 67(2):181, 1991.
- [89] C. Monroe, D. M. Meekhof, B. E. King, and D. J. Wineland. A “Schrödinger cat” superposition state of an atom. *Science*, 272:1131, 1996.
- [90] T. Kovachy, P. Asenbaum, C. Overstreet, C. A. Donnelly, S. M. Dickerson, A. Sugarbaker, J. M. Hogan, and M. A. Kasevich. Quantum superposition at the half-metre scale. *Nature*, 528(7583):530–533, 2015.
- [91] M. Brune, E. Hagley, J. Dreyer, X. Matre, A. Maali, C. Wunderlich, J. M. Raymond, and S. Haroche. Observing the progressive decoherence of the meter? in a quantum measurement. *Phys. Rev. Lett.*, 77:4887, 1996.
- [92] J. E. Mooij, T. P. Orlando, L. Levitov, L. Tian, C. H. Van der Wal, and S. Lloyd. Josephson persistent-current qubit. *Science*, 285(5430):1036–1039, 1999.
- [93] J. R. Friedman, V. Patel, W. Chen, S. K. Tolpygo, and J. E. Lukens. Quantum superposition of distinct macroscopic states. *Nature*, 406(6791):43–46, 2000.
- [94] B. Vlastakis, G. Kirchmair, Z. Leghtas, S. E. Nigg, L. Frunzio, S. M. Girvin, M. Mirrahimi, M. H. Devoret, and R. J. Schoelkopf. Deterministically encoding quantum information using 100-photon Schrödinger cat states. *Science*, 342:607, 2013.

- [95] A. D. OConnell, M. Hofheinz, M. Ansmann, R. C. Bialczak, M. Lenander, E. Lucero, M. Neeley, D. Sank, H. Wang, M. Weides, J. Wenner, J. M. Martinis, and A. N. Cleland. Quantum ground state and single-phonon control of a mechanical resonator. *Nature*, 464:697–703, April 2010.
- [96] N. Dörre, J. Rodewald, P. Geyer, B. von Issendorff, P. Haslinger, and M. Arndt. Photofragmentation beam splitters for matter-wave interferometry. *Physical review letters*, 113(23):233001, 2014.
- [97] P. Geyer, U. Sezer, J. Rodewald, L. Mairhofer, N. Dörre, P. Haslinger, S. Eibenberger, C. Brand, and M. Arndt. Perspectives for quantum interference with biomolecules and biomolecular clusters. *Physica Scripta*, 91(6):063007, 2016.
- [98] D. J. Wineland. Nobel lecture. superposition, entanglement, and raising Schrödinger’s cat. *Rev. Mod. Phys.*, 85:1103–1114, 2013.
- [99] S. Haroche. Controlling photons in a box and exploring the quantum to classical boundary. *Rev. Mod. Phys.*, 85:1083–1102, 2013.
- [100] D. Kienzler, C. Fluhmann, V. Negnevitsky, H.-Y. Lo, M. Marinelli, D. Nadlinger, and J. P. Home. Observation of quantum interference between separated mechanical oscillator wave packets. *Phys. Rev. Lett.*, 116:140402, 2016.
- [101] M. Hofheinz, H. Wang, M. Ansmann, R. C. Bialczak, E. Lucero, M. Neeley, A. D. OConnell, D. Sank, J. Wenner, J. M. Martinis, and A. N. Cleland. Synthesizing arbitrary quantum states in a superconducting resonator. *Nature*, 459:546, 2009.
- [102] W. C. Campbell and P. Hamilton. Rotation sensing with trapped ions. *arXiv preprint arXiv:1609.00659*, 2016.
- [103] J. D. Wong-Campos, S. A. Moses, K. G. Johnson, and C. Monroe. Demonstration of two-atom entanglement with ultrafast optical pulses. *arXiv:1709.05179*, 2017.
- [104] W. C. Campbell, J. Mizrahi, Q. Quraishi, C. Senko, D. Hayes, D. Hucul, D. N. Matsukevich, P. Maunz, and C. Monroe. Ultrafast gates for single atomic qubits. *Phys. Rev. Lett.*, 105(9):090502, 2010.
- [105] C. A. Sackett, D. Kielpinski, B. E. King, C. Langer, V. Meyer, C. J. Myatt, M. Rowe, Q. A. Turchette, W. M. Itano, D. J. Wineland, and Monroe C. Experimental entanglement of four particles. *Nature*, 404:256–259, March 2000.
- [106] D. J. Berkeland and M. G. Boshier. Destabilization of dark states and optical spectroscopy in zeeman-degenerate atomic systems. *Phys. Rev. A*, 65:033413, Feb 2002.

- [107] J. Wyant and K. Creath. *Applied Optics and Optical Engineering*, volume XI. Academic Press, 1992.